Charge and Energy Transfer in Different Types of Two-Dimensional Heterostructures

By

Matthew Z. Bellus

Submitted to the graduate degree program in Department of Physics and Astronomy and the Graduate Faculty of the University of Kansas in partial fulfillment of the requirements for the degree of Doctor of Philosophy.

Committee members

Dr. Hui Zhao, Chairperson

Dr. Judy Wu

Dr. Siyuan Han

Dr. Wai-Lun Chan

Dr. Rongqing Hui

Date defended: March 02, 2018

The Thesis Committee for Matthew Z. Bellus certifies
that this is the approved version of the following thesis :

Charge and Energy Transfer in Different Types of Two-Dimensional Heterostructures

Dr. Hui Zhao, Chairperson

Date approved: May 02, 2018

Abstract

In the last decade or so, layered materials have attracted significant attention due to their promise for tailoring electronic properties at an atomic level. Individually, these materials have exhibited strong attributes, relevant for both electronic and optoelectronic applications. However, the real world implementation of semiconducting materials is often derived from the junctions they form with other semiconductors. Thus, much of the interest in 2D materials arises from exploiting their ability to form low dimensional heterostructures. From a structural stand point, there are two ways these heterostructures can be formed, either vertically or laterally. The more common, vertical heterostructures, are intriguing due to their van der Waals adhesion, which eliminates many of the constraints attributed to lattice matching between materials. Lateral heterostructures, on the other hand, provide the unique opportunity to form in-plane junctions within a 2D sheet, creating novel 1D interfaces.

To better understand these various heterostructures, this dissertation aims to explore photocarrier dynamics, using ultrafast laser spectroscopy techniques, in several types of structures yet to be extensively studied. First, charge and energy transfer mechanisms in vertical heterostructures formed between various transition metal dichalcogenide monolayers are studied, highlighting the addition of type-I band alignment to the discussion. Next, the extent to which materials can interact electronically through van der Waals adhesion is explored at the interface between amorphous and crystalline layers.

From there, the focus shifts slightly to carrier dynamics across lateral junctions formed within monolayer sheets of transition metal dichalcogenides. This includes a discus-

sion on lateral heterostructures, formed between different materials, as well as homostructures where an electronic junction can be induced in a single material. All of these studies will provide a unique overview on the possible directions and applications for which two dimensional materials can be facilitated.

This dissertation includes previously published authored material.

Acknowledgements

I am truly grateful for the experiences and knowledge I have gained in my time at The University of Kansas. I have had the opportunity to meet incredible people along this journey and would like to take this section to thank those whom have gotten me to this milestone in life. I have been very fortunate in my graduate experience to work with two amazing advisors, Dr. Hsin-Ying Chiu and Dr. Hui Zhao. First, I would sincerely like to thank Dr. Chiu, who initially welcomed me into her group during my final year of undergrad. Her passion for science and discovery, and belief in me, truly inspired me to continue my journey in physics and pursue my PhD. I have learned so much from her and been provided so many opportunities for which I will be forever grateful. Next, I need to thank Dr. Zhao, who graciously accepted me into his research group part way through my graduate education. His patience and understanding as I adjusted to a new group and shifted my research focus is much appreciated. The opportunities he has provided through sending me to conferences and events outside of KU, as well as the vision and guidance he provided on so many research projects has been amazing. So much of the positive direction in which I believe my life to be headed is owed to these two.

I also need to thank my fellow lab mates, especially Dr. Frank Ceballos and Dr. Quinnan Cui, who helped teach me the majority of experimental techniques and lab practices. I would like to thank them along with Samuel Lane and Peymon Zereshki for their intellectual inputs and emotional support throughout this process, as well. The friendships I have built within the lab are ones I hope last a lifetime.

I also want to thank the other members of my committee, Dr. Judy Wu, Dr. Siyuan

Han, Dr. Wai-Lun Chan, and Dr. Rongqing Hui. I have been fortunate to learn from each of them in both the classroom and from their insightful inputs on research. Their experience and guidance has helped mold me into the scientist I am today. I need to give a special thanks to Dr. Wu and her group for allowing me to learn about and utilize various research tools from her lab.

I need to thank the various collaborators that have provided both samples, theory, and input for projects contained within this dissertation. Dr. Xiao Cheng Zeng and researchers, at the University of Nebraska-Lincoln, provided the theory on TMD band alignment leading to the work on type-I heterostructures. Dr. Shu Ping Lau and his group from The Hong Kong Polytechnic University provided us with the amorphous black phosphorus samples. Finally, I need to thank Dr. Kai Xiao and team at Oak Ridge National Laboratory for providing the lateral heterostructure samples. It is through collaborations like these that scientific research truly flourishes.

Last, but certainly not least, I would like to acknowledge all my friends and family that have given me so much support over the years. My parents, Peter and Jeanne, have furnished me with as good an upbringing as anyone could ask for. I could never have gotten to this point in my life without their unconditional love and support. I also thank my brother Alex and his wife Molly for their encouragement along the way and for being such great role models for how to pursue the next chapter in my life.

Contents

List of Figures

Chapter 1

Introduction

1.1 Two-Dimensional Materials

The discovery of graphene[1–5] has created an exponentially growing interest in 2D materials[6–9], such as the transition metal dichalcogenides (TMDs), transition metal oxides, hexagonal boron nitride (hBN), phosphorene, silicene, germanene, *etc.* Various 2D materials help cover a whole gamut of electronic structures from insulating to superconducting. Hexagonal boron nitride for instance is known to be insulating with a band gap around 6 eV and is commonly used as an ideally flat substrate or tunnel barrier[10;11]. Most of the TMDs, like MoS_2, $MoSe_2$, WS_2, WSe_2, *etc.*, are semiconductors. With band gaps in the visible to near infrared (IR) range (1-2 eV), they are being explored for uses in a wide variety of electronic and optoelectronic applications[12]. There has also been a fairly recent surge in studies on graphene analogues, where the 2D lattice is comprised of only one element like phosphorene[13], silicene, and germanene. Similar to graphene, these allotropes of their respective elements have shown promising electronic properties. However, unlike graphene, they more commonly exist in metastable forms making them difficult to study[14]. Although it does not exhibit quite the prestige of graphene in attributes like electronic mobility and ambient stability, phosphorene does possess a sizeable band gap, making it more desirable for logic device applications[15].

In general, these atomically thin materials possess several unique features that make them attractive for both fundamental research and applications. First, as the number of atomic layers approaches zero, the electronic structure of most 2D materials, namely graphene[16], the TMDs[17;18], and phosphorene[19], show a strong layer-dependence. One of the most notable effects is in the

electronic band structure of the materials. Monolayer graphene for instance is known to be a semimetal as it has a zero band gap, but actually exhibits the ability to open up a slight gap in bilayer[20]. Most of the TMDs have been found to exhibit a transition from an indirect band gap, in two or more layers, to a direct band gap in monolayer[21]. Changing the thickness of the TMDs can also strongly affect second-order nonlinear optical properties[22;23] as well as spin-valley coupling[24–26]. This is due to the altered crystal symmetry (*i.e.* inversion symmetry) that results from the presence of additional discrete layers. These allow for the control of electronic and optical properties by changing the sample thickness.

Secondly, the atomic thickness is also important as the material is thinner than the typical Coulomb interaction length, allowing a significant part of the electric field between charge carriers to leak to the surrounding area. This reduces the dielectric screening which can result in an enhancement of the interactions between charge carriers. Ultimately this causes an orders-of-magnitude increase in exciton[27;28], trion[29], and bi-exciton binding energies[30;31], as well as efficient carrier thermalization[32], relaxation[32], and exciton formation[33;34]. The leaked field also provides opportunities to control the electronic and optical properties of 2D materials by manipulating their surroundings[35–37]. For instance, relatively large differences in observed optical bandgaps in TMD MLs has been shown to be a result of their surrounding dielectric environment[38]. Also a product of their ultimate thinness is the exhibition of a large Young's modulus, allowing these materials to sustain large amounts of strain without fracturing. This leads to much promise for flexible device applications[39;40].

Third, the van Hove singularity that commonly exists in 2D materials results in exceptionally high optical absorption, which is attractive to many optical and optoelectronic applications[41;42]. This high efficiency light absorption can lead to large power densities in solar cell applications, potentially orders-of-magnitude larger than in silicon and GaAs[43].

Fourth, the van der Waals interlayer bonding results in a near-perfect surface without dangling bonds. This helps reduce scattering achieving high charge mobility[39] and long spin lifetimes[44]. As will be explained in the next section, this is also of great importance for semiconducting het-

erostructures where different layers are stacked together.

Overall, these features make 2D materials not only an ideal platform to explore new physics in low-dimensions, but also attractive candidates for near-future electronic and optoelectronic application, such as field-effect transistors[45;46], integrated circuits[47;48], solar cells[49], photodetectors[49], and light-emitting diodes[50–52].

1.2 Heterostructures in Flatland

Although 2D materials are attractive to fundamental research and applications as individual materials, one of the most intriguing aspects is that they provide a new route to fabricate multilayer structures[53]. Such multilayers are formed by combining several 2D materials with certain stacking orders *via* interlayer vdWs interaction. This virtually eliminates any constraints due to lattice matching, allowing for an expanded degree of freedom when forming these heterostructures. Hence, this new approach can produce a vast number of new materials for many applications, and can potentially transform material discovery[54;55].

The inert 2D nature of these materials and vdWs interaction addresses a number of drawbacks found in conventional heterostructures. In principle, these multilayers are free from interfacial defects, experience no interlayer atomic diffusion, and endure little to no lattice strain from interactions with other layers. This makes for not only less constrained matching of materials, but also more pristine junctions. An example of a vertical heterostructure between graphene and a monolayer TMD is shown in Fig. 1.1. Figure 1.1(a) shows the side view of the heterostructure highlighting that there is no interlayer bonding and actually a small gap between the layers. A top view of the heterostructure is shown in Fig. 1.1(b). Here, a clear Moiré pattern is seen, creating larger hexagonal patterns in the overall lattice. Several studies have reported on the importance of these patterns and the formation of superlattices[56–58] in hBN-graphene heterostructures.

In addition, the vdWs multilayers are still thin compared to more traditional heterostructures and thus remain rather flexible, withstanding relatively high levels of applied strain. They are also chemically stable as there is no physical bond between layers to alter their individual chemistry.

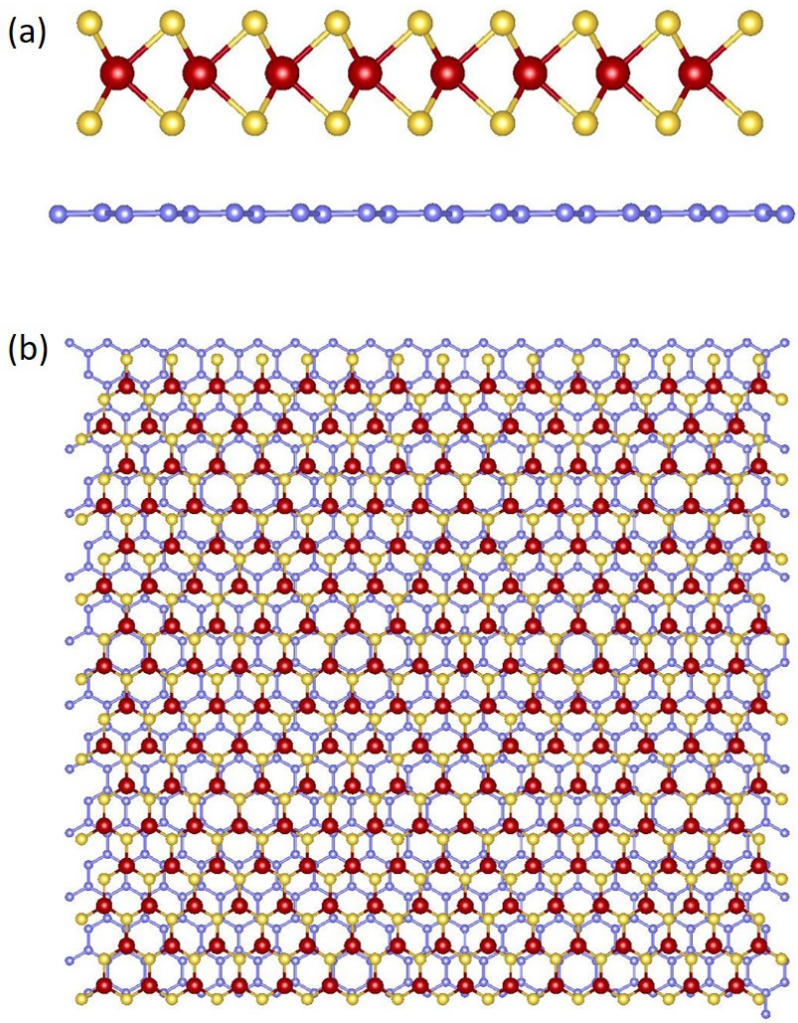

Figure 1.1: Schematic of a TMD-Graphene vertical heterostructure. (a) Side view of the heterostructure. (b) Top view of the heterostructure showing the overlap of the honeycomb hexagonal lattices of the two materials.

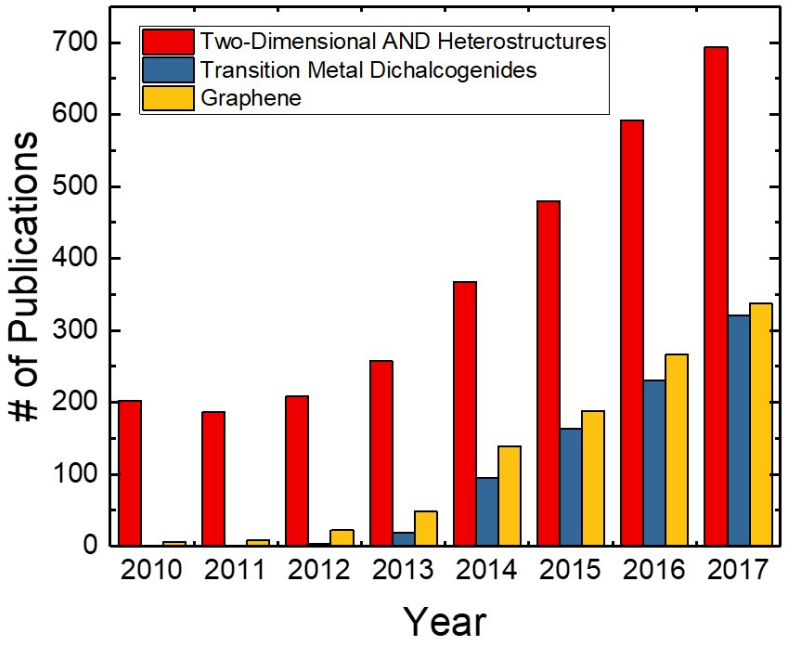

Figure 1.2: Number of publications by year according to the Web of Science on the topics of "Two-Dimensional" and "Heterostructures" (Red). The blue and yellow data represents the number of publications within the realm of 2D heterostructures for transition metal dichalcogenides and graphene, respectively.

This holds true when forming a heterostructure between a 2D layered material and non-layered material. Their fabrication is compatible with current thin-film technologies with advances in chemical vapor deposition (CVD) and epitaxial growth of different materials.

With these promising attributes, the study of 2D heterostructures has gained a lot of momentum in recent years. According to Web of Science, publications each year on this topic from 2010 to 2017 have grown roughly exponentially as seen in Fig. 1.2 (red). In the last few years, a large number of these efforts involved graphene (yellow) and/or TMDs (blue) (~50%). Combining graphene with TMDs is beneficial for optoelectronic applications since the former can serve as electrodes[59] while the latter, functions as the light absorption or emission layer[42]. Low-resistance contacts between graphene and TMD have also been achieved[60;61].

Various applications of this heterobilayer have been explored, such as photodetectors[62–64], photovoltaic devices[41;62], field-effect transistors[65–68], memory devices[69], and vertical tunneling

transistors[70]. Techniques for scalable growth of graphene-TMD heterobilayers have also been developed[71–73]. The study of TMD-TMD heterobilayers can provide valuable information on van der Waals interlayer coupling, and achieve tuning of the optical and transport properties of these materials. Most TMD-TMD heterobilayers form type-II band alignments, where the lowest conduction band and highest valence band are separated in the two layers[74–77]. This facilitates interlayer charge separation[78;79], extended photocarrier lifetime[80;81], and the formation of p-n junctions[82;83]. Recent studies have revealed potential applications of TMD-TMD heterobilayers for valleytronics[84–86], quantum light emitters[87], photovoltaics[88], and light-emitting diodes[89].

Also of increasing interest in this field are lateral heterojunctions formed within a single 2D layer. In this case, different materials are either grown in succession where one material is grown first and a second materials growth process expands the sample outward. Other methods utilize lithography techniques along with different types of atom changing methods. With the TMDs, this can be either or both, metal changing *i.e.* Mo $\leftrightarrow$ W, or chalcogen changing *i.e.* S $\leftrightarrow$ Se. With a physical junction size of $<$10 nm, lateral heterostructures in this context have been shown to have strong current rectification[90], increased photoluminescence at the junction, and light harvesting applications[91]. A depiction of an ideal lateral heterostructure between ML TMDs is shown in Fig. 1.3 with (a) showing a side view and (b) a top view. In this case, the metal atom (blue) remains constant throughout, whereas the chalcogen atom (yellow to red) changes at the junction. In practice, there would be more cross-over with the chalcogen atoms, leading to about a 5-10 nm region where both chalcogen atoms are interspersed.

Finally, emerging as another promising manipulation of charge carriers in these materials is the formation of lateral homojunctions. Here, by methods such as electronic gating[92–94], chemically doping[95], or changing of the dielectric environment in different areas of a single sheet of a material[96], lateral semiconducting junctions are formed. For example, the lateral junction between semiconducting and metal MoS_2 (Nb-doped) has been shown to create Schottkey-free edge contacts[97]. Several studies have shown the ability to modulate the electronic structure in monolayer TMDs using dual-gate environments. Often times this will create current rectification through the

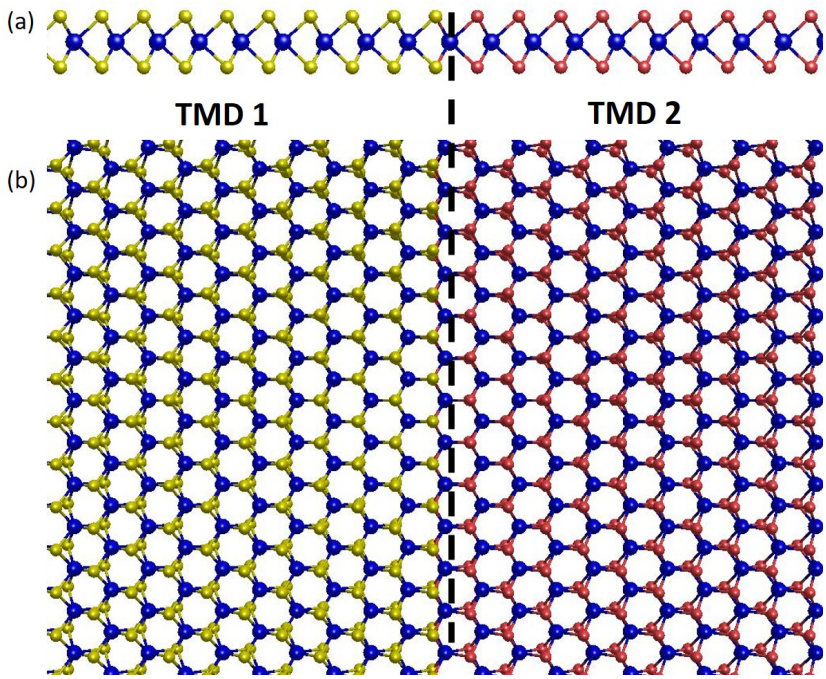

Figure 1.3: Schematic of a TMD-TMD lateral heterostructure. (a) Side view of the heterostructure. (b) Top view of the heterostructure.

formation of an n-n+ type of junction, but in ambipolar materials, p-n junctions can form. This has been shown to create different functionalities, such as light harvesting and emission, from a single material device[92–94].

As previously highlighted, changes to the dielectric environment can inhibit large alterations to electronic properties in these 2D materials. Thus, lateral homostructures can be created in monolayers with laterally diverse substrates or at a lateral interface between a covered and uncovered area. For instance, scanning tunneling spectroscopy studies have shown type-I band alignment and band bending at the interface between monolayer and bilayer in several TMDs[96].

1.3 Charge and energy transfer in van der Waals multilayers

One key process for achieving emergent properties in van der Waals multilayers is effective transfer of charge and energy between different layers. As discussed in the previous section, the weak vdWs adhesion allows for the a pristine interface between layers that also keeps the unique prop-

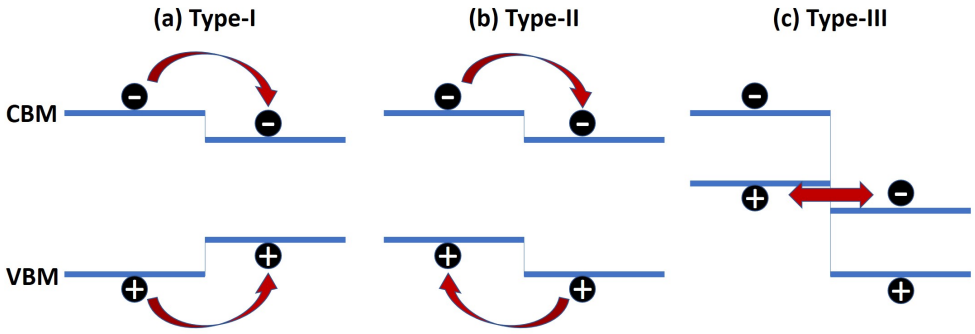

Figure 1.4: The three types of band alignment that dictate charge transfer in semiconducting heterostructures. (a) Type-I band alignment, where the CMB and VBM are both on the same side of the junction causing both carrier to transfer in the same direction. (b) Type-II alignment where the CBM and VBM are located on different sides causing charge separation. (c) Type-III alignment where the CBM of one material is below the VBM of the other. This often results in tunneling mechanisms across the junction.

erties of each material intact. This is because there is no physical bond between the materials at the interface. Ultimately, this has led many to treat these heterostructures as near perfect semiconducting junctions and utilize Anderson's Rule as predictor of charge transfer. Anderson's Rule simply treats the alignment of the respective energy bands with regard to the material work function or electron affinity relative to a common vacuum level. This, then, allows three types of band alignment, as shown in Fig. 1.4.

Type-I band alignment is created when the conduction band minimum (CBM) and valence band maximum (VBM) are both contained in the same material. This results in both types of charge carriers to transfer to the smaller band gap material. Type-II alignment occurs when the respective CBM and VBM of the two materials straddle each other as shown in Fig. 1.4(b). This alignment facilitates charge separation at the junction. Finally, type-III band alignment is the result of largely differing work functions between the materials resulting in the CBM of one materials to be lower than the VBM of the other. Here, any charge transfer is typically a result of tunneling mechanisms.

Although charge transfer is of great importance in heterostructures, it is also pivotal to discuss the role of energy transfer in these systems. This is especially true when considering interactions between two layers that have no net charge transfer. Figure 1.5 shows two main pathways for the

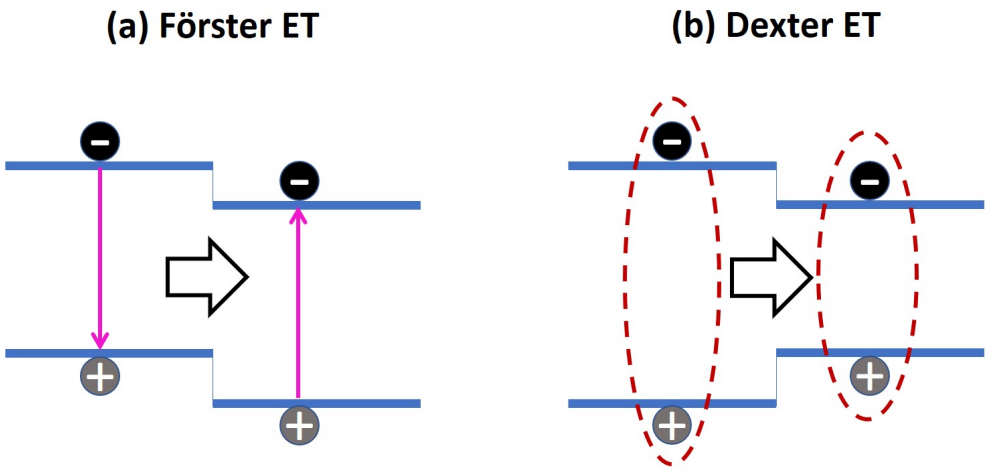

Figure 1.5: Types of energy transfer across semiconducting junctions. (a) Example of a Förster-type energy transfer process. The pink arrows represent the recombination process in one layer that leads to the excitation in the other (b) Example of a Dexter-type energy transfer process. Here, electrons and holes can move across the junction as a bound pair.

energy transfer between monolayers, Förster-type energy transfer (ET)[98], and Dexter-type energy transfer[99;100]. Förster-type energy transfer (Fig. 1.5(a)) occurs *via* nonradiative dipole-dipole coupling in the two layers. Here, an electron-hole pair (or exciton) in the first layer recombines nonradiatively, transferring the energy to the other layer. This leads to the excitation of an electron-hole pair in the second layer. With the band alignment shown in Fig. 1.5(a), this process is likely to be followed by a hole transfer process toward the first layer.

Dexter-type energy transfer involves the sequential or simultaneous transfer of both carrier types, as shown in Figure 1.5(b). This is the same process that results from type-I band alignment, shown in Fig 1.4(a). However, the transfer of opposite charges results in no net charge transfer, and thus the collective movement of an electron-hole pair leads to the transfer of energy from one material to the other. This effect mimics Förster-type energy transfer, albeit with different physics mechanisms.

The charge and energy transfer processes are expected to play key roles in van der Waals multilayers for electronic and optoelectronic devices because they are basic elements for coupling different layers. As the first step towards understanding these processes, charge and energy transfer

in heterobilayers formed by TMDs and graphene have been studied by femtosecond transient absorption[78;79;101–103] and steady-state optical spectroscopy measurements[104;105] by several groups (including us). Based on these studies, the following experimental knowledge appears to be established: First, between two TMD monolayers that form a type-II band alignment, interlayer charge transfer occurs on a time scale shorter than 100 fs[78;79;101;102;104]. Second, charge transfer is not strongly dependent on the twist angle[85;103;104]. Third, energy transfer occurs on a 1-ps time scale, and makes a minor contribution when charge transfer is efficient[104;105].

The highly efficient interlayer charge transfer observed in these studies is encouraging news for the development of van der Waals multilayers for electronic and optoelectronic technologies. However, the physics mechanisms of charge and energy transfer are yet to be well understood. A number of theoretical models have been proposed to explain the ultrafast charge transfer process: First, delocalization in momentum space due to strong localization in real space may help fulfill in-plane momentum conservation requirements[106]. Second, quantum coherence at the interface can help overcome the Coulomb attraction[107]. Third, the interlayer coupling between some states can be enhanced by the Coulomb field from initially transferred charges[108]. Lastly, intervalley scattering of carriers from layer-uncoupled to layer-coupled states can assist charge transfer[109]. These models are plausible and have established a foundation for ultimately understanding this process. However, more experimental studies that reveal different aspects of charge and energy transfer, and identify dominant mechanisms under different conditions are highly desired.

1.4 Overview of Dissertation

The previous sections provided an overview of the key topics that will be present throughout this dissertation. Better understanding the mechanisms behind charge and energy transport in these novel materials is of great importance to establish their viability for future applications. Ultimately, the studies that follow will explore the dynamic processes of photocarriers within a wide variety of 2D heterostructure systems.

The physical basis for these studies with be discussed in Chapter 2. I will devolve into the

different experimental methods for characterizing these ultrathin materials, as well as how we study different aspects of carrier dynamics in these systems. Mainly, I will discuss the physics of light-matter interactions and the variations of transient absorption microscopy experiments employed to study the dynamics of injected photocarriers.

Chapter 3 will look at a few studies involving vertically stacked 2D heterostructures. This will begin with a photoluminescence study on a $MoSe_2$-WS_2 heterostructure where we observe the formation of charged excitons, also known as trions, which pointed towards charge separation. Next, I will explore two more studies on heterostructures that were found to exhibit type-I band alignment, MoS_2-ReS_2 and WSe_2-$MoTe_2$. Here, we used transient absorption microscopy to study the resulting exciton transfer from the larger gap material to the smaller gap material.

The next chapter will explore another vertical heterostructure that is truly unique to the realm of 2D materials, that between a monolayer crystalline semiconductor and an ultrathin amorphous semiconductor. In this study, we look at carrier dynamics in an heterostructure formed by stacking monolayer WS_2 on top of amorphous black phosphorus (aBP). As a new material, we first study the carrier dynamics in samples of aBP with different thicknesses. With a varying band gap that is found to be inversely related to thickness, we focus on the interaction between the thinnest aBP sample and ML WS_2.

Finally, Chapters 5 and 6 concentrate on carrier dynamics in different lateral 2D structures. Chapter 5 looks at observed exciton transport across a MoS_2-$MoSe_2$ lateral heterojunction, which is formed by a combination of lithographic patterning and a chalcogenide changing process. In Chapter 6, we explore the carrier dynamics in lateral homojunctions formed in ML $MoSe_2$ by modifying the dielectric environment in part of the sample. In this case, we place relatively thick layers of hBN on portions of $MoSe_2$ flakes in an attempt to increase dielectric screening which can impact the energy landscape within these monolayers. It is expected that this modification should create a lateral semiconducting junction at the interface between covere and uncovered $MoSe_2$. Chapter 7 will provide a summary of these studies and elaborate on some potential future outlooks for the field.

Chapter 2

Experimental Techniques

Before diving into the actual studies performed on different heterostructure samples it is important to provide justification for the experimental methods. This chapter will focus on the methods used to study carrier dynamics in these 2D materials and heterostructures. In section 2.1, the process of photoluminescence (PL) spectroscopy is described. Next, the techniques behind time-resolved pump-probe spectroscopy are discussed in section 2.2. This is expanded in section 2.3, to include a spatial resolution component to these experiments. Finally, a discussion of the main dynamic processes observed from the methods in 2.3, diffusion and drift transport, are highlighted in 2.3.1 and 2.3.2, respectively.

2.1 Photoluminescence Spectroscopy

To study general trends of energy relaxation in these ultrathin systems, we often utilize photoluminescence (PL) spectroscopy. PL is a process in which photons excite carriers in a material to a higher energy state and the subsequent relaxation results in photon emission. Typically in semiconductor materials, these excited free carriers quickly and non-radiatively relax to the conduction band edge, where they form excitons. The recombination of these excitons results in photon emission with an energy consistent with the optical band gap of the material. This optical band gap is often slightly lower than the electrical band gap due, in large part, to the binding energy of the excitons[110]. It is also important to note that PL is best used to study direct gap materials, where the VBM and CBM are at the same position in momentum space. The need for phonon assisted momentum transitions can greatly suppresses photon emission in indirect gap materials. Excitons

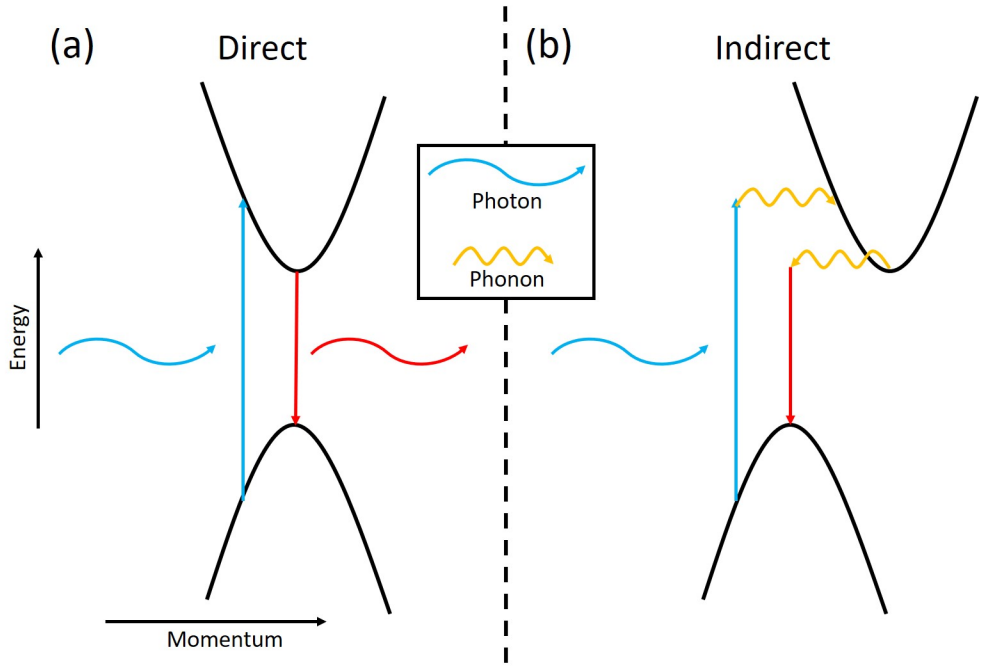

Figure 2.1: Energy and momentum transitions for photoexcited carriers for (a) direct gap and (b) indirect gap materials. The curved arrows represent photons, either excitation photons (blue) or emitted photons (red). The more squiggly arrows (yellow) represent phonons which assist in momentum transition in materials with indirect band gaps.

are also less stable in indirect materials, making them more susceptible to decay back into free electrons and holes where they are more likely to non-radiatively dissipate their excited state energy[110]. This is shown in Fig. 2.1, with (a) showing the process for direct gap materials and (b) the phonon assisted indirect transition.

For TMD samples, this plays an important role in determining if a sample has ML thickness as many of these materials transition from a direct gap in ML to indirect in 2 or more layers[21;111]. A strong PL yield is often a fast and easy way to confirm monolayer thickness and quality of these ultrathin samples.

An example of a typical PL setup is shown in Fig. 2.2. Here, a monochromatic light source, typically a diode laser, is focused onto the sample through an objective lens. The reflected beam along with the resulting PL emission are then collimated though the same lens and sent towards a spectrometer. Before reaching the spectrometer, the reflected beam from the pump is filtered out using appropriate optical filters. In the spectrometer, a grating separates the PL spectra into

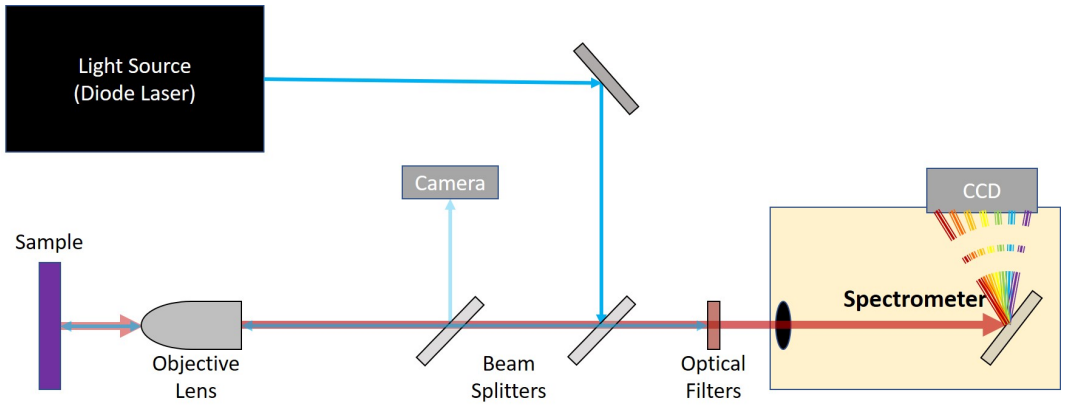

Figure 2.2: Schematic of a typical PL experimental setup.

wavelength ranges where it is then collected by a thermoelectrically cooled charge-coupled device (CCD) camera.

2.2 Time Resolved Pump-Probe Spectroscopy

The bulk of the projects contained in this dissertation utilize time resolved pump-probe spectroscopy techniques to study different aspects of carrier dynamics in these 2D systems. This involves two ultrashort laser pulses focused onto the sample. Figure 2.3 outlines the mechanism behind this type of experiment. In a typical experiment, the pump photon energy will be larger than the gap energy of the material and the probe will be tuned to the exciton resonance, which is typically near the optical band gap of the material. When the pump pulse reaches the sample, these photons excite electrons from the valence band to higher energy states in the conduction band. After a short thermalization process and energy relaxation, these carriers settle near the conduction band edge at which point they form excitons with the holes remaining in the valence band. The probe, with an energy that can only excite carriers to the band edge, will be mostly reflected when a significant portion of these excited states near the band edge are filled from the pump. As the excitons recombine, they free states in the conduction band. This allows more of the probe photons to be absorbed, decreasing the reflection[112]. We track the differential reflection of this probe pulse as a function of the relative time delay between the arrival of the pump pulse and the probe pulse.

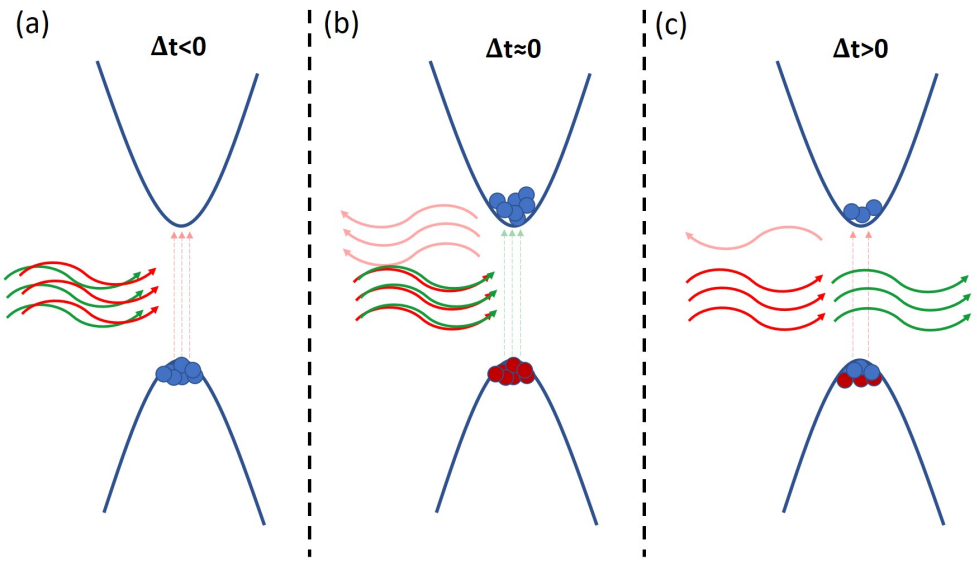

Figure 2.3: Schematic of the mechanism behind time resolved pump-probe experiments. Red arrows represent the probe photons and green arrows the pump photons. The blue and red circles represent electrons and holes, respectively (a) Early delay times, before the pump reaches the samples. Probe photons are mostly absorbed by the material in the form of excited electrons. The red dashed arrows represents these excitations. (b) The system just after the pump reaches the sample. The electrons are excited to the conduction band (green dashed arrows). With no available states near the band edge, the probe is mostly reflected. (c) Later delay times where the electron-hole pairs recombine, freeing up states in the conduction band allowing for some probe photons to be absorbed.

This differential reflection is defined as, $\frac{\Delta R}{R_0} = \frac{R-R_0}{R_0}$, where R and R_0 represent the reflection of the probe with and without the presence of the pump, respectively.

Although a relatively simple process, there is a lot that goes into creating such an experiment. A generalized setup for this type of experiment is shown in Fig. 2.4. The process for creating the pump and probe beams is outlined in Fig. 2.4(a). Here, a continuous wave, 532 nm, pump laser is used in conjunction with a tunable, mode-locked, Ti:Sapphire oscillator to create ultrashort pulses, as short as <100 fs, at a wavelength typically between 750 nm and 850 nm. This beam can then be used in a number of different ways to generate the desired pump or probe beams based on the samples and conditions being studied. If longer wavelengths, in the infrared (IR) range are needed, part of the output can be directed to a synchronously pumped parametric oscillator (SPPO), which can be tuned to an output between 1.1 μm and 2.6 μm. In some cases, we use a barium borate (BBO) crystal to double the frequency of the output from either the SPPO or Ti:Sapphire. We

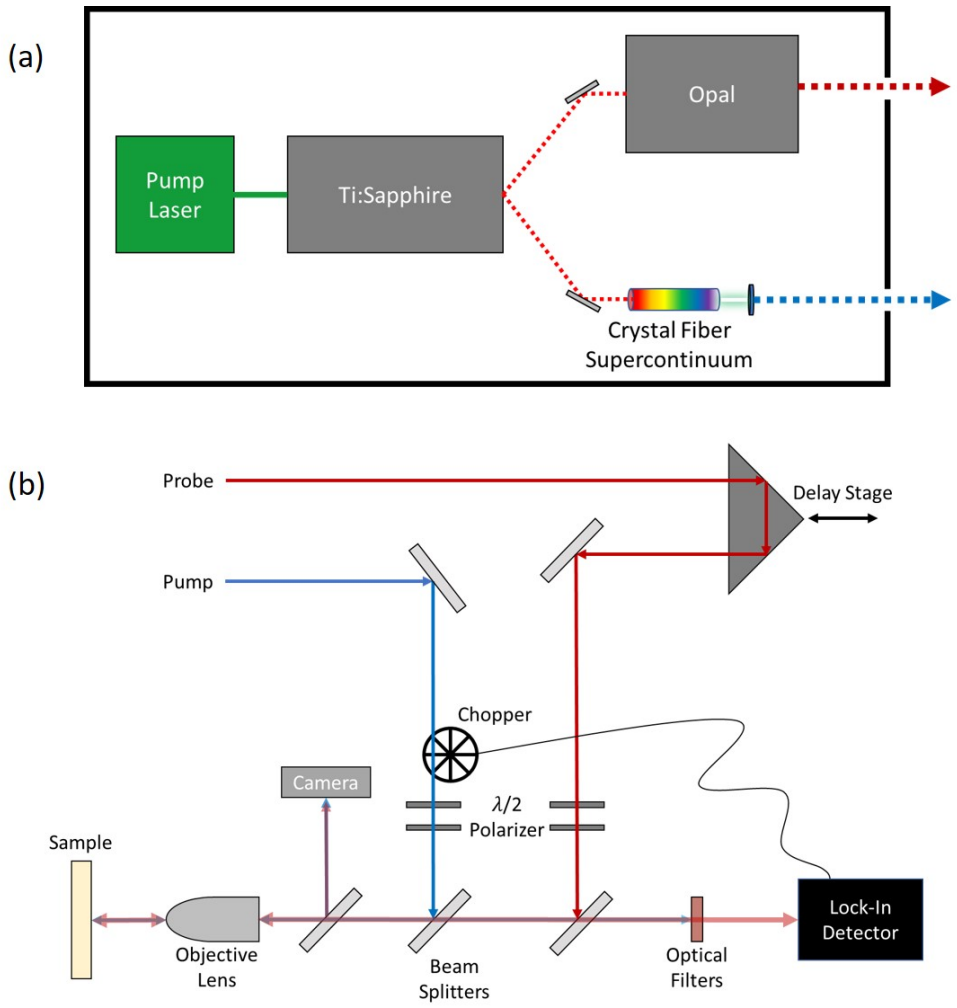

Figure 2.4: Setup for time resolved pump-probe spectroscopy. (a) Schematic of the process to create the ultrafast pump and probe beams. (b) Schematic of the overall experimental setup.

can also use the Ti:Sapphire output to pump a nonlinear photonic crystal fiber, which generates a supercontinuum. A band pass filter can then be placed after the fiber to select a desired wavelength from this broad spectral output.

Some combination of these outputs are then used as the pump and probe pulses for the experiment. One of these beams is sent to a set of mirrors or a retroreflector that is attached to a motorized delay stage. This allows for control of the relative path length between the pump and probe beams. In turn, this path length difference correlates to a relative time delay between the arrival of each pulse.

The incident power of each beam is controlled using combinations of half wave plates ($\lambda/2$)

and polarizers. An objective lens is used to both focus the beams onto the sample, as well as collect and collimate the reflections. This reflection is sent through a beam splitter with a small portion of the beam sent towards a CCD camera in order to track the position of the laser spots on the sample. The remaining portions of the beams are sent to a photo-detector. Before reaching the detector, optical filters are used to block the pump beam so only the reflection of the probe is measured. This is important, as we want to observe how the pump affects the probe reflection. Thus, the pump is sent through a mechanical chopper before reaching the sample. The chopper is connected to a lock-in amplifier which filters out contributions without the chopped frequency. This allows us to directly measure the portion of the probe reflection that is influenced by the pump.

We then track this differential reflection signal as function of delay stage position. This can be translated into a delay time by simply using the speed of light and the relative path length change. As explained earlier, over time, excitons excited by the pump will recombine, opening up more available states for probe photons to be absorbed, subsequently reducing the reflection. This results in a measured signal that decays with increasing delay time as a result of exciton recombination. We can, thus, measure the recombination mechanisms and how the carrier distribution evolves over time.

For heterostructure samples, we can choose appropriate pump and probe wavelengths to observe dynamics specific to the different materials. As will be discussed in later chapters, this can provide insights into both the charge and energy transfer across material boundaries.

2.3 Spatiotemporally Resolved Pump-Probe Spectroscopy

In addition to temporally resolving the differential reflection of the probe, it can also be measured as a function of pump position to spatially resolve the carrier dynamics. Here, the probe spot is left stationary to keep the reflection, R_0, constant. The pump spot is then moved across sample by rotating the beam splitter that directs the pump beam into the objective lens. This beam splitter is equipped with pico-motors, allowing for very precise movement of the pump spot. At each position of the pump, the differential reflection is measure as a function of the delay time. This

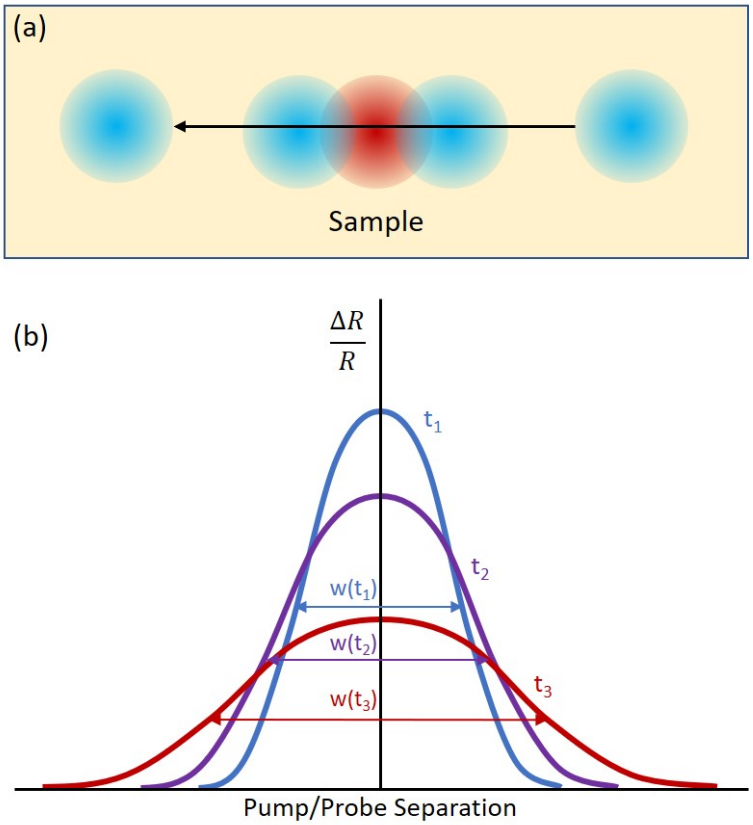

Figure 2.5: (a) Schematic of the how the carrier distribution is resolved spatially. (b) Sample spatial profiles of the differential reflection based on this measurement technique. The blue, purple, and red curves represent the expected evolution of these profiles for later delay times ($t_1 > t_2 > t_3$). The width of the distribution is expected to increase over time as carriers diffuse outward.

general concept is shown in Fig. 2.5. The blue and red circles in (a) represent the focused pump and probe laser spots, respectively. An depiction of the measured spatial profiles at different time steps is shown in (b).

Ultimately, the measured spatial profile represents the convolution of the probe spot and the carrier density distribution. This can be represented by,

$$S(x,t) = \int P(x)N(x-\mu,t)d\mu, \tag{2.1}$$

where $P(x)$ is the spatial shape of the probe (typically Gaussian), $N(x,t)$ is the injected carrier density as a function of space and time, and μ is the position of the pump relative to the probe. If both profiles are Gaussian, then the resulting convolution is also Gaussian[113] with a convoluted

width,

$$w_S = \sqrt{{w_P}^2 + {w_N}^2}. \tag{2.2}$$

This type of experiment can provide insight into a couple different mechanisms related to the carrier dynamics. In uniform samples, we can observe the diffusion of the injected carrier distribution and in non-uniform samples, as with lateral heterostructures, this method can be used to gain insight into the channels of drift transport. Each will be explained in more detail below.

2.3.1 Photocarrier Diffusion

Typically, in isotropic samples without any external fields present, the transport of injected carriers is dictated strictly by the density gradient. With an initial Gaussian profile, consistent with the shape of the pump spot, the carrier distribution will spread radially outward from the injection site[114;115]. This is a simple diffusion process that follows the diffusion equation,

$$\frac{\partial N(r,t)}{\partial t} = D\frac{\partial^2 N(r,t)}{\partial r^2}, \tag{2.3}$$

where D is the diffusion coefficient, which is assumed to be a constant with dimensions of area per time. In uniform 2D samples, the injection depth of the laser spot is far greater than the sample thickness and thus allows us to consider only planar diffusion. If this diffusion is then also isotropic, we can mathematically treat the injected carrier density in 1D, with a Gaussian distribution,

$$N(x,t) = \frac{N_0}{w(t)\sqrt{2\pi}} e^{-\frac{1}{2}(\frac{x}{w(t)})^2}, \tag{2.4}$$

with $w(t)$ representing the time-dependent width of the distribution. It can be shown that the squared width depends linearly on time as,

$$w^2(t) = w_0^2 + 2Dt, \tag{2.5}$$

satisfies the diffusion equation, with w_0 being the initial width of the distribution. This can then be translated to a FWHM by,

$$FWHM = 2\sqrt{2\ln(2)}w, \tag{2.6}$$

making the squared width,

$$w^2(t) = w_0^2 + 16\ln(2)Dt \approx w_0^2 + 11.09Dt. \tag{2.7}$$

We can then track the squared width of the measured spatial profile as a function of the delay time to find the diffusion coefficient for injected photocarriers in the sample. It is important to note that this treatment of the diffusion process does not take into account the recombination rate of the injected carriers. Ultimately, any decay of the signal due to recombination does not affect the spatial component of the distribution. This leaves the width of the distribution unchanged by the recombination process.

The extracted diffusion coefficient, D, along with the photocarrier lifetime, τ, can then be used to infer other material properties. The diffusion length can be found by,

$$L = \sqrt{D\tau}. \tag{2.8}$$

Important to electronic applications is the carrier mobility as it is essentially a measure of how well carriers move within a material. The diffusion coefficient is related to mobility by the Einstein relation,

$$\frac{D}{\mu} = \frac{k_B T}{e}, \tag{2.9}$$

with k_B being the Boltzmann constant, T the sample temperature, and e the elementary charge.

2.3.2 Photocarrier Drift

In the case of non-uniform samples or when there is an externally applied electric field, many of the assumptions used in the previous section no longer hold. In many regards, this is because there are now different mechanisms present. For example, in photodiodes and photovoltaic (PV) devices, there is an applied voltage across the material that leads to charge separation of injected electron-hole pairs. These separated charge carriers then travel in opposite directions to their respective terminals. This type of transport is dictated by the electric field as compared to the density gradient, and is called drift transport. The drift velocity can be found by,

$$v_d = \mu E \tag{2.10}$$

where μ is the carrier mobility, and E is the electric field strength.

Another type of drift transport can occur with Dexter energy transport processes, where both types of charge carriers move in the same direction across a junction. Here, it becomes exciton drift as a result of the built-in potentials within the structure. Both of these drift mechanisms can be observed by spatiotemporally resolved pump probe experiments as outlined in Fig. 2.6. The experimental setup, in this case, is exactly the same as in the previous subsection. The only difference is that now the carrier distribution undergoes a drift process that causes it to move over time. Fig. 2.6(a) shows how the distribution would be expected to change if there is roughly uniform charge separation. Here, the different peaks would actually represent the movement of electrons and holes separately. Fig. 2.6(b) depicts the case of exciton transport, where the bound electron-hole pairs move in a singular direction.

In both cases, the distribution still undergoes a diffusion process and thus can be described by the Fokker-Planck equation, which is often used to describe systems that undergo a combination of drift and diffusion processes. In 1D, this equation is given by,

$$\frac{\partial}{\partial t}[N(x,t)] = -\frac{\partial}{\partial x}[\rho(x,t)N(x,t)] + \frac{\partial^2}{\partial x^2}[D(x,t)N(x,t)] \tag{2.11}$$

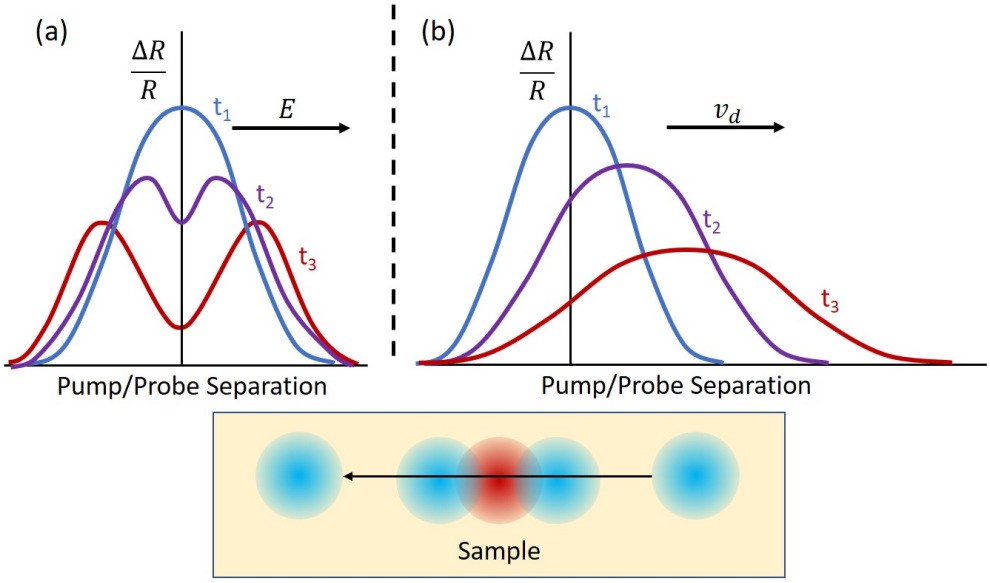

Figure 2.6: Expected spatial profiles for a carrier distribution undergoing different drift transport processes. (a) An applied electric field causes charge separation. The distribution will then split with two peaks representing their respective carriers. (b) Exciton drift causes the whole distribution to move in one direction.

where $\rho(x,t)$ describes the drift process and $D(x,t)$ the diffusion process.

Chapter 3

Vertical Heterostructures Formed by Monolayer TMDs

As discussed in Chapter 1, the most prevalent and widely studied type of heterostructure in flat land is the layered, vdWs heterostructure. In these structures, different materials can be stacked on top of one another, adhering only by the relatively weak vdWs force. One of the main advantages of these heterostructures is the lack of chemical bonding at the interface, which allows for different layered materials to be combined without much concern for lattice matching. This chapter will look at studies involving 3 different TMD-TMD vertical heterostructures. The first explores trion formation in a structure formed by stacking MLs of $MoSe_2$ and WS_2. Here, common to most TMD-TMD heterostructures, type-II band alignment facilitates charge separation leading to trion formation in WS_2. Then, carrier dynamics are examined in two heterostructures that contain less common TMD MLs. These two heterostructures, WSe_2-$MoTe_2$ and MoS_2-ReS_2, are predicted and found to exhibit type-I band alignment facilitating exciton transfer across their respective junctions.

3.1 Trion Formation in Type-II $MoSe_2$-WS_2 vdWs Heterostructure

One of the prominent features of TMD MLs is strong electron and hole interactions as a result of reduced dielectric screening from the low dimensionality. This leads to strongly bound excitons with large binding energies on the order of hundreds of meV[27;28]. Such strong Coulomb interactions in these materials can also lead to charged exciton formation, known as trions. These trions have been observed mostly at cryogenic temperatures, but can also be induced by gate-doping[29], photoionization of impurities[116], different substrates[117], or functionalization layers[118]. This section looks at the formation of trions at room temperature in a vertical heterostructure formed by

MLs of $MoSe_2$ and WS_2. The type-II band alignment between these layers facilitates charge separation, resulting in excess electrons in WS_2. The excited excitons and transferred electrons interact forming these trions. This is observed by an addition peak in the PL spectra of the heterostructure, not seen in isolated WS_2. We also deduce a zero-density trion binding energy of 62 meV. This study was published in the journal, ACS Nano[119].

3.1.1 Sample Fabrication and Characterization

For the samples fabricated in this experiment, monolayers of both $MoSe_2$ and WS_2 were exfoliated onto flexible, transparent polydimethylsiloxane (PDMS) substrates. Monolayers were found using an optical microscope and initially identified by optical contrast. Then, using a specialized microscope equipped with long working distance objective lenses and micro-manipulators, the monolayers are transferred to a Si/SiO_2 substrate, one on top of the other. After stacking these monolayers, as shown in Fig. 3.1, the sample is annealed at 200°C for 2hrs in an Ar/H_2 (100sccm/5sccm) environment with a base pressure of 3 torr. The annealing process helps to clear the heterostructure of trapped contaminants, providing better coupling between the two layers. The fabrication process is highlighted in more detail in A.1.

Using the sample described above, PL spectra were taken for both individual monolayers and the overlapping heterostructure region. The sample was excited using a continuous-wave (CW), 405 nm laser and the resulting luminescence was collected by a Horiba iHR550 imaging spectrometer. Figure 3.2 shows the PL spectra of the aforementioned regions, WS_2 (blue), $MoSe_2$ (red), and the heterostructure (black). The individual monolayers are found to have peaks at 1.58 eV ($MoSe_2$) and 2.01 eV (WS_2), and both have widths of about 50 meV. This is consistent with previously reported values[120–125], and also confirms the ML thickness.

3.1.2 Results and Discussion

There are a few clear differences between the individual monolayer spectra and the heterostructure spectrum. First, there is a huge quenching (factor of 23) of the WS_2 monolayer peak in the het-

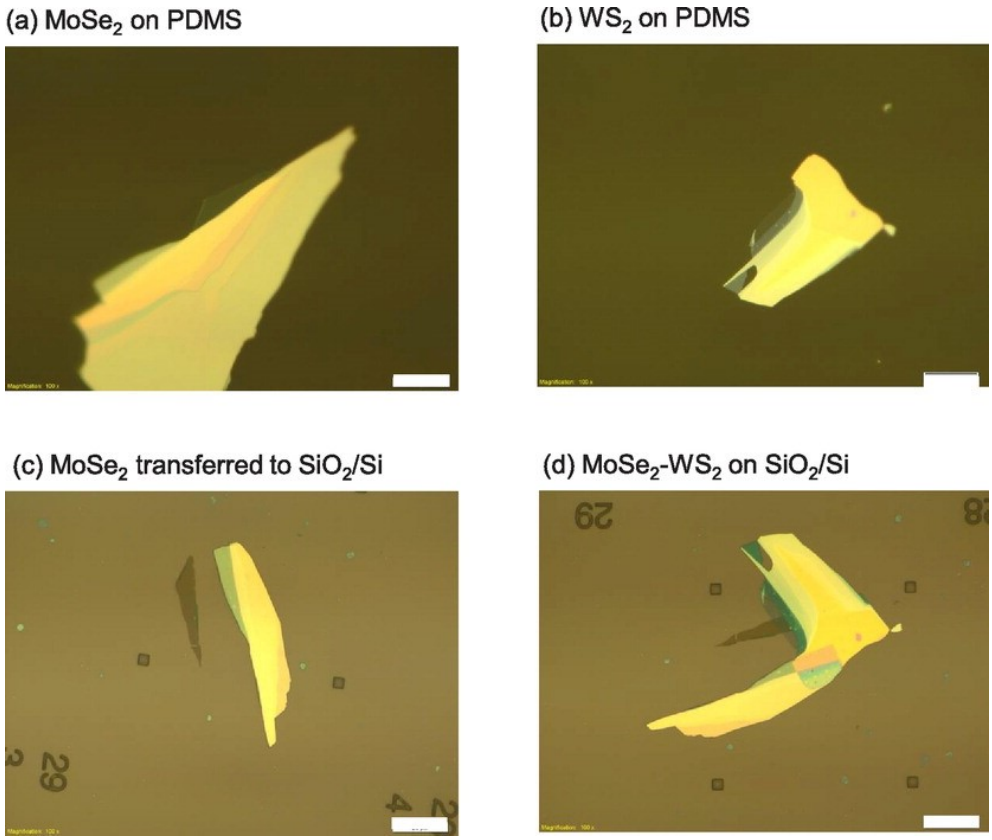

Figure 3.1: Optical images of the $MoSe_2$-WS_2 heterostructure sample at different steps of fabrication. (a,b) Images of the $MoSe_2$ and WS_2 monolayer samples on the PDMS substrates. (c) Image of the MoS_2 sample after being transferred to a Si/SiO_2 substrate. (d) Image of the heterostructure after the transfer of the WS_2 sample. The scale bars are 20 μm. Reproduced with permission from ACS Nano 2015 9 (6), 6459-6464. Copyright 2015 American Chemical Society.

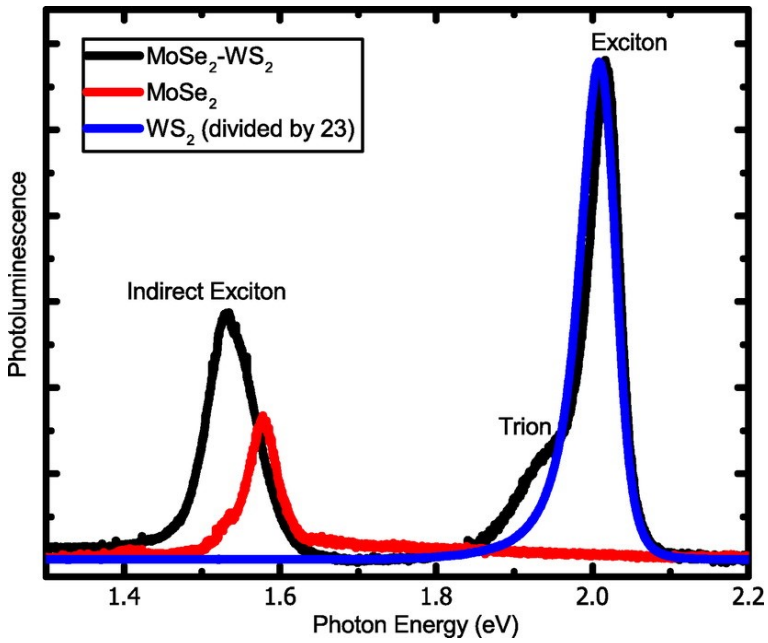

Figure 3.2: Photoluminescnece spectra measured from WS_2 (blue), $MoSe_2$ (red), and the heterostructure (black). Reproduced with permission from ACS Nano 2015 9 (6), 6459-6464. Copyright 2015 American Chemical Society.

erostructure, which is largely believed to be the result of efficient interlayer charge transfer across the junction. There is also the peak of the indirect exciton, from the recombination of electrons in the WS_2 layer and holes in the $MoSe_2$ layer. A slight broadening of this peak is from the quenched $MoSe_2$ peak. Lastly, the additional bump next to the WS_2 peak is believed to be due to the formation of trions, and is the primary focus fo this study. As shown in Fig. 3.3, trion formation, often referred to as charged excitons, are formed in the WS_2 layer as electrons are transferred from the $MoSe_2$ layer.

The type-II band alignment stimulates charge separation in the heterostructure leading to an excess of electrons in the WS_2 layer and an excess of holes in the $MoSe_2$ layer. The PL peak representing these trions is shifted from the WS_2 peak as a result of the extra binding energy associated with the excess electron. To extract this binding energy and learn more about the suspected trion peak, we excite the heterostructure with different pump powers, as shown in Fig. 3.4. Here, each dataset is fit with a two Gaussian functions. The red and blue curves in each are the individual Gaussian fits to the exciton and trion peaks, respectively, with the orange curve representing the

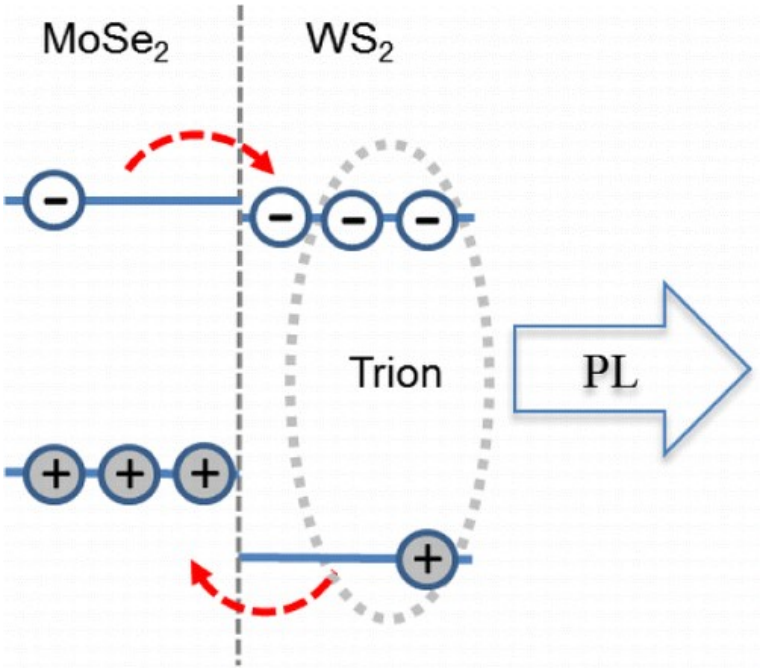

Figure 3.3: Expected band alignment of the $MoSe_2$-WS_2 heterostructure. Electrons in $MoSe_2$ transfer to WS_2 creating bound trions. The resulting recombination of these particle clusters results in a shifted peak in the PL. Reproduced with permission from ACS Nano 2015 9 (6), 6459-6464. Copyright 2015 American Chemical Society.

cumulative fit.

From these fits we can reliably separate the trion peak from the exciton peak. The peak energy as a function of the excitation power for the exciton and trion are shown in Figs. 3.5(a,b). Here, we find with increasing the the excitation level that energies of both peaks decrease. The change in the trion peak energy (E_T) is noticeably larger than that of the exciton peak (E_X). Taking the difference of the two, $E_X - E_T$, we find that the separation increases linearly with excitation level, shown in Fig. 3.5(c). This energy difference is known as the trion binding energy, and is the required energy to separate the trion into an exciton and free electron or hole. The binding energy increases with the excitation level, because the free charge needs to be released above the Fermi surface where there are unoccupied states. Increasing the excitation level increases the Fermi surface, and thus the binding energy as well.

From the linear extrapolation, we find a trion binding energy of 62 ± 2 meV at zero excitation power. This is slightly larger than previous reports on trions in WS_2 [121;122]. It is interesting to note

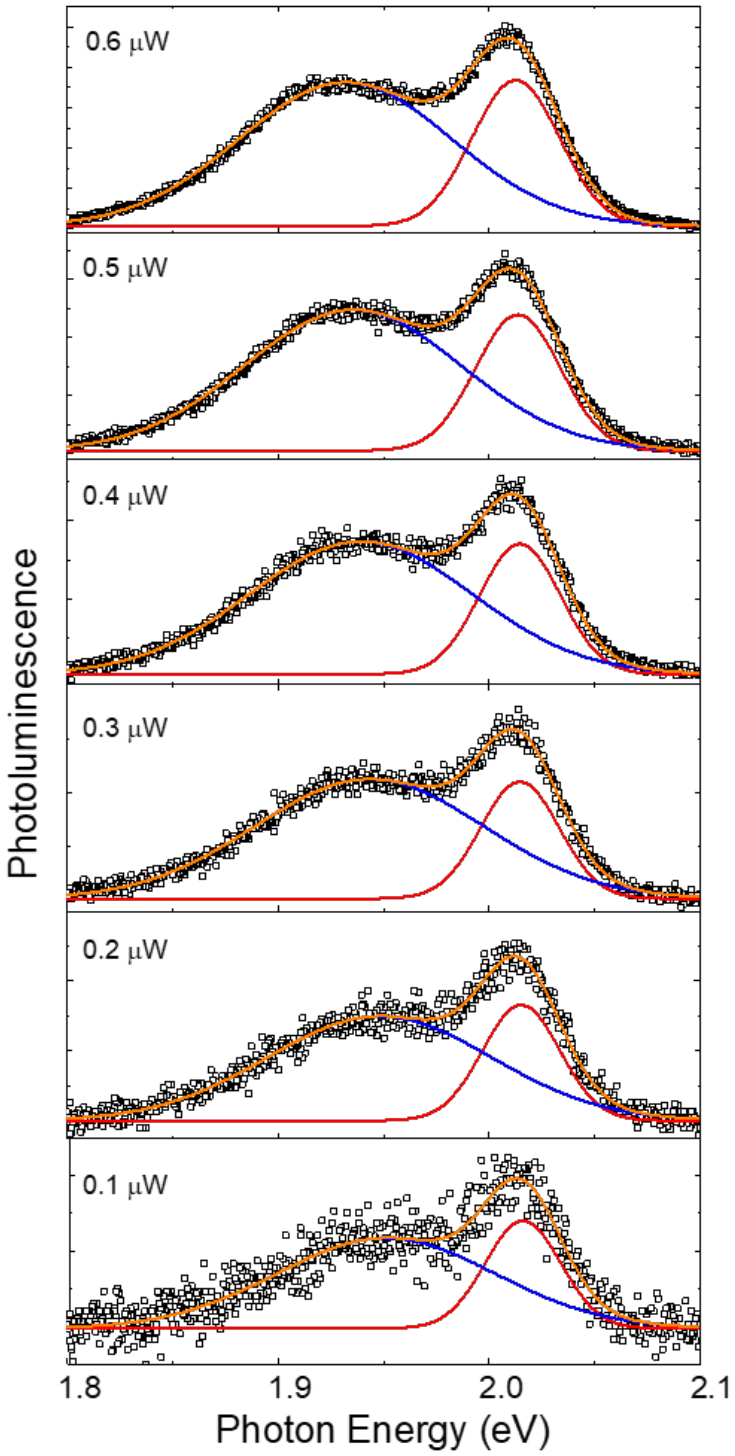

Figure 3.4: Photoluminescence spectra measured from the heterostructure for different pump excitation powers. The red and blue curves are Gaussian fits to the exciton and trion peaks respectively. The orange curve is the cumulative fit from the two Gaussian functions. Reproduced with permission from ACS Nano 2015 9 (6), 6459-6464. Copyright 2015 American Chemical Society.

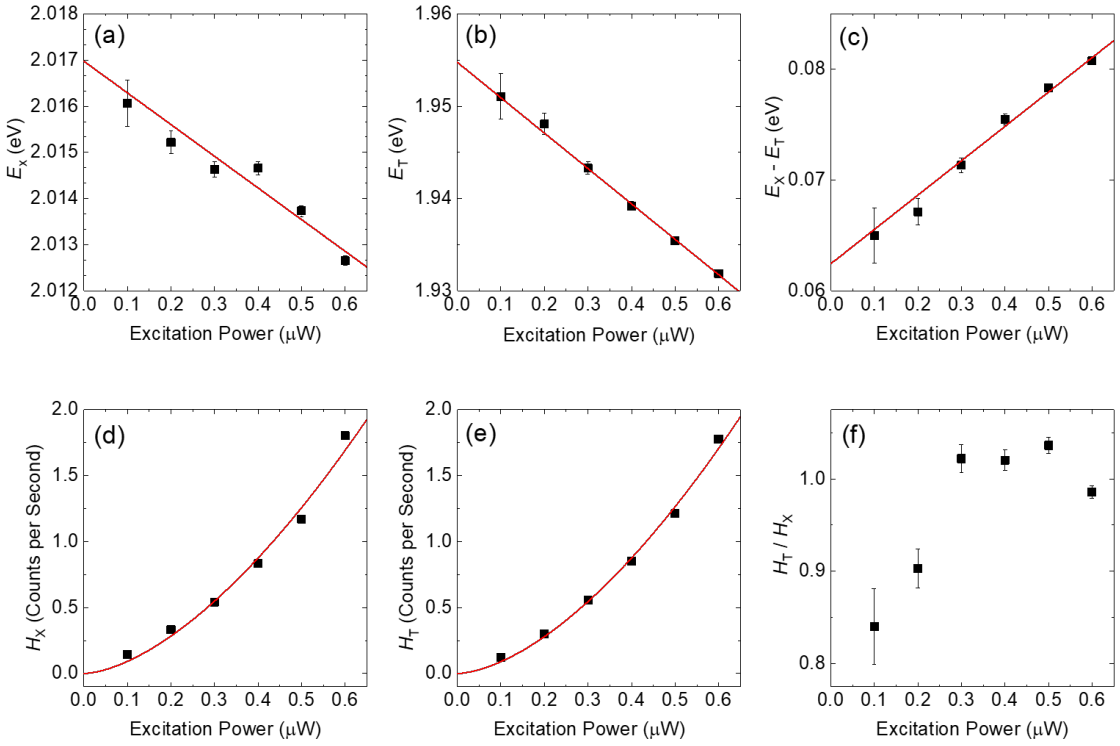

Figure 3.5: Power dependent trends from 3.4 (a,b) The peak energy measured from the exciton and trion peaks as a function of the excitation power. (c) The difference between (a) and (b). (d,e) The height of the exciton and trion peaks as a function of excitation power. (f) The ratio of the peak heights found in (d) and (e). Reproduced with permission from ACS Nano 2015 9 (6), 6459-6464. Copyright 2015 American Chemical Society.

that this binding energy is consistent with the conduction band offset (60 meV) in the heterostructure[126].

We also look at how the heights of each peak, H_X and H_T, change with excitation power. The results are summarized in Figs. 3.5(d,e). We see that both peaks scale similarly in a super-linear fashion. The curves shown are fit using a power of about 1.6 in each case. This superlinear dependence is likely the result of defects in the materials which allow for nonradiative recombination and exciton trapping that can compete with radiative recombination[127–129]. With higher excitation powers, a higher portion of injected carriers recombine radiatively as the number of defects is more or less fixed. In Fig. 3.5(f), we also see that the ratio of the two peak heights is relatively constant with excitation power.

One would also expect to see evidence of trion formation in the $MoSe_2$ layer. The reason we do not observe this is likely due to a higher density of defect sites in $MoSe_2$ compared to WS_2. Monolayer WS_2 is commonly known to have very strong PL yield due to better growth methods that incur fewer of these defect sites. With fewer defect sites, charge carriers in WS_2 can more easily form both neutral and charged excitons instead of quickly recombining with defects as in $MoSe_2$.

The results observed in the $MoSe_2$-WS_2 heterostructure are a prime example of the charge transfer phenomena that can be seen in vdWs heterostructures. The type-II band alignment facilitates one type of electronic control in these atomically thin materials. Next, we will explore slightly more exotic combinations of TMD MLs layers that exhibit type-I band alignment.

3.2 Exciton Transfer in Type-I vdW Heterostructures

The above study involved one of the more common TMD heterostructures. It exhibited type-II band alignment, which drives charge separation at the interface. This type of band alignment is expected from, and has been observed in, all of the heterostructures formed by combinations of the four common TMD layers, MoS_2, $MoSe_2$, WS_2, and WSe_2 [74;77;79;101;126]. However, finding combinations of layered materials that form type-I alignment is essential for many different applications like ultrathin quantum wells, optical pumping and wavelength conversion devices. Presented here are two heterostructures formed by combining different TMD MLs that exhibit type-I band alignment. We find that the heterostructure with two similar crystal structures facilitates faster transfer dynamics than the one with dissimilar crystal structures.

3.2.1 2H-2H $MoTe_2$-WSe_2

The first type-I heterostructure we look at is formed by vertically stacking monolayers of $MoTe_2$ and WSe_2. In this case, each of the materials have a similar 2H crystal lattice.

In our experiments, the WSe_2-$MoTe_2$ heterostructure sample was fabricated in a similar fashion

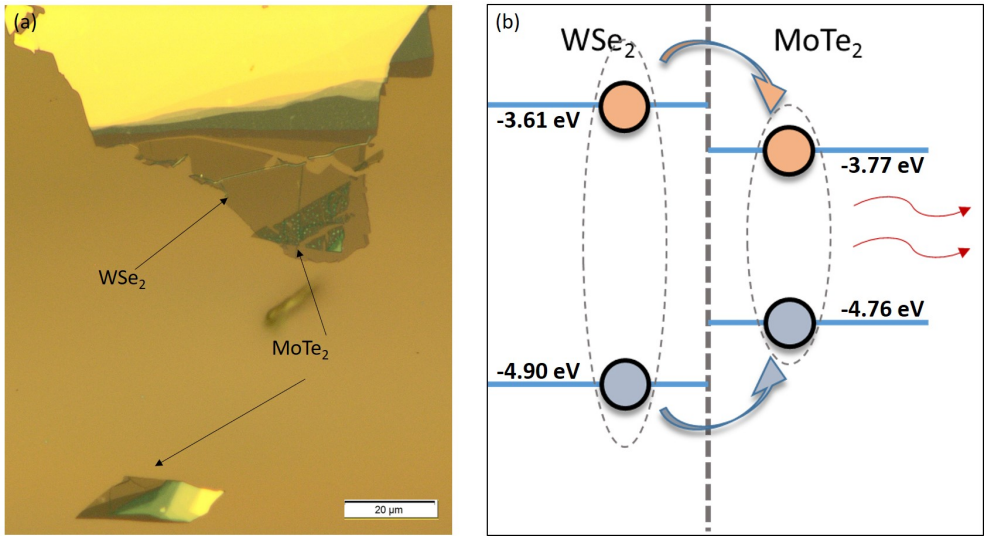

Figure 3.6: (a) Optical image of the $MoTe_2$-WSe_2 heterostructure sample. (b) Calculated band alignment between MLs of WSe_2 and $MoTe_2$. The orange and gray circles represent excited electrons and holes, respectively, which are expected to transfer to the $MoTe_2$ layer.

to the sample in the previous section, by mechanically exfoliating the MLs of WSe_2 and $MoTe_2$ onto PDMS substrates and sequentially transferring the layers to a Si/SiO_2 (90 nm) substrate. An optical image of the heterostructure sample is shown in Fig. 3.6(a). Due to the relative instability of ML $MoTe_2$ in ambient conditions [130], this layer was completely covered by the WSe_2 ML, in order to increase the longevity of the heterostructure sample. Isolated ML regions of both materials were also present on the same substrate in order to conduct a reliable comparison between each ML and the heterostructure. The sample was also annealed under the same conditions as the sample in the previous section. The thickness of each ML is determined by optical contrast (outlined in A.2).

A schematic of the calculated band alignment is shown in Figure 3.6(b). With both the CBM and VBM residing in $MoTe_2$, excitons induced in WSe_2 are expected to transfer to $MoTe_2$ where they recombine, emitting photons (red arrows) with an energy consistent with the optical bandgap of $MoTe_2$. In the following, we present experimental results on the photocarrier transfer process, which show unambiguously the type-I nature of the band alignment.

First, PL spectra were taken from the heterostructure, as well as, from both ML regions. As shown in Fig. 3.7, the spectra of the WSe_2 ML (red) and the heterostructure (blue) both show a peak located around 1.65 eV which is consistent with the A-exciton resonance in WSe_2 [34;131].

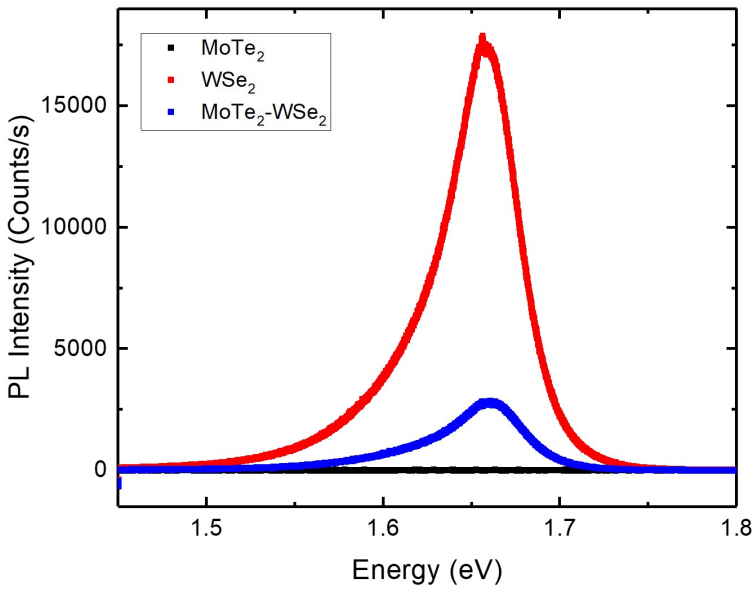

Figure 3.7: Photoluminescence spectroscopy data measured from WSe_2 (blue), $MoTe_2$ (red), and the heterostructure (black).

There is significant quenching of the peak, about 83% measured from the heterostructure region. This shows a good interface between the two layers, and provides initial evidence that electrons, holes, or both are likely transferring from WSe_2 to $MoTe_2$.

To observe the photocarrier dynamics in the heterostructure, we employed transient absorption microscopy experiments setup in reflection geometry. In these measurements, a tightly focused pump pulse of about 100 fs duration was used to excite certain regions of the sample. Then, a probe pulse, which arrives at the sample after the pump and overlaps in space with the pump spot, is used to monitor the dynamics of the photocarriers. The differential reflection of the probe, $\Delta R/R_0=(R-R_0)/R_0$, is measured as a function of the relative time delay between the two pulses. Here, R and R_0 represent the reflection of the probe pulse with and without the presence of the pump, respectively. By choosing the pump and probe photon energies, we can preferentially inject and detect photocarriers in different layers of the heterostructure sample.

We first study the photocarrier dynamics in ML $MoTe_2$. A 1.65 eV pump pulse with a peak injected fluence of 8.44 μJ cm^{-2} was used to excite the $MoTe_2$ ML. Based on the absorption

coefficient of bulk $MoTe_2$2 for this photon energy, 2.5×10^7 m^{-1}, the pump fluence corresponds to an injected photocarrier density of about 4.4×10^{11} cm^{-2}. The differential reflection of a 1.31 eV probe pulse is then measured for different delay times, and can be seen as the gray squares in Fig. 3.8. Note that both the pump and the probe photon energies are significantly larger than the optical bandgap of $MoTe_2$ of about 1.1 eV. The rising of the signal can be modeled by the integral of a Gaussian function with a FWHM of 0.63 ps, as indicated by the black curve in Figure 3.8. This rising time is slightly slower than the instrument response time of about 0.4 ps, which can be attributed to the time it takes for the photocarriers to relax their energy from the injected energy states to the states coupled to the probe pulse. The decay of the signal after the first 1 ps can be fit by a bi-exponential function with two time constants of 2.8 and 28 ps, respectively. The short time constant could be attributed to the energy relaxation of photocarriers from the probed state to the band edges, while the long time constant gives the photocarrier lifetime.

Using this same procedure, we then measured the differential reflection signal from the heterostructure under the same conditions. Since the optical bandgap of ML WSe_2 is about 1.65 eV, the pump is expected to inject photocarriers in both layers, while the 1.3 eV probe should only sense photocarriers in $MoTe_2$. The result is shown by the blue squares in Fig. 3.8. The magnitude of the signal is about 7.5 times larger than that of $MoTe_2$, while the temporal shapes of the two are very similar. The white squares in Fig. 3.8 show the scaled signal from ML $MoTe_2$ (multiplied by 7.5), which shows that the signal from the heterostructure has a very similar rising time, with a small lag, and slightly slower initial decay. Furthermore, by bi-exponential fit (purple curve), the two time constants from the heterostructure measurement are 4.3 and 28 ps, with the long time constant matching the $MoTe_2$ ML very well.

These features are strong evidence of electron and hole transfer from WSe_2 to $MoTe_2$, as a result of the type-I band alignment shown in Fig. 3.6. First, without carrier transfer, the two measurements should yield identical results since carriers injected in WSe_2 would not be sensed by the probe. The larger signal observed in the heterostructure sample is induced by photocarriers transferred from WSe_2 to $MoTe_2$. The existence of carrier transfer is also consistent with the PL

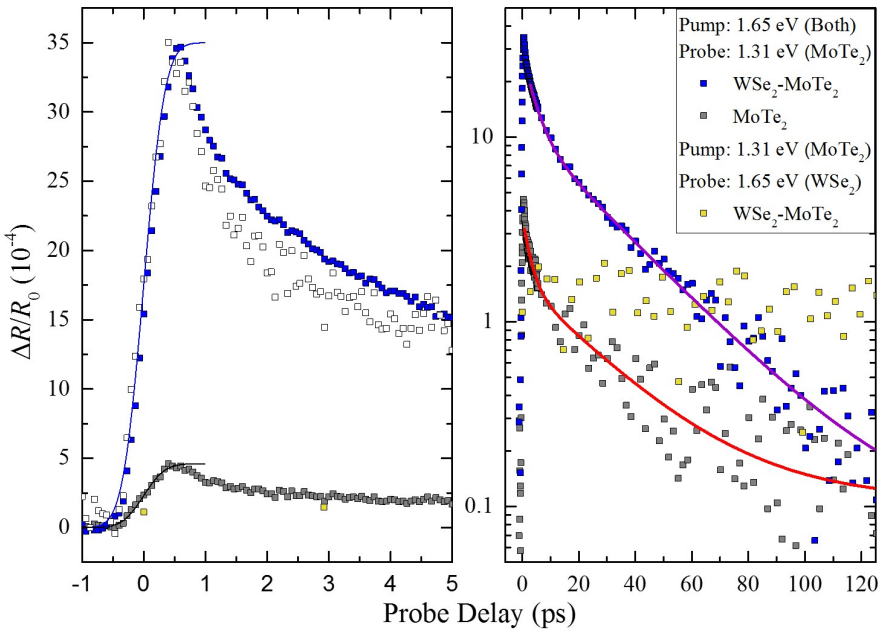

Figure 3.8: Differential reflection measurements using a 1.31 eV probe pulse and a 1.65 eV pump pulse. The blue squares were measured from the heterostructure and show a significantly higher signal than that measured from the isolated $MoTe_2$ ML (Grey Squares). The purple and red lines represent double exponential fits to the heterostructure and ML $MoTe_2$ data respectively. The yellow squares represent measurements on the heterostructure with the pump and probe switched, 1.65 eV probe and 1.31 eV pump. This is to probe carriers excited in $MoTe_2$ that might transfer to WSe_2.

quenching of WSe_2, shown in Fig. 3.7. Second, the carrier transfer occurs on a time scale shorter than the response time of the measurement. If the transfer were a slow process, the signal from the heterostructure would be expected have a slow rising part as dictated by the transfer rate. Third, the same decay time observed in the two samples indicates that both electrons and holes excited in WSe_2 transfer to $MoTe_2$, as dictated by the type-I alignment. If the alignment were type-II, only one type of carrier would transfer. Once the electrons and holes are separated in different layers, their recombination would be significantly suppressed, resulting in a longer lifetime of photocarriers in the heterostructure[79;132–134].

To ensure that no carriers, neither electrons nor holes, transfer in the opposite direction, *i.e.* from $MoTe_2$ to WSe_2, we used a 1.31 eV pump and probed at 1.65 eV. In this case, we expect to inject photocarriers in $MoTe_2$ only. The 1.65 eV probe matches the A-exciton resonance of WSe_2 providing the best differential signal from carriers in the WSe_2 layer. As shown by the yellow squares in Fig. 3.8, there is no noticeable signal from the heterostructure observed. It is also important to note that this signal is from a peak injected fluence of 16.9 μJ cm^{-2}, twice that of the other 2 curves in Fig. 3.8. With an absorption coefficient of 0.8×10^7 m^{-1}, this fluence corresponds to an injected density of 4.5×10^{11} cm^{-2}. If the band alignment were type-II, there would be charge separation and we would expect to observe a noticeable differential reflection signal due to either electrons or holes transferring to WSe_2 under these conditions.

To further confirm that the increased signal observed in the heterostructure is from photocarriers injected in WSe_2 that subsequently transfer to $MoTe_2$, we studied the dependence on the pump energy. Using a 1.31 eV probe, we varied the pump energy from 1.65 eV, the A-exciton resonance of WSe_2, to 1.55 eV. Figure 3.9 shows the differential reflection of the heterostructure for the different pump energies. The inset shows the peak signal as a function of the pump energy. It is clear the signal increases as the pump energy moves towards the exciton resonance of WSe_2. This indicates that as more photocarriers are injected in WSe_2, subsequently the observed carrier density in $MoTe_2$ also increases. The trend of this increase is fairly consistent with the energy dependence of the absorption coefficient in WSe_2[42].

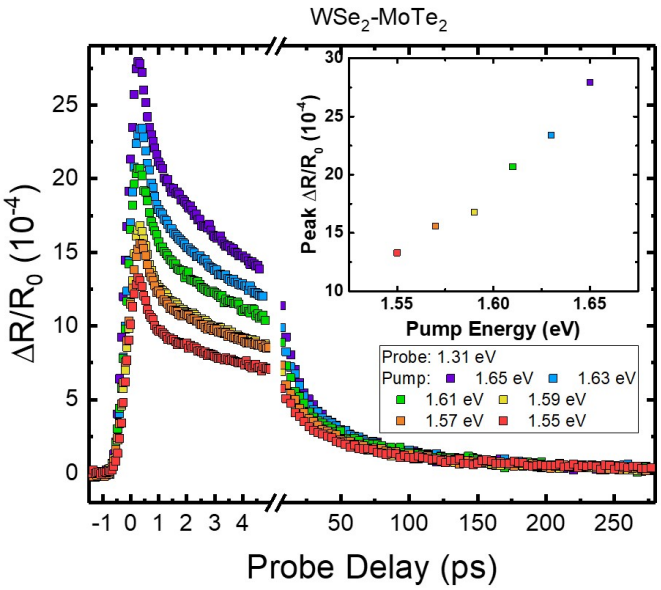

Figure 3.9: Pump energy dependence on the differential reflection of 1.31 eV probe measuring the heterostructure. The inset shows the peak differential reflection signal for the different pump energies.

Next, we looked at the carrier dynamics in WSe_2. Photocarriers were injected by a 2.1 eV pump in the WSe_2 ML and the heterostructure with a peak fluence of 4.22 μJ cm^{-2}. At this energy, WSe_2 has an absorption coefficient of 1.6×10^7 m^{-1}, which leads to an injected carrier density on the order of 1.4×10^{11} cm^{-2}. From Fig. 3.10, it can be seen that there is an initial fast decay in the heterostructure that is noticeably faster than the exciton decay in ML WSe_2. Fitting each data set with a bi-exponential function, the initial fast decay is about 0.84 $\pm$ 0.3 ps in ML WSe_2 compared to 0.66 $\pm$ 0.1 ps in the heterostructure, about a 20 percent decrease. This faster decay is almost certainly from carriers transferring from WSe_2 to $MoTe_2$, another indication of type-I band alignment. The right panel of Fig. 3.10 shows the dynamics on a longer time scale. The longer decay times are nearly identical at 33 and 29 ps, respectively. It is also important to note that the signal from the heterostructure is smaller in magnitude than that of the isolated WSe_2 ML. This is evidence that a significant portion of the photocarriers transfer on an ultrafast time scale, faster than the time resolution of our system of about 300 fs. These transfer dynamics are consistent with previous reports on TMD heterostructures that point to a coherent transfer process

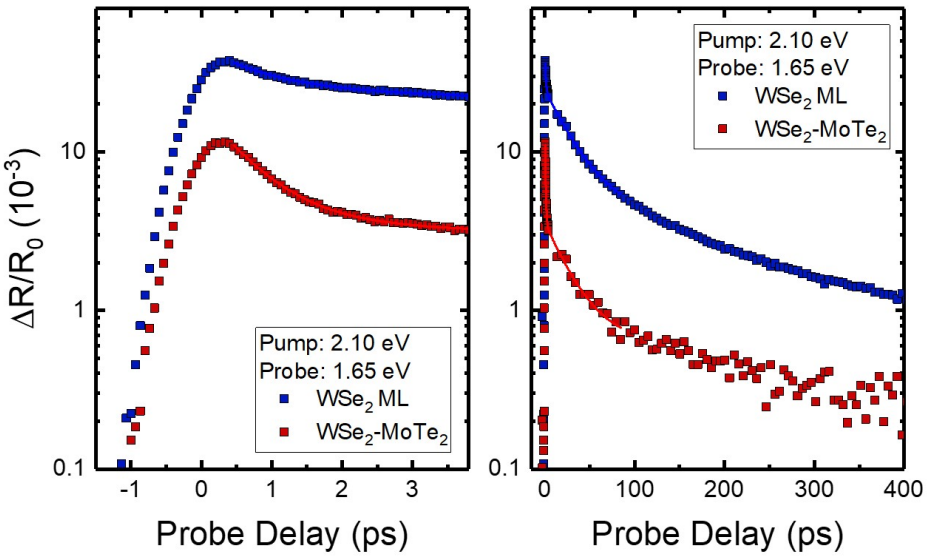

Figure 3.10: Short and long scale differential reflection measurements on WSe_2 ML (Blue) and the heterostructure (Red) using a 1.65 eV probe and 2.1 eV pump.

between layers.

3.2.2 2H-Distorted 1T MoS_2-ReS_2

The previous section discussed results on a heterostructure comprised of two materials with very similar lattice constructs, both having hexagonal, 2H, structures. In that heterostructure, as seen in other 2H-2H vdW heterostructures, we observed ultrafast exciton transfer from one material to the other. This transport was so fast that it was beyond the response time of our system of about 300 fs. This section will look at another suspected type-I heterostructure which is formed by combining two dissimilar crystal structures. In this case, the heterostructure is made from monolayers of 2H-MoS_2 and distorted 1T-ReS_2. This study was published as the cover article in the journal, Nanoscale Horizons[135].

Similar to the previous structure, the expected band alignment is found from first principle calculations, which were performed by our collaborators from Dr. Zeng's group at The University of Nebraska. In MoS_2, the VBM and CBM are found to be -5.91 eV and -4.25 eV, respectively.

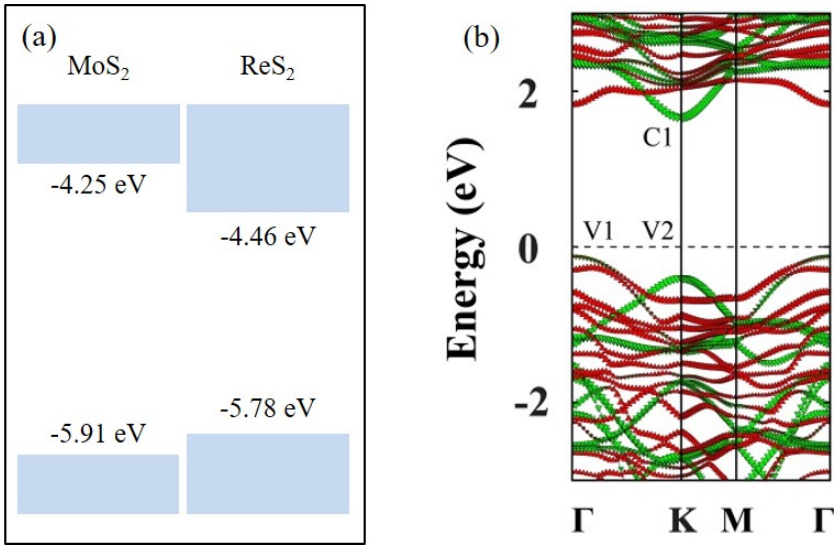

Figure 3.11: (a) Calculated band alignment of monolayer MoS_2 and ReS_2. (b) Calculated band structure of the MoS_2-ReS_2 heterosturcture. The red and green symbols represent contribution from MoS_2 and ReS_2, respectively. Reproduced from Ref. 135 with permission from The Royal Chemical Society.

In ReS_2, they are -5.78 eV -4.46 eV, respectively, resulting in type-I band alignment between the layers. Fig. 3.11(a) shows this band alignment. Fig. 3.11(b) shows the calculated band structure for the heterostructure. Here, the red symbols represent contributions from MoS_2, where as the green is contributions from ReS_2. The calculations shows that both the CBM and VBM in the heterostructure are contributed from ReS_2, predicting the type-I alignment at the junction.

Fabricating this heterostructure followed the same procedure used in the previous section, with both materials being mechanically exfoliated and transferred onto a 90 nm SiO_2/Si substrate. The sample was then annealed under the same conditions previously mentioned. An optical microscope image of the final sample is shown in Fig. 3.12(a).

To confirm the ML thickness of the materials, we utilized optical contrast and Raman spectroscopy. Figure 3.12(b) shows the green channel contrast measured along the yellow line in (a). The green channel is used as it provides a good standard for the contrast of various monolayers of about 12-13%, as shown in previous reports[136–138]. Our measurements are in agreement with the expected contrast of ML samples (see A.2).

The Raman spectroscopy results are shown in Fig. 3.12(c) for both MoS_2 (red) and ReS_2

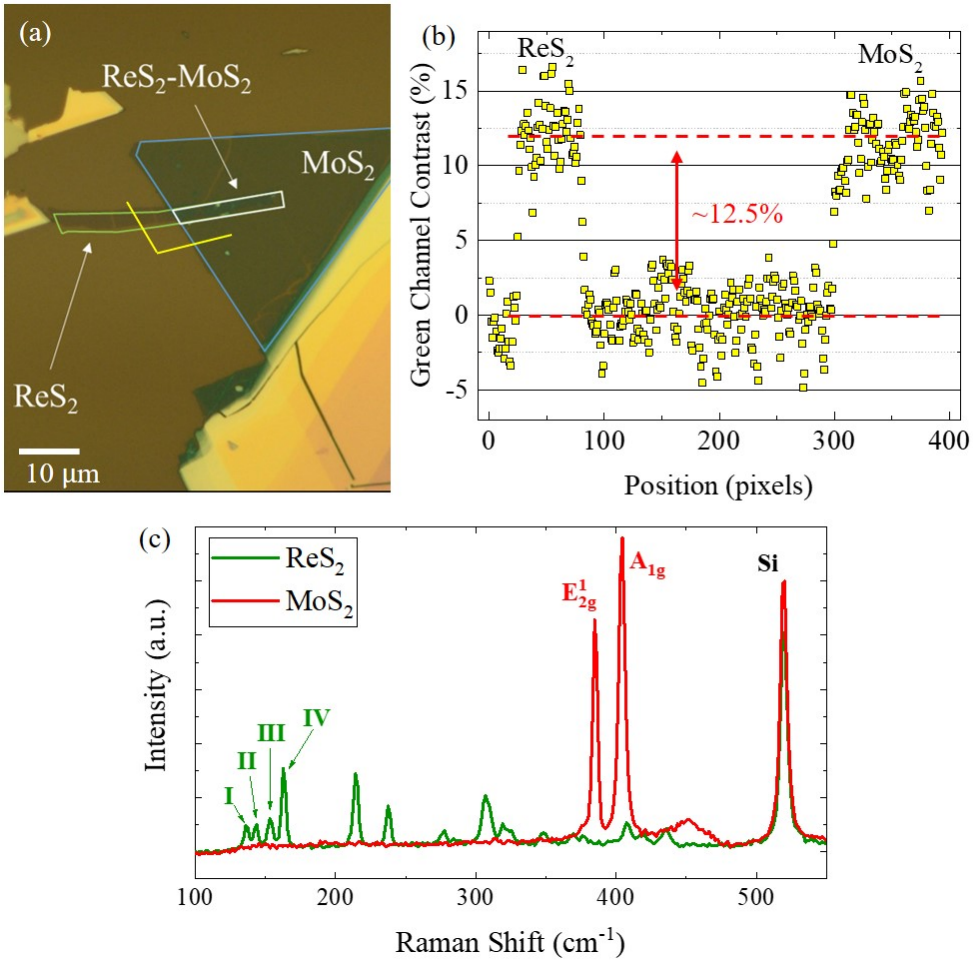

Figure 3.12: (a) Optical image of the MoS_2-ReS_2 sample. (b) Contrast measured from the green color channel along the yellow line in (a). (c) Raman spectra measured from MoS_2 (red) and ReS_2 (green) The large peak at a Raman shift of around 520 cm^{-1} is from the silicon substrate. Reproduced from Ref. 135 with permission from The Royal Chemical Society.

(green). Raman measurements were also used to further confirm monolayer thickness of both layers. In MoS_2 the separation between the E^1_{2g} and A_{1g} peaks is used to confirm the ML thickness[139]. For ReS_2, the separation between the peak labeled I and III in Fig. 3.12(c), also point to ML thickness (see A.3 for a more in-depth look at the Raman modes in both layers).

Now that we have established both layers to be monolayer,as expected, we again look at the injected carrier dynamics using transient absorption microscopy to measure the time dependent differential reflection. First, using a pump pulse with an energy of 1.67 eV and 300 fs duration, we inject carriers in a portion of the ReS_2 monolayer. Because the optical band gap of Re_2 is about 1.52 eV, these carriers are injected by inter-band absorption. We focus the laser spot through a 20$\times$ objective lens to a spot size of 2.2 μm, injecting carriers with a fluence of 7 μJ cm^{-2}. With an absorption coefficient of 8 $\times$ 10^6 m^{-1} (bulk value), we obtain a peak injected density of about 1.4 $\times$ 10^{11} cm^{-2}. We monitor the dynamics of these carriers by measuring the differential reflection of a 1.53 eV probe pulse. This is tuned slightly above the bandgap of ReS_2. The open red squares in Fig. 3.13, show the results of this experiment. We fit the decay of the signal using a single-exponential with a background. From this, we find a decay constant of 65$\pm$5 ps which is attributed to the recombination lifetime of the photocarriers. Similar results were observed when measuring the heterostructure region of the sample shown by the solid red squares in Fig. 3.13.

In this experiment on the heterostructure, the MoS_2 was neither pumped nor probed, as the lowest excitonic state in MoS_2 is at 1.85 eV. If the band alignment were type-II, however, we would expect to see a change to the measured dynamics as the MoS_2 layer would serve as a channel for charge transfer. Specifically, if the CBM (VBM) were lower (higher) in MoS_2 compared to ReS_2, electrons (holes) would be expected to transfer to MoS_2. This would results in a smaller magnitude of the signal (by about a factor of 2) due to the loss of one carrier type in ReS_2. We would also expect to see a longer carrier lifetime from indirect exciton formation across the junction as observed from other type-II heterostructures[79;101;132].

However, the lack of charge transfer is not itself proof of type-I band alignment, as poor interface quality could be a factor. TO rule this out, we next inject carriers in both ReS_2 and MoS_2 using

a 1.85 eV pump. This is tuned to the A-exciton resonance of MoS_2. We again inject carriers with a peak fluence of 7 μJ cm^{-2}, resulting in peak density of 4.8 $\times$ 10^{11} cm^{-2}. This is according to an absorption coefficient of 3 $\times$ 10^7 m^{-1} for MoS_2. Measuring the differential reflection of the same 1.53 eV probe, we would expect to see an increase in the signal measured from the heterostructure if there is type-I band alignment. The results are shown by the solid green squares in Fig. 3.13. We indeed see an increase of the signal, by a factor of 3, and the decay is also very similar to that of the ReS_2 monolayer, with a time constant of 62 ps (blue curve).

Using this more energetic pump, we also again measure the isolated ReS_2 monolayer, as shown by the open green squares in Fig. 3.13. Here, we do not see an increase in the signal magnitude which confirms that the increased signal from the heterostructure is not from addition carriers injected in ReS_2 due the increased pump energy. This signal is very similar to that measured with the 1.67 eV pump confirming that the signal from ReS_2 is rather insensitive to the the pump photon energy in this range. This is consistent with other observation that the absorption coefficient in ReS_2 does not change significantly in this range as well.

To provide further evidence of the type-I band alignment between these two layers, we also probe the MoS_2 layer. Here, we measure the differential reflection of a 1.85 eV probe, matching the A-exciton of monolayer MoS_2. The results are summarized in Fig. 3.14. First, using a 3.06 eV pump, we inject carriers in MoS_2 with fluence of 12 μJ cm^{-2}. With an absorption coefficient of 1.5 $\times$ 10^8 m^{-1}, this corresponds to an estimated injected density of 3.4 $\times$ 10^{12} cm^{-2}. The results are shown as the solid black squares in Fig. 3.14. We observe a differential reflection signal on the order of 10^{-3}.

Next, using a 1.53 eV pump, we inject carriers in the ReS_2 layer of the heterostructure, with a fluence of 33 μJ cm^{-2}. This corresponds to a peak injected density in ReS_2 of 7.6 $\times$ 10^{11}. If the band alignment were type-II, electrons or holes would transfer to MoS_2. Given the fairly high injected carrier density, these transferred carriers would be expected to result in a differential reflection signal on the order 10^{-4}, using a 1.85 eV probe. However, as shown by the open squares in Fig. 3.14, no such signal is observed. This further confirms a lack of charge transfer from ReS_2

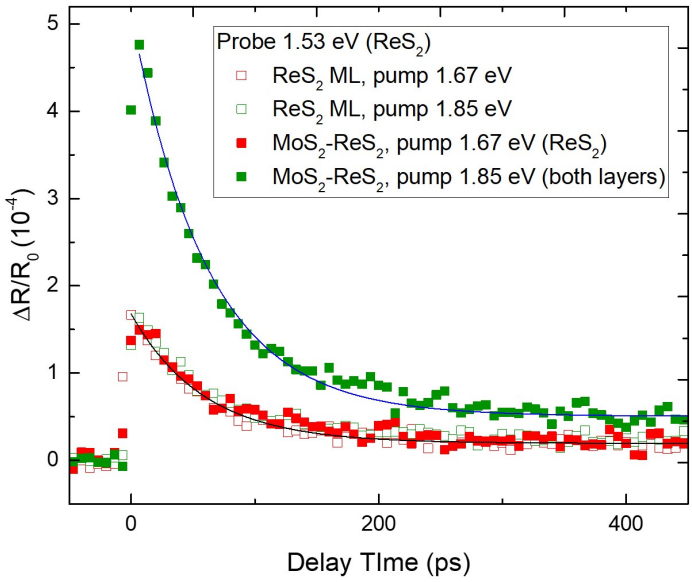

Figure 3.13: Differential reflection of a 1.53 eV probe measured from ML ReS_2 (open symbols) and the MoS_2-Res_2 heterostructure (closed symbols) for different pump energies, 1.57 eV (red symbols) and 1.85 eV (green symbols). Reproduced from Ref. 135 with permission from The Royal Chemical Society.

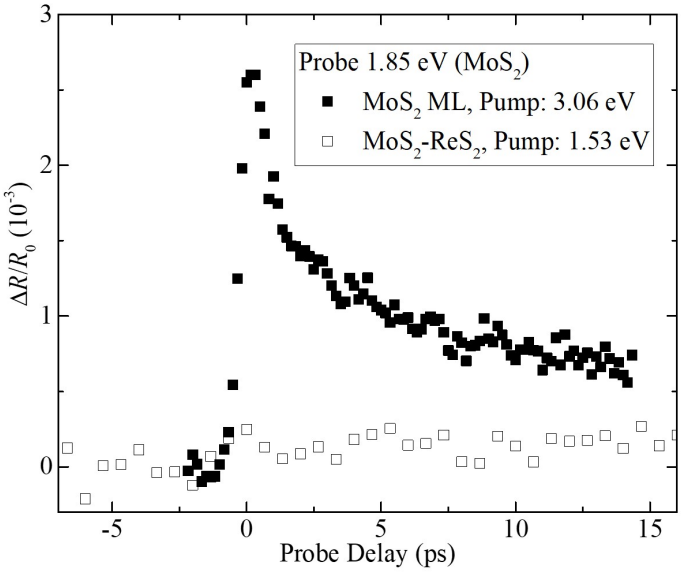

Figure 3.14: Differential reflection of a 1.85 eV probe as a function of probe delay. The black squares represent the measurements from ML MoS_2 using a 3.06 eV pump. The white squares represent the measurements from the heterostructure using a 1.53 eV pump to excite carriers only in the ReS_2 layer. Reproduced from Ref. 135 with permission from The Royal Chemical Society.

to MoS_2.

Finally, with the confirmed observation of type-I band alignment exhibited by this heterostructure, we can study the interlayer transfer process of photocarriers in this configuration. These results are outlined in Fig. 3.15. In this figure, all the differential reflection signals are normalized in order to facilitate a visual comparison. First, a 1.85 eV pulse with a peak fluence of 7 μJ cm^{-2} was used ot pump the heterostructure. Based on the absorption coefficients of each of the monolayers, the peak density of injected photocarriers in MoS_2 and ReS_2 are 4.8×10^{11} cm^{-2} and 1.3×10^{11} cm^{-2}, respectively. Probing the ReS_2 layer with a 1.53 eV pulse, we monitored the evolution of the photocarrier population in that layer and hence time resolved the transfer process. In Fig. 3.14, the solid and open green squares represent the measurements from this configuration as observed from the heterostructure and monolayer ReS_2, respectively. We found a rather slow rise of the signal observed from the heterostructure. The contribution of photocarriers directly injected in ReS_2 can be isolated by the control experiment on monolayer ReS_2 under the same

experimental conditions. The actual magnitude of the signal measured in ReS_2 is about one third that from the heterostructure, which is consistent with the ratio of the carriers injected in the two layers. Clearly, the rising of the signal is much faster in ReS_2, confirming that the slower rise time observe from the heterostructure originates from the transfer of photocarriers across the interface. We fit the rising part of the signal using,

$$N_1[1 - exp(-t/\tau_T)] + N_2, \tag{3.1}$$

where N_1 and N_2 represent the initial photocarrier densities in the MoS_2 and ReS_2 layers, respectively, and, τ_T represents the transfer time. As shown by the green line in Fig. 3.15, this expression can satisfactorily describe the data with a transfer time of 1.3 ± 0.1 ps.

Alternative to observing the photocarrier build up in ReS_2, we also monitor the photocarrier population leaving the MoS_2 layer of the heterostructure. Using a 3.06 eV pump pulse, we inject photocarriers in the heterostructure and probe the MoS_2 layer with a 1.85 eV probe. Carriers in ReS_2 are not sensed by this probe. The results are shown as the blue squares in Fig. 3.15. The signal decays single-exponentially with a decay constant of 1.1 ± 0.2 ps, as indicated by the blue curve. The decay is significantly faster than that observed from monolayer MoS_2 under the same conditions (black squares in Fig. 3.14), which represents the exciton recombination time. This fast decay is due to the transfer of photocarriers to the ReS_2 layer, and the time constant very closely matches the transfer time, τ_T, observed in the build up of photocarriers in ReS_2.

Several studies on other TMD heterostructures, including the results in the previous subsection, have shown that transfer processes in these ultrathin structures occurs on a time scale shorter than 100 fs[78;79;101]. This ultrafast process is thought to be facilitated by quantum coherence. The transfer process in this heterostructure, however, is noticeably slower, occurring on a ps time scale. The most notable difference between this heterostructure and the others is the difference in crystal structures. In each of the previous studies, the two layer each have the same 2H crystal structure. Here, the heterostructure is formed by MoS_2 with a 2H structure and ReS_2, which has a distorted 1T structure. It is possible that difference in lattice structures suppresses the coherent transfer

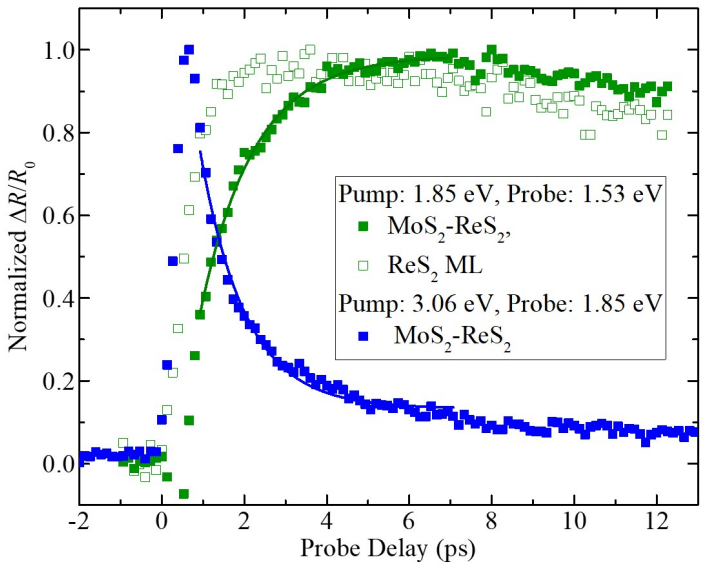

Figure 3.15: Normalized, time-dependent differential reflection signals on a short time scale to show the transfer dynamics. The green squares are measured using a 1.53 eV probe and 1.85 eV pump in ML ReS_2 (open) and the heterostructure (closed). The blue squares are measured from ML MoS_2 using a 1.85 eV probe and 3.06 eV pump. The lines represent fits to the measured data. The green line is fit to eq. 3.1 and the blue is exponential decay fit. Reproduced from Ref. 135 with permission from The Royal Chemical Society.

process, resulting in a slower incoherent transfer process.

3.3 Summary

The experimental observation of Type-I aligned heterostructures in the landscape of vdWs heterostructures is of critical importance for the broader applications of 2D materials. These studies help to introduce the possibility for quantum well applications at the atomic limit which could prove pivotal for future developments in laser technologies, wavelength manipulation and more. Most notably, ultrathin semiconducting structures that can combine different types of band alignment, will provide unprecedented opportunities to control charge transport on an atomic scale.

The above studies help to initiate a thorough platform for the development of band engineering at an atomic level, highlighting different types of band alignment, as well as possible effects due to differences in crystal structures. We found that the charge separation found in the combination of $MoSe_2$ and WS_2, can lead to exotic excitonic behavior with the formation of charged excitons called trions. We also observed the photocarrier dynamics in two heterostructures, WSe_2-$MoTe_2$ and MoS_2-ReS_2, which both exhibited properties consistent with type-I band alignment, facilitating exciton transfer across the junction.

We also observed a noticeable difference in the transfer time seen from the two type-I structures. We believe this to be the results of different crystal structures. The WSe_2-$MoTe_2$ heterostructure is formed by two layers with similar 2H crystal structures. As seen in other similar 2H-2H heterostructures, this results in a transfer process shorter than 100 fs, facilitated by quantum coherence. The MoS_2-ReS_2 heterostructure has a 2H-Dist. 1T combination that results in a much slower transfer process, on the order of 1 ps. This difference in crystal structure likely breaks the coherence, resulting in slower photocarrier transfer.

Chapter 4

2D Amorphous-Crystalline Semiconducting Heterostructures

After exploring various TMD-TMD vertical heterostructures, we now shift the focus to another type of vertical heterostructure, between a TMD monolayer and an ultrathin amorphous semiconductor layer. It is important to look at unique heterostructures formed between different lattice structures to learn more about the mechanisms that facilitate charge and energy transfer in these low dimensional systems. In the previous chapter, for instance, it was shown that a heterostructure with similar lattice structures showed faster energy transfer than one with dissimilar lattice structures. Studies have shown that charge transfer mechanisms in various TMD-TMD heterostructures are likely dictated by quantum coherence and effective coupling between donor and accepter states which reside in opposite layers[79;107]. Previously, it was assumed that these vdWs structures would exhibit incoherent transfer due to suspected weak interlayer coupling and relatively large interfacial spacing compared to chemically bound structures.

Recently, the effect of layer-coupled states has been explored in TMD homobilayers[109;140]. In these the structures, the individual layers constitute a perfect lattice match. The results suggest that it is likely states in the Q or Γ valleys are coupled between layers and could be a dominant mechanism for ultrafast transfer processes. If these layer-coupled states are responsible for ultrafast transfer, it would imply that similar efficient transfer would not occur in layered combinations with significantly different lattice structures. It is thus interesting to study the heterostructure between 2D crystalline and amorphous layers, as it presents an extreme case for exploring this hypothesis.

However, due to the lack of studies on amorphous materials in the 2D realm and specifically amorphous black phosphorus (aBP), the material used in our study, we will begin by examining properties of aBP thin films. This will include samples of different thicknesses of 2, 5, and 10

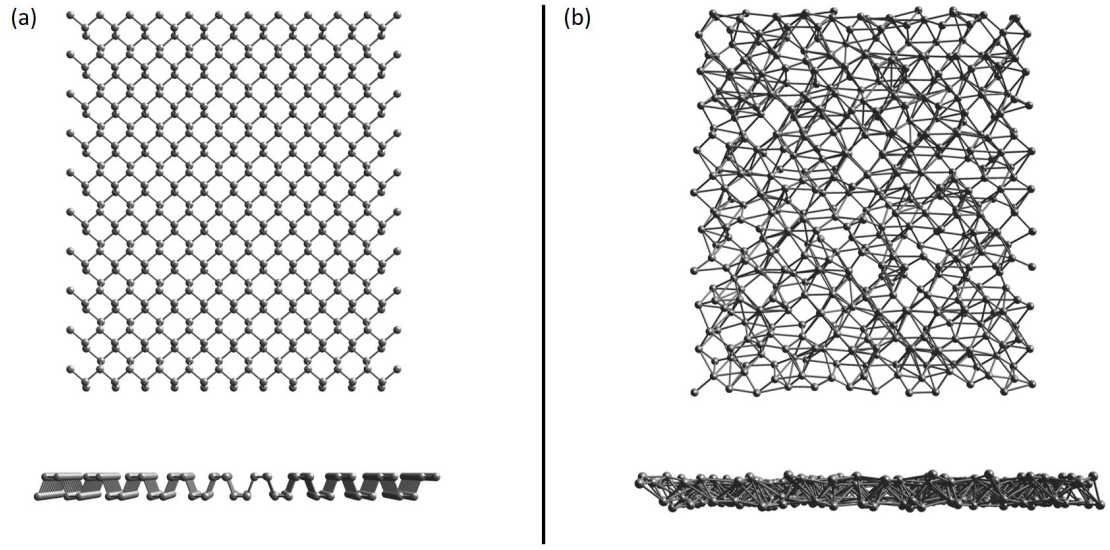

Figure 4.1: Top and side view of the lattice structure of (a) crystalline and (b) amorphous black phosphorus.

nm. Once we establish an understanding for the aBP films, we will look at the interaction of photocarriers between a TMD ML and the thinnest of these amorphous sheets. The resulting charge transfer phenomena will be explored in detail.

4.1 Introduction to Amorphous Semiconductors

Amorphous semiconductors are of great importance in the electronics industry. They are an interesting class of materials, as their amorphous structure omits one of the most fundamental characteristics utilized in solid state physics, crystallinity. The difference in structure is highlighted in Fig. 4.1. This shows the lattice structure of crystalline (a) and amorphous (b) black phosphorus, the material studied in this chapter. Here, in a stable crystalline form, BP exhibits a puckered hexagonal structure [14], where as the amorphous form, by nature, is much more randomized.

In amorphous solids, this lack of long-range periodicity often leads to very fuzzy electronic states and poor electronic performance compared to their crystalline counterparts. However, low fabrication costs makes these types of materials highly desirable for applications that do not require superior performance. Most notably, amorphous silicon has been widely used for common

photovoltaic devices[141] and thin-film transistors[142]. Amorphous In-Ga-Zn-O has shown promise for transparent thin-film transistors with reported mobilities exceeding 10 $cm^2\ V^{-1}\ s^{-1}$ [143]. Additionally, amorphous SiO_2 is widely used as a gate dielectric in the electronics industry. Tin-based oxides have been used in lithium-ion storage applications[144]. Amorphous materials have also been used as reaction catalysts, with amorphous iron being used to aid in the hydrogenation of carbon monoxide[145], and amorphous metal-oxides as an oxygen evolution reaction catalyst[146].

The majority of applications utilizing amorphous solids to date have focused on bulk materials. Knowing that ultrathin, 2D materials can exhibit varying properties from their bulk, 3D counterparts, it is important to investigate 2D amorphous materials. It would be expected that the electronic properties in dramatically thinned down amorphous semiconductors should follow similar trends to crystalline 2D materials as many of the differences from bulk to ML spawn from dielectric screening and confinement effects. These types of effects are not unique to crystalline materials.

The following sections will focus on studies involving amorphous black phosphorus. The motivation behind studying ultrathin films of aBP spurs from the promising attributes of crystalline black phosphorus. Layered black phosphorus (BP) has received an increasing amount of interest as a 2D semiconductor in recent years, especially with the ability to isolate layers down to ML[147]. Ultrathin BP films have exhibited very promising charge transport properties[147;148;148–156]. Along with novel quantum confinement effects[157;158], crystalline BP has shown a variable band gap that changes with thickness. This gap has been shown to dramatically increase from 0.35 eV in bulk to the near IR and even optical range in ML[147;159–162]. We will look at 3 different thicknesses of aBP films, 2, 5, and 10 nm. A previous study[163] performed by our collaborators, has looked at various properties of these thin films and found field effect mobilities of 14 $cm^2\ V^{-1}\ s^{-1}$ and current On/Off ratios of about 100. This gives some promise or potential applications as thin film transistors. The following will focus on the photocarrier dynamics in these materials as studied by ultrafast pump-probe experiments. This study is published in the journal, 2D Materials[164].

4.2 Carrier Dynamics in Amorphous Black Phosphorus Thin Films

4.2.1 Fabrication and Characterization of aBP thin Films

Amorphous black phosphorus ultrathin films were synthesized on silicon substrates with a 300 nm oxide layer by pulsed laser deposition (PLD). A black phosphorus crystal (Smart-Element) was used as the target. The growth temperature was set at 150 °C and the base pressure of the chamber was evacuated to around 1.5×10^{-7} Torr. Due to the instability of BP in air, a thin layer of poly(methyl methacrylate) (PMMA) was applied to protect the a-BP films. These samples were provided and characterized by Shu Ping Lau and co-workers at The Hong Kong Polytechnic University.

The structure of the as-grown films was characterized by transmission electron microscopy (TEM) and X-ray diffraction (XRD). From the energy-dispersive X-ray spectroscopy (EDX) results shown in Figure 4.2(a), the chemical composition of pure phosphorus (P) was confirmed. The minor peaks of copper (Cu) are attributed to the TEM grid. The amorphous nature of the samples was indicated by the high-resolution TEM (HRTEM) and XRD as illustrated in Figure 4.2(b) and 4.2(c) respectively. The films were further characterized by Raman spectroscopy. As shown in Figure 4.2(d), three BP characteristic peaks were observed in the Raman spectra of the aBP thin films with thicknesses of 2, 5, and 10 nm. As the thickness decreases, the peaks become broader and the intensity decreases significantly. For the 2 nm thick sample, the Raman peaks exhibit a shift of about 5 cm^{-1} with respect to the thicker films, which is consistent with the previous report[163]. This can be attributed to the consideration that for ultrathin films, the vibrational modes are more easily influenced by the highly disordered structure. Finally, the optical properties of the films were also characterized. The room temperature photoluminescence (PL) spectrum of the 2 nm aBP film is shown in Figure 4.2(e). A 808 nm laser was used as the excitation light source. The emission peak is located at 0.85 eV, which is attributed to the optical band gap of 2 nm aBP. No PL was observed from the 5 and 10 nm films, suggesting that their optical band gaps are not in this spectral range.

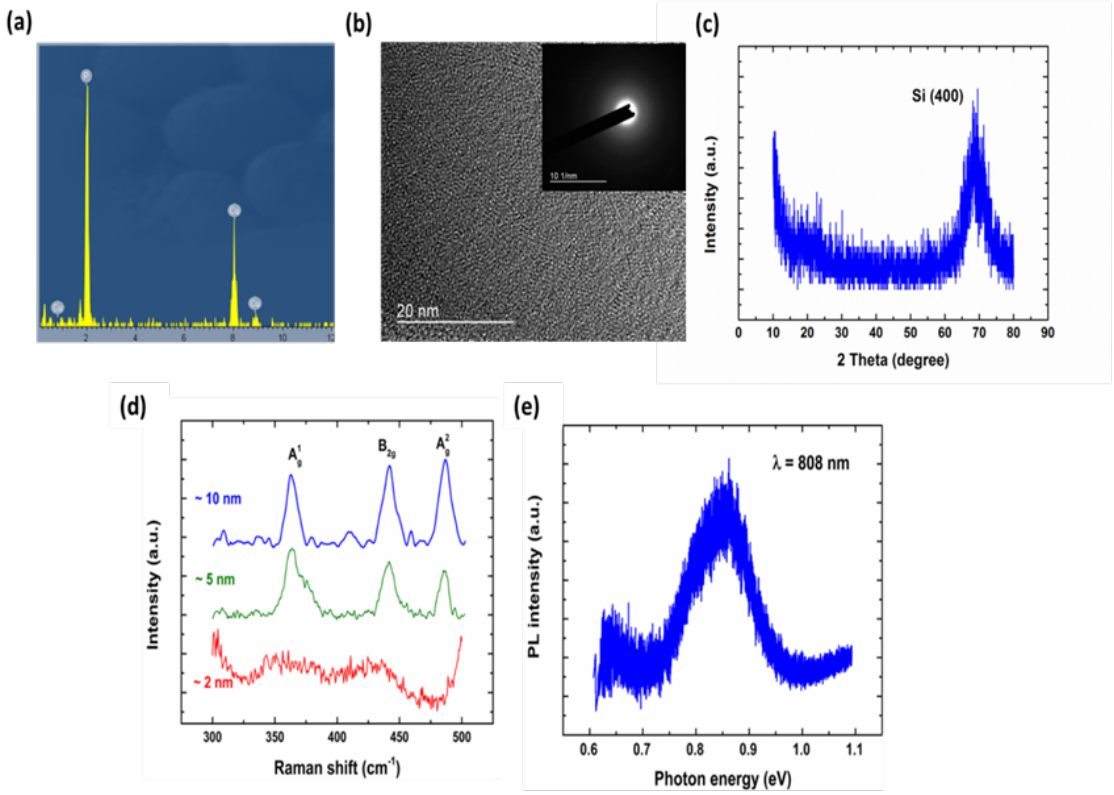

Figure 4.2: Structural characterization and optical properties of the a-BP thin films. (a) EDX spectrum of the aBP thin films, confirming that pure phosphorus films were obtained. (b) High-resolution TEM image of the 10-nm a-BP film, combining the SAED pattern shown inset, revealing the highly disordered feature of the obtained films. (c) XRD pattern of the a-BP film grown on SiO_2/Si substrate. The only emerged peak is Si (400), further confirming the amorphous nature of the BP film. (d) Raman spectra of the aBP thin films with different thicknesses. (e) PL spectrum of the 2 nm aBP film under the excitation of an 808 nm laser.

4.2.2 Results and Discussion

Transient reflection measurements were performed to investigate photocarrier dynamics in the grown aBP samples. We will first focus on the 2 nm film. Figure 4.3(a) illustrates the pump-probe scheme of the measurement. The sample was excited by a 100 fs pump pulse with a photon energy of 1.57 eV. The probe pulse with a photon energy of 0.80 eV is tuned to near the optical band gap of the sample in order to effectively sense the reflectance change of the sample induced by the pump-injected photocarriers. The differential reflection of the probe was measured as a function the delay time between the pump and probe pulses. Figures 4.3(b and c) show the observed differential reflection signal, in short and long time ranges, respectively, with various values of pump fluence. We found that the signals reach their peaks on an ultrafast time scale, and then decay exponentially.

To understand the observed features, we first establish the relation between the signal and the photocarrier density. Figure 4.3(d) shows the peak signal as a function of the pump fluence. With the fluences lower than 100 μJ cm^{-2}, the absorption of the pump can be safely assumed to be in the linear regime. Hence, the carrier density injected by the pump is proportional to the pump fluence. That is, the dependence of the signal on the pump fluence reflects its dependence on the photocarrier density. Figure 4.3(d) shows saturation effect of the differential reflection at fluences higher than 50 μJ cm^{-2}. The fluence dependence can be fit by a standard saturation model, $\Delta R/R_0 \propto F/(F+F_{sat})$, where $F_{sat} = 350$ μJ cm^{-2} is the saturation fluence. Below 50 μJ cm^{-2}, the differential reflection is approximately proportional to the pump fluence, and hence the photocarrier density.

With an excess energy of 0.72 eV, the pump pulse injected free electron-hole pairs with high kinetic energy. As shown in Figure 4.3(b), the signal reaches the peak on an ultrafast time scale, even though the probe is tuned to near the optical band gap. The rising part of the signal can be modeled by the integral of a Gaussian function with a full width of 0.45 ps, which is similar to (or slightly larger than) the cross-correlation width of the pump and probe pulses used. The initially injected non-equilibrium distributions of the electrons and holes are expected to undergo

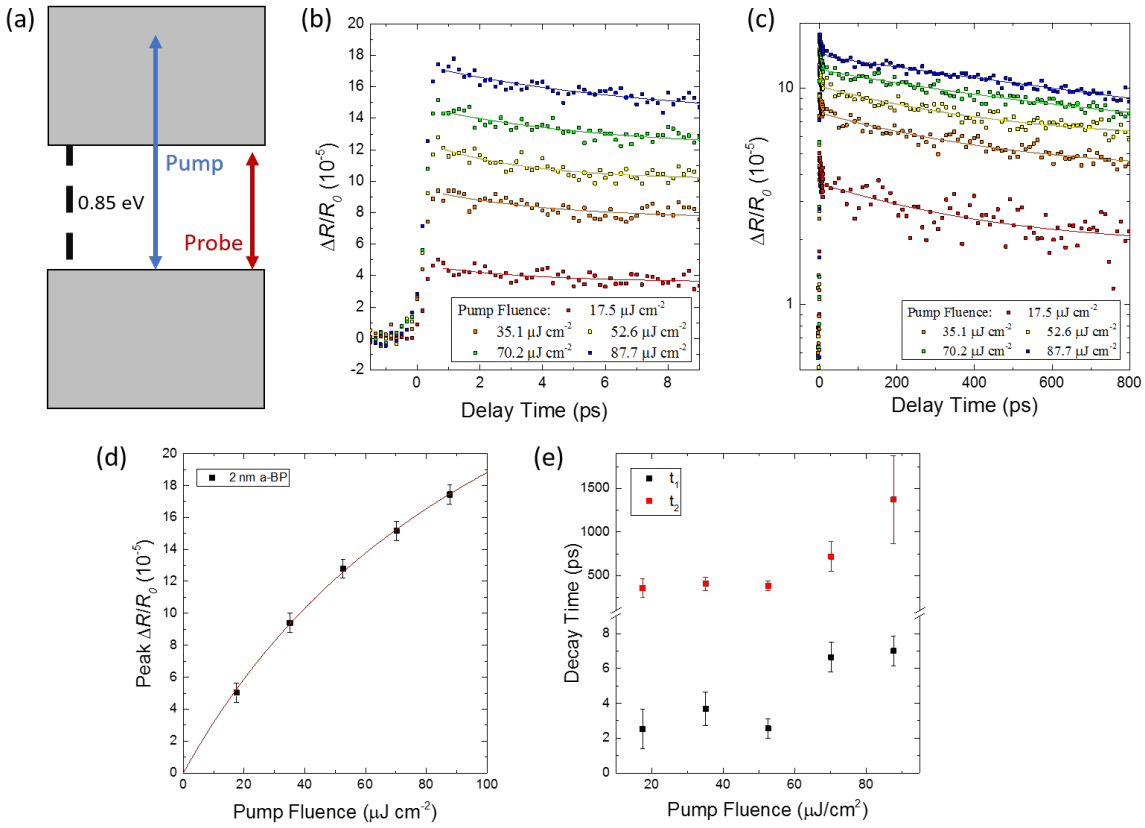

Figure 4.3: Differential reflection of then 2 nm aBP ultrathin film. (a) Schematics of pump and probe scheme with respect to the electronic bands of the 2 nm aBP film. (b) Differential reflection of the 2 nm aBP film for different values of pump fluence. (c) Same as (b), but on a larger time range and in semi-logarithm scale (d) Peak $\Delta R/R_0$ signal as a function of pump fluence. The solid line shows a fit to a standard saturation model. (e) The decay times, t_1 (black) and t_2 (red), obtained from from double exponential fits of the data in (c) as a function of pump fluence.

a thermalization process first, in which a thermal distribution is established via electron-electron and hole-hole scattering, followed by an energy relaxation process via carrier-phonon scattering, in which these hot carriers cool down to the lattice temperature of 300 K. Both processes increase the population of carriers in the probed states near the band edge, and hence are expected to cause an increase of the signal. The observed ultrafast rising time suggests that these processes occur on sub-picosecond time scales in the aBP ultrathin film. Ultrafast thermalization and energy relaxation of hot carriers have been observed in other 2D materials, such as transition metal dichalcogenides[32] and graphene[165;166], which can be attributed to the enhanced carrier-carrier and carrier-phonon interactions due to the reduced dielectric screening effect. Since such enhancement also exists in ultrathin a-BP, it is reasonable that these processes occur on a similar time scale. On the other hand, carrier thermalization and relaxation can take several tens of picoseconds in traditional bulk semiconductors and quantum wells[167].

The decay of the signal can be fit by double exponential functions, as shown by the solid curves in Figure 4.3(b) and 4.3(c). The two constants are plotted as a function of the pump fluence in Figure 4.3(e). The fast time constant of about 2 ps could be attributed to exciton formation. Due to the enhanced coulomb interaction between electrons and holes in this 2D system, the exciton binding energy is expected to be large, and excitons should be stable at room temperature. Ultrafast exciton formation from nonresonantly excited electron-hole pairs has been observed in monolayer transition metal dichalcogenides, as a fast decay of the transient reflection signal shorter than 1 ps[33;168]. After this short transient in the first few picoseconds, the rest of the decay can be described by a time constant of about 400 ± 20 ps, which is attributed to the exciton lifetime. We note that the longer time constants at high pump fluences could be attributed to the nonlinear dependence of the signal on the carrier density, as shown in Figure 4.3(d). In that regime, the time evolution of the differential reflection signal does not accurately reflect that of the carrier density.

It is interesting to note that even in the saturation regime, there is no sign of exciton-exciton annihilation. Previous studies have shown that exciton-exciton annihilation dominates dynamics of high density exciton populations in 2D TMDs[169–172]. In our measurement, the injected

exciton density is comparable to the saturation density, as evident by the sub-linear power dependence shown in Figure 4.3(d). In this regime, exciton-exciton scattering is expected to be strong. Exciton-exciton annihilation caused faster decay of exciton population at higher density, which is not observed in Figure 4.3(c). The absence of exciton-exciton annihilation suggests that the defect density of the aBP sample is rather high. This is also consistent with the relatively long exciton lifetime compared to most 2D TMDs.

To study the transport properties of excitons in aBP, we performed spatially resolved differential reflection measurements. Using the focused 1.57 eV pump pulse, we inject carriers in the aBP samples with a Gaussian profile of 2.5 μm full width at half maximum. Due to the induced density gradient, excitons diffuse two-dimensionally. We do not consider a 3D diffusion as the samples are thinner than the injection depth of the lasers and thus carriers are injected throughout the sample thickness and diffuse in a planar direction. We then measured the differential reflection as a function of both probe position and time delay, relative to the pump.

The result of this spatiotemporal measurement for the 2 nm aBP sample is shown in Figure 4.4(a). Here, the probe position is defined as the distance between the centers of the pump and probe spots. As the excitons diffuse, the spatial Gaussian profile can be seen to expand, showing a clear sign of diffusive transport. Figure 4.4(b) shows the Gaussian profiles for several probe delays. Each profile was fit with a Gaussian function to extract its full width at half maximum. The squared width, w^2, is plotted as a function of the probe delay in Figure 4.4(c). In the diffusion process with an initial Gaussian density profile, the width of the profile expands as $w^2 = w_0^2 + 11.09Dt$, where w_0 is the initial width and D, the diffusion coefficient of the excitons. With a linear fit to the squared widths in Figure 4.4(c), we find a diffusion coefficient of about 5.3 $\pm$ 0.2 cm^2 s^{-1}. By using the exciton lifetime of 400 ps, we obtain a diffusion length of $\sqrt{D\tau} = 460$ nm.

The exciton diffusion coefficient obtained is significantly larger than other amorphous semiconductors. For example, in amorphous silicon, the most widely used amorphous semiconductor, the photocarrier diffusion coefficient is on the order of 0.01 to 0.001 cm^2 s^{-1} [173–176]. Using Einstein's relation, $\mu/e = D/k_B t$, where μ, e, and k_B are the mobility, the elementary charge, and Boltzmann

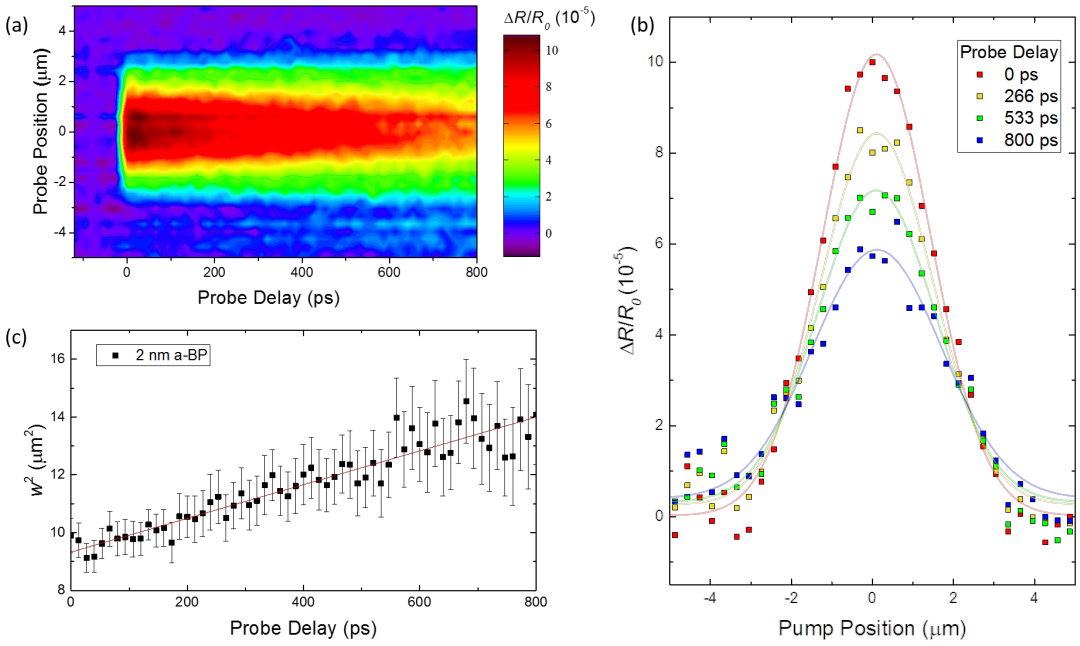

Figure 4.4: Exciton diffusion in the 2 nm aBP ultrathin film measured by spatially resolved differential reflection. (a) Spatiotemporal differential reflection signal. (b) Spatial Gaussian profiles for different delay times. (c) The squared width of the Gaussian profiles as a function of the probe delay. The data is fit with a linear function in order to extract the diffusion coefficient from the slope.

constant, respectively, we deduce an exciton mobility of 200 $\pm$ 10 cm^2 V^{-1} s^{-1}. These superior photocarrier transport properties make aBP an attractive amorphous materials for optoelectronic applications.

Similar experiments were performed on both the 5 nm and 10 nm aBP film. Figure 4.5(a) shows, again, the differential reflection of a 0.80 eV probe pulse for different relative time delays of the 1.57 eV 100 fs pump pulse as measured for the varying aBP thicknesses, 2 nm (black squares), 5 nm (red squares), 10 nm (blue squares). It can be clearly seen that the longer decay portion of the signal, which more accurately represents the exciton population in the sample is significantly larger in the 2 nm sample. This is likely due to the probe energy more closely matching the exciton resonance for this thickness of aBP. Similar to crystalline BP, we expect the band gap of aBP to significantly depend on sample thickness, likely decreasing with thickness. It is also not surprising that we observe a more prominent transient process in the first several ps in the thicker samples, as the pump energy is higher relative the gap energy.

We also performed spatially and temporally resolved differential reflection measurements on both the 5 nm and 10 nm aBP samples, in order to measure their respective diffusion coefficients. These results on the 5 nm and 10 nm samples can be seen in Figures 4.5(b) and 4.5(c), respectively. The squared FWHM, found by fitting the spatiotemporal data with Gaussian functions for the different relative delay times between the pump and probe pulses can be seen in Figure 4.5(d). The results from the 2 nm sample (black squares) is added for comparison. As before, all three datasets were linearly fit in order to extract the diffusion coefficients from the respective slopes. It can clearly be seen that the slope decreases with thickness of a-BP. Excitons were found to diffuse in the 5 nm film with a diffusion coefficient of 3.4 $\pm$ 0.4 cm^2 s^{-1}. This corresponds to an exciton mobility of about 130 cm^2 V^{-1} s^{-1}. It is interesting to note that there is no diffusion observed in the 10 nm thick sample.

In summary, charge carrier dynamics were measured in amorphous black phosphorus. Optical pump probe experiments were utilized to resolve the differential reflection of an ultrafast probe pulse in both space and time. We found the exciton lifetime to be as high as 400 ps in 2 nm thick

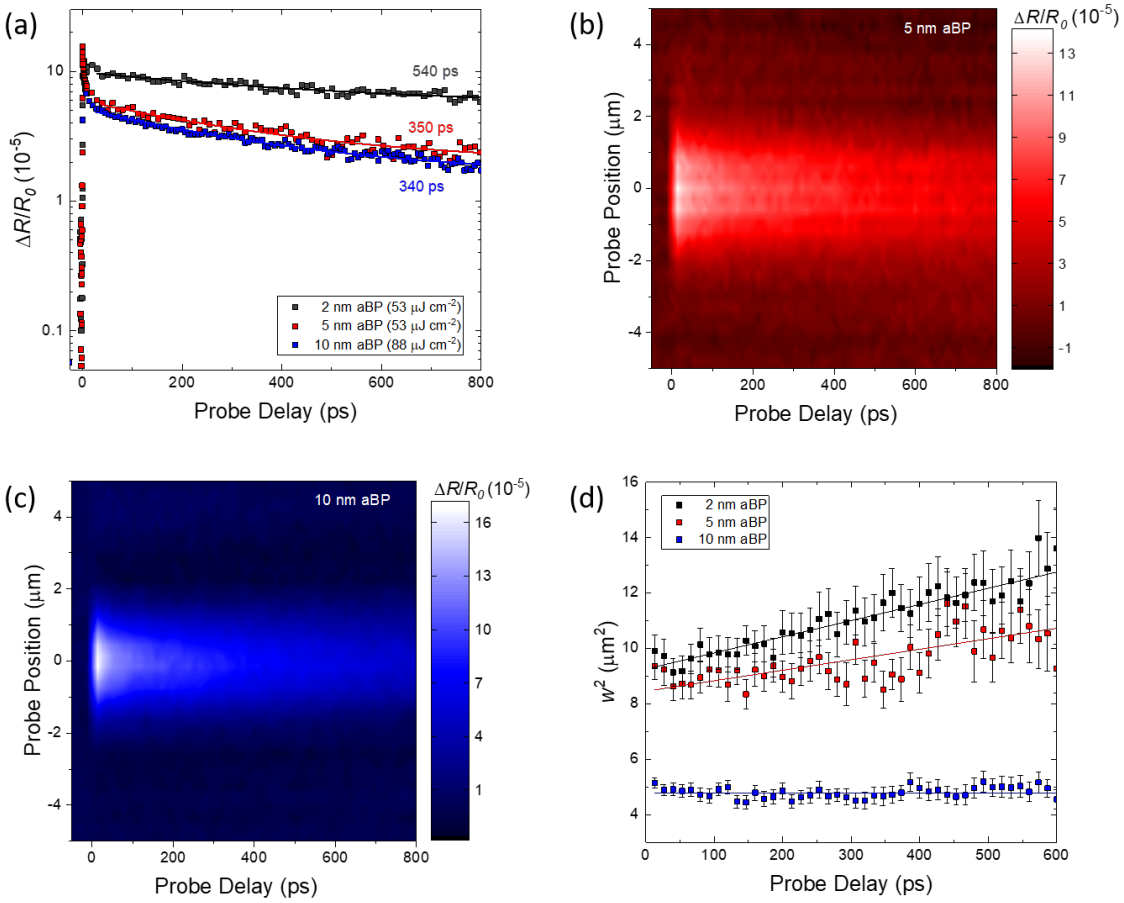

Figure 4.5: Differential reflection and exciton diffusion in the 5 and 10 nm aBP ultrathin films (a) Differential reflection of the 2, 5, and 10 nm aBP thin films plotted on a log scale vs relative probe delay. (b) Spatiotemporal differential reflection signal of the 5 nm aBP film (c) Spatiotemporal differential reflection signal of the 10 nm aBP film (d) The squared width of the Gaussian profiles as a function of the probe delay for the 2, 5, and 10 nm aBP films. Each dataset is fit with a linear function in order to extract the diffusion coefficient from the slope.

aBP samples, decreasing in thicker samples. The diffusion coefficients were also extracted and found to be in the range of 3-6 $cm^2\ s^{-1}$ for 2 nm and 5 nm thick samples. This corresponds to exciton mobilities on the order of 100-200 $cm^2\ V^{-1}\ s^{-1}$, which is about 2 orders of magnitude larger than many amorphous semiconductors currently used in a variety of applications. Amorphous black phosphorus could thus have a lot of potential for less expensive, better performing electronic and optoelectronic devices.

4.3 Carrier Transfer in 2D WS_2-aBP Vertical Heterostructure

With the promising characteristics of these amorphous samples, it is important to explore avenues for possible applications. One such direction is to use them in semiconducting heterostructures. However, it is typically difficult to find ideal growth conditions to create a quality semiconducting junction with an amorphous sample. Layered materials provide a unique solution to this problem since they adhere through vdWs forces as compared to chemical bonds. This allows for the easy formation of such heterostructures, but little is known as to the extent with which the two will interact, if at all. The following begins to explore the interaction between ultrathin aBP films with TMD MLs, specifically WS_2.

With the largest band gap of the three aBP samples studied previously, the 2 nm aBP sample provides the best platform for studying carrier dynamics in these ultrathin amorphous-crystalline heterostructures. Due to the thinness of this sample, it also fits best into the discussion of 2D semiconductor junctions.

The heterostructure samples are made by mechanically exfoliating and subsequently transferring ML flakes of WS_2 onto the aBP covered substrate. In order to create reasonable control conditions, we first transferred flakes of hBN with varying thicknesses onto regions of the aBP substrates. This is done by mechanically exfoliating flakes of hBN from bulk crystals onto PDMS substrates. The hBN flakes are then transferred onto the aBP covered substrate. Next, monolayer WS_2 samples are similarly exfoliated onto PDMS substrates and identified by optical contrast. Using the same method as with hBN, they are transferred to the aBP sample, with different regions

of the same WS_2 flake overlapping both the hBN samples and the aBP substrate. After the WS_2 is transferred, the samples are annealed for 2 hrs at 75°C in an Ar environment held at a base pressure of 3 torr. This is to help the van der Waals materials adhere better to the aBP. Next, to help preserve the aBP surface from degrading in the ambient conditions of our measurements, the samples are coating in a thin layer of PMMA.

The samples used in this study are shown in Fig. 4.6(a,b). In each, the blue outline is the ML region of the WS_2 sample, and the white outline is the hBN sample. The substrate, which is shown here as the pinkish colored background, is the aBP covered substrate. Figure 4.6(a) shows a sample using a relatively thick (>15 layers) hBN flake between WS_2 and aBP. This should create a sufficiently thick insulating barrier allowing us to study the properties of ML WS_2. The sample in Fig. 4.6(b) uses a much thinner barrier, using a few layer (<5 layers) hBN flake. Thicknesses of the hBN layers are estimated by optical contrast on PDMS.

With so little known about the electronic structure of the aBP samples, such as its work function, it is difficult to know how carriers will behave in the heterostructure. However, we attempt to estimate the expected alignment using previously calculated values for the CBM and VBM of appropriately thick crystalline black phosphorus (BP). Figure 4.7 shows the estimated band alignment and the resulting charge transfer.

With both the work function and band gap of BP being highly sensitive to thickness, we use the values from literature that best represent our 2 nm thick aBP, which correlates to about 3 layers. Relative to a 0 eV vacuum level, the calculated CBM and VBM for 3 layer BP is found to be about -4.09 eV and -4.85 eV, respectively[177]. From reports on the band alignment of various TMD MLs, the CBM and VBM of WS_2 are -3.96 eV and -5.50 eV, respectively[126]. As shown in Fig. 4.7 this results in type-I band alignment. However, with such a small conduction band offset between the materials and the ambiguity of aBP's alignment, we speculate the band alignment could be either type-I or type-II. With a large valence band offset, holes are expected to transfer from WS_2 to aBP, but the uncertainty in CBM alignment leaves us less certain of the transfer of electrons. It is important to reiterate, however, that much of this is speculation as no studies have yet to be

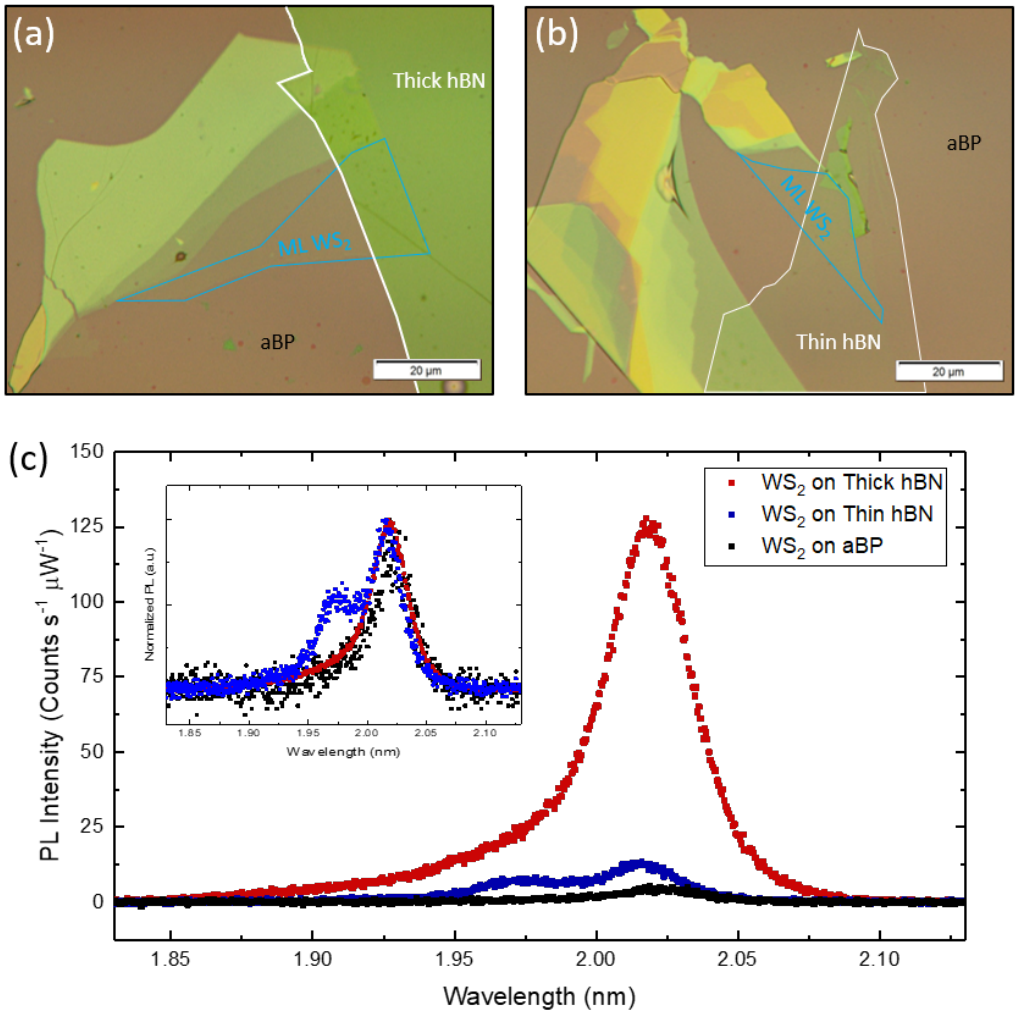

Figure 4.6: (a,b) Optical images of the samples used in this study. ML WS_2 is outlined by blue and hBN by white. (a) Optical image of the sample with bulk hBN. (b) Optical image of the sample using few layer hBN. (c) Photoluminescence spectroscopy results of ML WS_2 on bulk hBN (red), few layer hBN (blue), and directly on aBP (black). The inset shows the normalized PL.

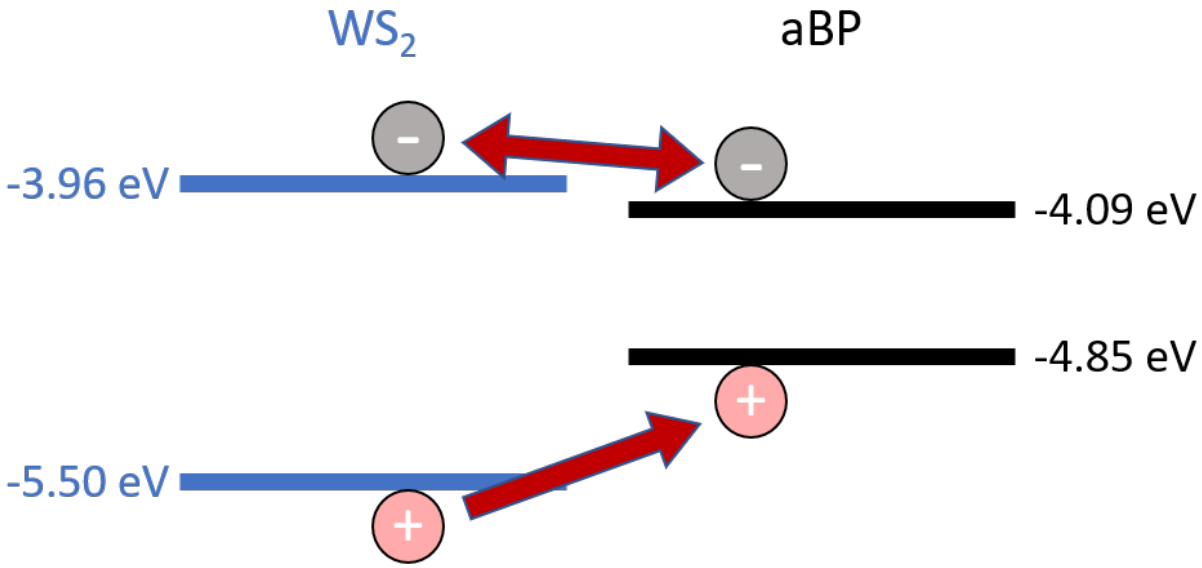

Figure 4.7: Estimated band alignment and expected charge transfer of the WS_2 and aBP heterostructure based on the calculated CBM and VBM values from literature. The fairly large valence band offset results in hole transfer from WS_2 to aBP, whereas with a small conduction band offset and relative uncertainty of the true alignment of aBP, the direction of electron transfer is less certain. From this, we would expect the band alignment to be either type-I or type-II.

performed on aBP to determine its work function or band alignment.

The WS_2 is characterized using photoluminescence spectroscopy. A continuous wave, 405 nm laser, is focused through a 100× objective lens on to the WS_2 sample. As seen in Fig. 4.6(c), the WS_2 placed on thick hBN exhibits a strong luminescent peak at 2.02 eV (red), which is consistent with previous reports and confirms the ML thickness of the WS_2 [121;122;124;125]. There is significant quenching of this peak, about 95 percent, for the portion of the WS_2 placed directly on aBP (black). This quenching is a likely indication of some sort of charge or energy transfer mechanism from WS_2 to aBP. Without the transfer of carriers, excitons would be expected to stay in WS_2 and recombine, contributing to the PL signal. It is well known that hBN serves as a near ideal substrate for many 2D materials. It is then possible that some quenching could arise as a result of simply being placed on a less ideal surface, however, it is hard to justify such a large effect on this basis alone.

Looking at the sample on thinner hBN (blue), some interesting results arise. First, despite the

thin insulating layer, there is still noticeable quenching compared to the sample on thick hBN. There is also a secondary peak present at 1.97 eV. The emission energy of this peak is consistent with that of charged excitons or trion formation, which has been previously observed in ML WS_2 [119;178]. The presence of trions would suggest that there are either excess electrons or holes in WS_2, pointing towards a charge transfer process. It is interesting to note that this only occurs in the heterostructure with a thin hBN barrier and not the direct junction, which may indicate a discernible difference in the transfer mechanisms in the two cases. As briefly discussed in the previous section, the aBP films are thought to have a fairly high density of defect states, due at least in part to the amorphous structure. Suppression of radiative recombination due to these defects could play a role in this difference.

Looking into this further, we examine the emission spectrum for different excitation powers in the sample on few layer hBN. The different spectra can be seen in Fig. 4.8. In most of these measurements there are actually 3 discernible peaks. This third peak could be attributed to bi-exciton formation, where two excitons are bound together. Each spectra is fit for 3 Lorentzian peaks, except in the 1 μW case, as no third peak was found for unknown reasons. In this case, the data was fit with a bi-Lorentzian function. The neutral, A-exciton peak of WS_2 is the blue fitted curve, with the secondary fitted peaks shown in green and red. The yellow curves show the cumulative fit from all three Lorentzian peaks.

Figure 4.9 shows the basic trends of these peaks for the different excitation powers. In Fig. 4.9(a), we see that each of these peaks experiences a slight blue shift with increasing excitation power. As discussed in 3.1.2, the difference between the emission energy of the neutral exciton and trion peaks represents the trion binding. This binding energy, as function of excitation power, is shown in Fig. 4.9(b). Extrapolating a rough linear fit back to zero power, we find a zero density binding energy of about 42.5 $\pm$ 0.9 meV. This value is consistent with previous reports [121;122]. The trend of the peak heights is shown in (c), and in each case seems to increase fairly linearly, especially in the neutral exciton case (blue). This shows that in this power range, no saturation effects are present. Finally the the FWHM of each fitted peak is shown in (d). Here, both the

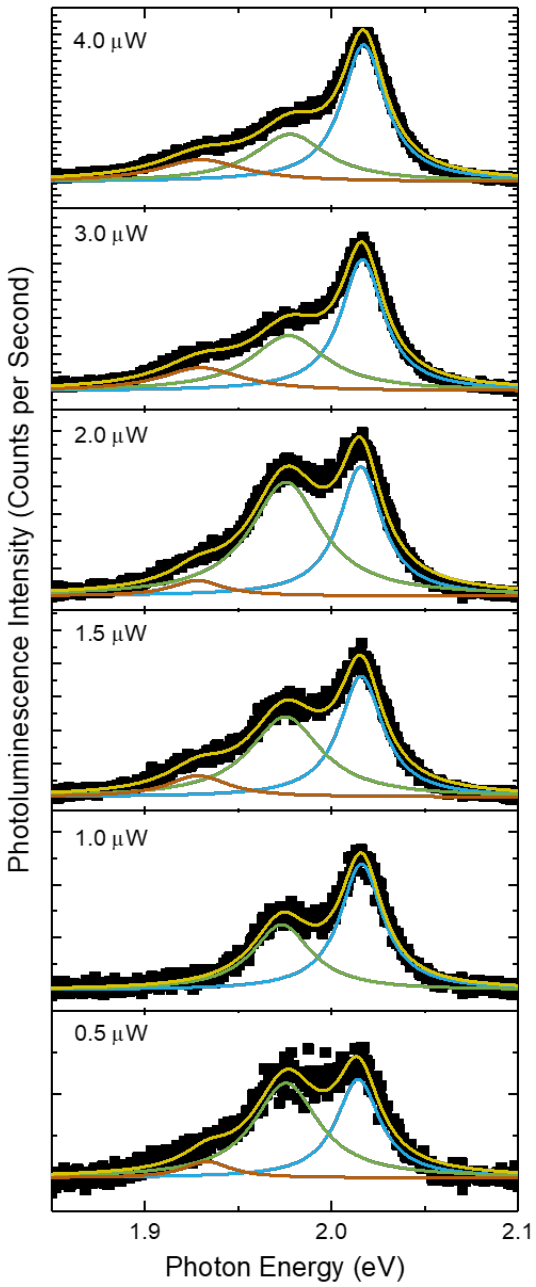

Figure 4.8: Power dependent PL spectroscopy results of ML WS_2 on few layer hBN. The colored lines are triple Lorentzian fits to the data. The blue lines are the main the A-exciton peak,the green lines are the secondary peak, and the red lines are the third peak. The yellow lines represent the cumulative fit.

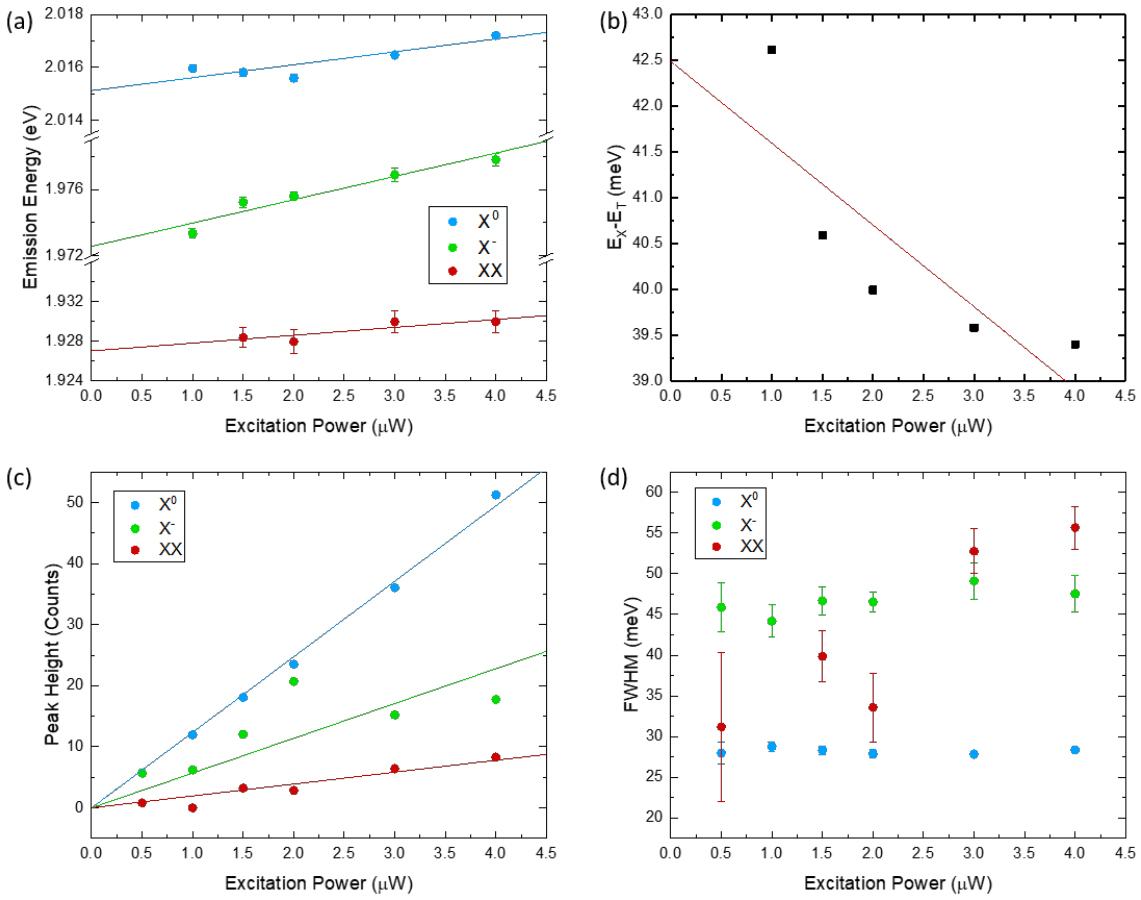

Figure 4.9: Power dependent trends from the Lorentz fits in Fig. 4.8. These are the (a) emission energy, (b) peak height, (c) FWHM, and (d) integrated PL intensity of the neutral exciton (blue), trion (green), and biexciton (red). All fit lines are linear fits to these trends.

exciton and trion peak widths appear independent of excitation power, where as the bi-exciton peak broadens with increased power.

With a clear observation of charge transfer and interaction between WS_2 and aBP, we next look at the dynamics of injected carriers in the different layers of the sample. This is done utilizing ultrafast pump-probe spectroscopy methods.

First, we look at the dynamics in the ML WS_2 layer, by probing the A-exciton resonance of WS_2 of about 2.0 eV. We inject carriers using a 3.2 eV pump with a peak fluence of 0.46 μJ cm^{-2}. With an absorption coefficient of 0.72×10^6 m^{-1}, this corresponds to an injected carrier density of 4.37×10^{10} cm^{-2}. The results measured from aBP, WS_2 on aBP, and WS_2 on bulk hBN are shown

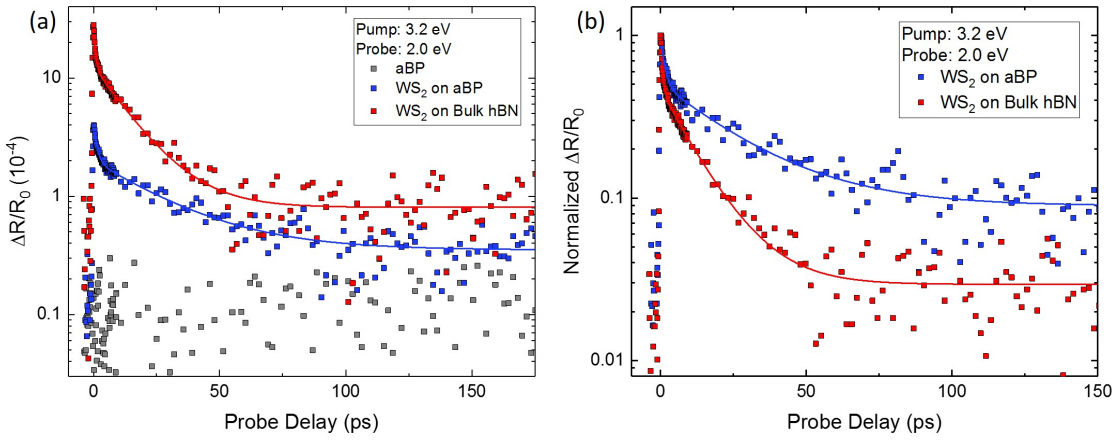

Figure 4.10: Time dependent differential reflection measurements of a 2.0 eV probe. (a) Log scale with measurements of aBP alone (grey), WS_2 on aBP (blue), and WS_2 on bulk hBN (red). (b) Same measurements as in (a) but normalized to more dramatically show the difference in decay features.

in Fig. 4.10. As can be seen in Fig. 4.10(a), these measurements yield no signal from the aBP (gray) itself. Here, we are probing about 1.2 eV above the expected A-exciton resonance of aBP, and thus expect little to no response.

Tracking the differential reflection in WS_2 on bulk hBN (blue) should provide a control for measuring the exciton lifetime in the WS_2, minimally influenced by the aBP. Comparing the data from WS_2 on bulk hBN (blue) and WS_2 directly on aBP (yellow), we see a significant quenching of the signal about 86 percent, similar to what we observed from the PL measurements. Both datasets are fit with bi-exponential functions, shown by the solid color coordinated lines in Fig.4.10(a). Fig. 4.10(b), shows the normalized data, to better visualize the difference in dynamics. The fit of the ML WS_2 control, on hBN, gives fast and slow time constants of 0.81 ± 0.07 ps and 12.5 ± 0.4 ps, respectively. WS_2, directly on aBP, gave noticeably longer decay times of 1.33 ± 0.13 ps and 26.5 $\pm$ 1.8 ps, about twice as long as on bulk hBN. Although not shown here, it is important to note that data for WS_2 on thinner hBN trended more similarly to the results of WS_2 on thicker hBN.

The longer decay of the signal for the direct heterostructure would suggest that there is charge separation at the interface. The longer decay is a result of the larger spatial separation of the

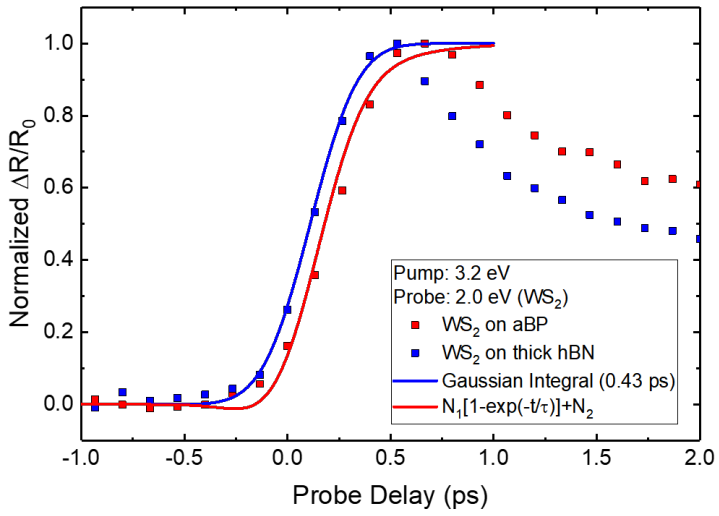

Figure 4.11: Normalized time dependent differential reflection measurements of a 2.0 eV probe on a short, few ps time scale. The blue line represents a Gaussian integral with a FWHM of 0.43 ps. The red line is a transfer model following the equation in the legend.

induced electron-hole pairs across the junction as compared to being in the same material. We also look at the dynamics on a short time scale to see if we observe any difference in the rise time of the signal. This is shown in Fig. 4.11, where the two signals are normalized to highlight the any differences. There is a noticeable, albeit small, increase in signal rise time measured from the direct heterostructure between WS_2 and aBP. We quantify this difference by first modeling the instrument response time with a Gaussian integral having a FWHM of 0.43 ps. This is shown by the blue curve, fit to the isolated WS_2 response in Fig. 4.11. The red curve is based on a transfer model, similar to eq. 3.1. The transfer time, τ_T, is found to be about 0.23 ps.

Next, we look at the dynamics of carriers in the 2 nm aBP film, using a 0.8 eV probe. First, we look at the dynamics in the aBP sample injecting carriers with an energy of 1.55 eV. This pump is focused through a 20$\times$ objective lens to spot size between 2-3 μm, injecting carriers with a peak fluence of about 53 μJ cm^{-2}. In this case, the energy is below the optical band gap of WS_2 and thus should only excite carriers in the aBP layer. We measure the differential reflection of the 0.8 eV probe in areas of both aBP alone, and the aBP-WS_2 heterostructure, as a function of probe delay. The results are shown in Fig. 4.12. The data is then fit with single exponential functions

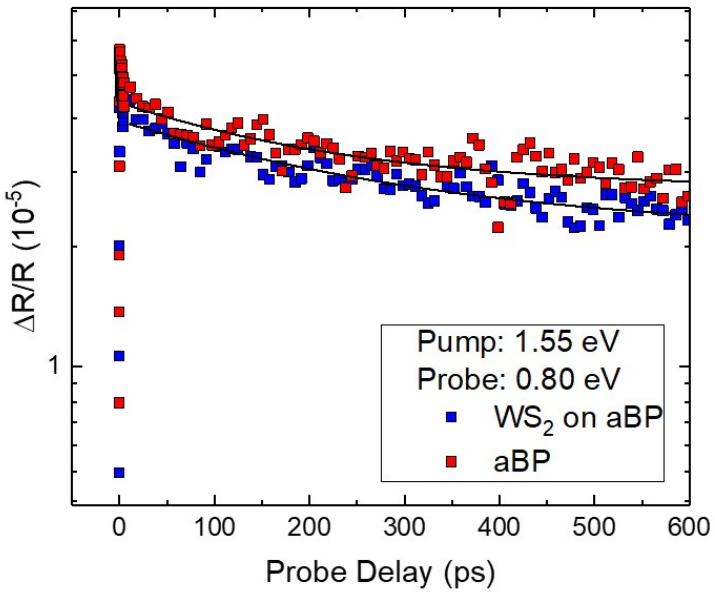

Figure 4.12: Differential reflection of a 0.8 eV probe from aBP (red) and WS_2 on aBP (blue), injecting carriers only in aBP with a 1.55 eV pump.

to extract the exciton lifetime in each part of the sample. We find a time constant of 220±45 ps measured from the aBP sample and 290±47 ps in the heterostructure. The slightly longer lifetime in the heterostructure provides further evidence of charge separation in the crystalline-amorphous vdW heterostructure.

Overall, there is substantial evidence of charge transfer between ultrathin aBP films and monolayer WS_2. The strong quenching of both the PL and the differential reflection signal from WS_2 both provide an initial indication of this. The presence of exotic peaks in the PL spectrum in the sample on thin hBN, representing the formation of trions and possibly biexcitons, suggests that there is charge separation in the heterostructure, as well as, evidence of coupling between the materials strong enough to illicit tunneling through an insulating barrier, albeit a thin one. A noticeably longer exciton lifetimes measured from the heterostructure region compared to the isolated individual materials additionally supports the observation of charge separation at the junction. These findings hold much promise for future applications involving amorphous semiconductors and 2D materials alike. The result of charge transfer and thus electronic interaction between amorphous

and crystalline 2D layers can open up new avenues for device functionality. Combining the inexpensive and easy application of amorphous materials and the superior performance of crystalline layered materials like the TMDs could prove promising for future applications in photovoltaics, thin film transistors, and beyond.

Chapter 5

Exciton Dynamics in 2D Lateral Heterostructures

5.1 Introduction to 2D Lateral Heterostructures

In the previous sections, we highlighted several examples of vertically stacked heterostructures. The ability to use van der Waals interaction to weakly adhere two individual layers, virtually ignoring lattice parameters, is a significant advantage that 2D materials possess. However, it is also very intriguing to explore the opportunities of in-plane, lateral heterostructures in the 2D realm.

Lateral modulation of electronic and optical properties of 2D materials is necessary for planar devices with high-density integration potentials, such as atomically thin p-n diodes, light-emitting devices, and photovoltaic devices. Since 2014, several groups have reported on the fabrication of lateral heterostructures made from ML TMDs, such as chalcogen-changing MoS_2-$MoSe_2$ [179] and WS_2-WSe_2 [179;180], and metal-changing MoS_2-WS_2 [180–184] and $MoSe_2$-WSe_2 [185]. These TMD lateral heterostructures have atomically sharp, high-quality interfaces and coherent lattice matching between the two materials. Furthermore, using two-step epitaxy growth, it is possible to fabricate heterostructures with both chalcogen and metal atoms changing, such as WSe_2-MoS_2, where alloy formation in the junction region can be avoided, and the shape of the junction can be precisely controlled [186]. There has also been patterned growth of lateral heterostructures utilizing lithography [187] or focused ion beam etching [188;189], illustrating the potential of device integration.

The successful fabrication of lateral heterostructures has enabled the study of electron transport across semiconducting junctions at the atomic limit, a core issue for applications in electronics and optoelectronics. Many of the TMD lateral heterostructures have been found to form type-II band alignment, which will facilitate the separation of electrons and holes at the junction [190–192].

When the two materials forming a heterostructure have different types of charge carriers, effective p-n junctions can form, as confirmed by observations of current rectification and photovoltaic effects[179;181;183;186;193]. Others have found certain lateral TMD-TMD structures can exhibit type-I band alignment[187], allowing for full spectrum of charge and energy transfer mechanisms.

Although these pioneer studies have revealed the effectiveness of electron transport in these materials, quantitative information on the mechanisms of this process is rare. The following study explores the drift transport of optically injected carriers near the planar junction between MoS_2 and $MoSe_2$. Spatially and temporally resolved pump-probe experiments are utilized to track the spatial profile of the injected photocarrier density, providing a more quantitative approach for studying the lateral transport of charge carriers in 2D materials.

5.2 Photocarrier Drift Across Type-I MoS_2-$MoSe_2$ Lateral Heterostructure

The samples for this project were provided by Dr. Kai Xiao and team at Oak Ridge National Laboratory. These lateral heterostructures are formed using a pulsed laser vaporization method outlined in more detail in Ref. [187]. First, $MoSe_2$ MLs are grown by a pulsed laser deposition assisted vapor transport technique. Using electron beam lithography, different sized strips are patterned for SiO_2 deposition. For this project, these strips varied in width from 0.5 μm to 7 μm. A sulfurization process is then used to convert exposed areas, not covered by SiO_2, from $MoSe_2$ to MoS_2. The physical junction size at the interface is found to be about 5 nm wide[187].

An ideal representation of the samples crystal structure is shown in Fig. 5.1(a). The gray atoms are molybdenum, with the red and blue atoms representing sulfur and selenide, respectively. Figure 5.1(b) shows an optical image of one of the samples used in this study, which has alternating MoS_2 and $MoSe_2$ strips, 7 μm wide. The blueish color regions are $MoSe_2$ covered with about 50 nm thick SiO_2, leaving the uncovered areas to be MoS_2 after the sulfurization process. The wide strips provide isolated areas of each material for a direct comparison of properties, as well as the ability to look at the behavior of a single junction. We later study samples with 500 nm strips which provides further insight into more aspects of the carrier dynamics in these heterostructures and a

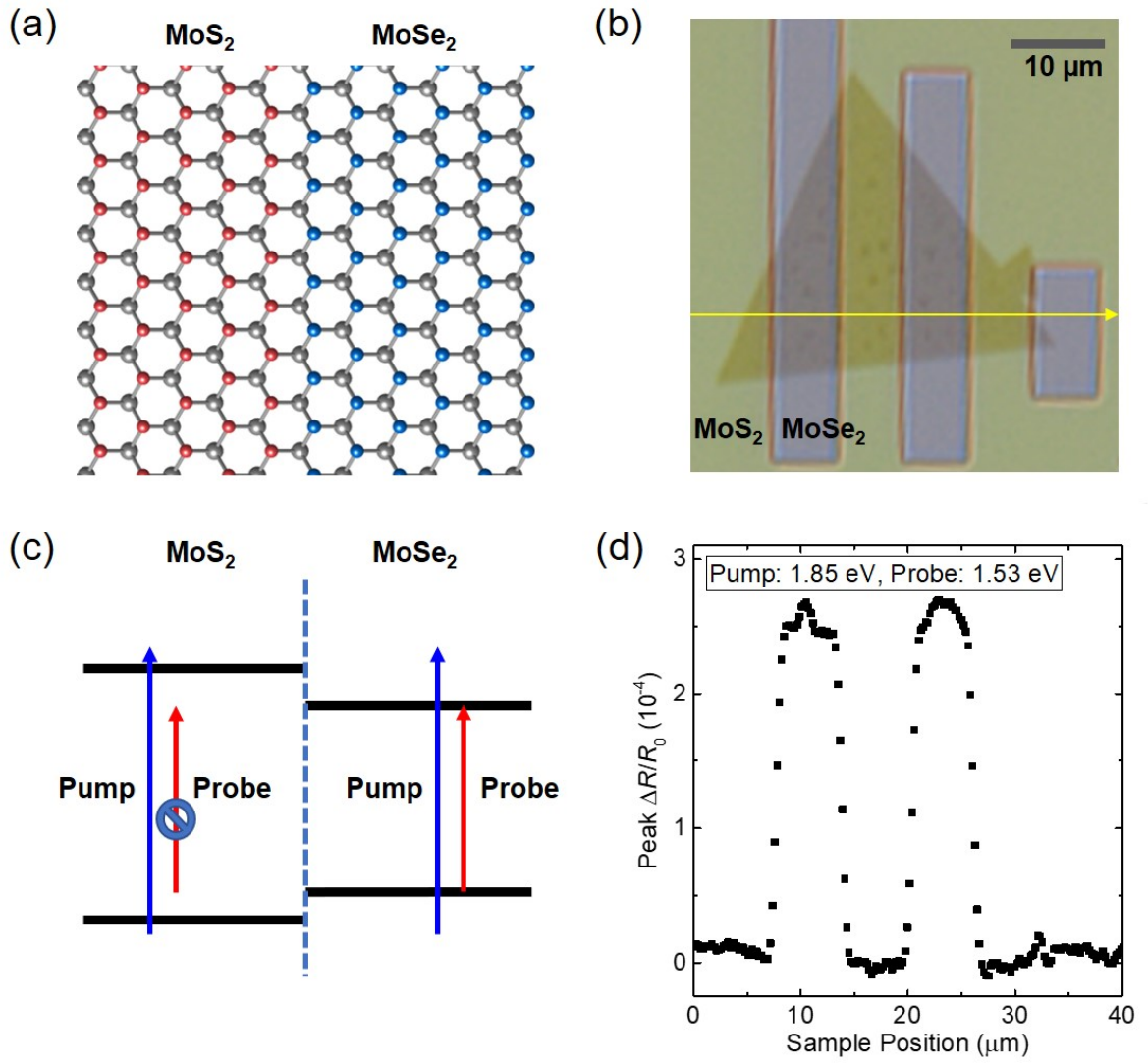

Figure 5.1: (a) Schematic of the crystal structure for an ideal MoS_2-$MoSe_2$ heterostructure. (b) Optical image of the sample with alternating 7 μm strips of MoS_2 and $MoSe_2$. Tge bluish colored region is the $MoSe_2$ covered by a SiO_2 film. (c) Schematic of the band alignment of the sample and the pump-probe experiment. The blue and red arrows represent the pump and probe energies, respectively. A probe resonant with the gap energy in $MoSe_2$ will not be sensitive to carriers in MoS_2 (d) Peak differential reflection scanned across the 7 μm sample shown in (b). The yellow arrow in (b) shows the path of the scan.

chance to observe more general junction behavior.

5.2.1 Exciton Dynamics in $MoSe_2$ and MoS_2

To study the photocarrier dynamics in these samples we utilize transient absorption measurements. Pump and probe laser pulses, of about 100 fs in duration, are focused onto the sample, through a 20x objective lens, to a size of about 1.5 μm in FWHM. As defined in previous chapters, we measure the differential reflection of the probe.

For much of the experiment, we use a 1.53 eV probe, which closely matches the A-exciton resonance of ML $MoSe_2$ [187]. Figure 5.1(c) shows the expected band alignment and justification for using this probe. With the smaller of the two band gaps, probing $MoSe_2$ allows us to selectively probe carriers only in this material. This will be more important later, when trying to resolve transport mechanisms near the junction.

To confirm this, we first measure the differential reflection at zero delay (peak signal), and scan across the sample. The results are shown in Fig. 5.1(d), with the yellow arrow in Fig. 5.1(b) showing the scan path. Here, a 1.85 eV pump, with a spot size of 1.5 μm in FWHM, is used with a peak fluence of about 20 μJ cm^{-2}. With estimated absorption coefficients of 2×10^5 cm^{-1} in $MoSe_2$ and 3.5×10^5 cm^{-1} in MoS_2 [42], we expect this to correspond to injected carrier densities of 10^{12} cm^{-2} and 1.8×10^{12} cm^{-2}, respectively. Despite injecting carriers in both materials, it is clear from the results in Fig. 5.1(d) that the probe in this case is only sensitive to the $MoSe_2$ portion of the sample. It is also important to note that a portion of the deposited SiO_2 that is not covering $MoSe_2$, is measured in this scan, and expectedly produces no $\Delta R/R_0$ signal. This confirms that the signal we see from $MoSe_2$ is indeed from $MoSe_2$ and not from the protective SiO_2 layer.

Next, we measure the differential reflection as a function of the relative time delay, gaining insight into the dynamics of photocarriers in the two ML regions. Figure 5.2 shows the decay profiles for different regions of the sample. The blue and gray symbols represent the differential reflection of the same 1.53 eV probe, used previously, as measured from the $MoSe_2$ and MoS_2 regions, respectively. In $MoSe_2$, the decay of the signal was fit by a bi-exponential function,

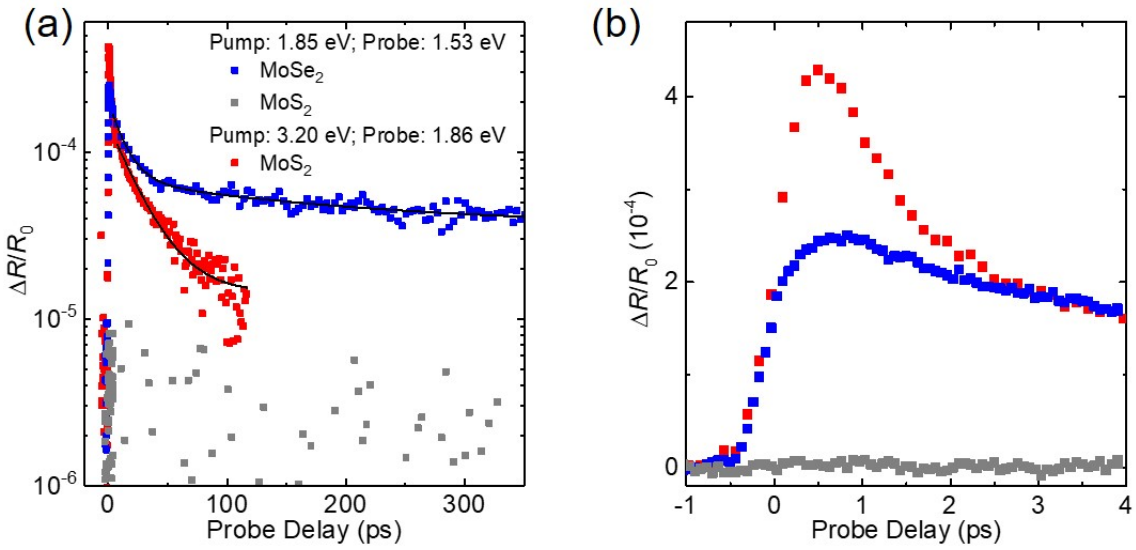

Figure 5.2: (a) Time resolved differential reflection signal measured in different regions of the sample. The blue and gray squares represent the signal from a 1.53 eV probe, resonant with $MoSe_2$, measured from $MoSe_2$ and MoS_2, respectively. The black lines represent bi-exponential fits to the data. (b) The same measurements as in (a), but on a shorter (few ps) time scale.

$\Delta R/R_0 = A_1 \times exp(-t/\tau_1) + A_2 \times exp(-t/\tau_2) + A_0$, as shown by the black curve over the data. The two decay constants are found to be $\tau_1 = 13 \pm 1$ ps and $\tau_2 = 190 \pm 50$ ps, respectively, with $A_1 : A_2 \approx 4 : 1$. We attribute the long time constant to the exciton lifetime in $MoSe_2$. The short time constant could originate from effects of exciton-exciton annihilation[169;170] or hot excitons. As expected, there is no signal detected from the MoS_2 region (gray symbols), which is attributed to the probe energy being below the exciton resonance of MoS_2.

Considering that the MoS_2 was fabricated by the sulfurization of $MoSe_2$, it is necessary to probe the photocarrier dynamics in MoS_2. For this purpose, we measured the differential reflection of a 1.86 eV probe, which is tuned near the A-exciton resonance of MoS_2, with a 3.20 eV pump. The results of this configuration as measured from the MoS_2 region are shown in Fig. 5.2 as the red symbols. Here, we find an initial fast decay of about 1 ps, highlighted in Fig. 5.2(b), which represents a short transient process as free-carriers form excitons[33;34]. After this short process, we can fit the decay of the signal with a single exponential function, $\Delta R/R_0 = A_* exp(-t/\tau) + A_0$,

where τ again represents the exciton lifetime. The fit is shown by the respective black curve in Fig. 5.2(a) and is has a time constant of 24 $\pm$ 2 ps. This exciton lifetime is comparable to exfoliated MoS_2 MLs[112;132], confirming the high quality of MoS_2 fabricated by this method.

5.2.2 Observation of Type-I Band Alignment

The previous section established the dynamics in the two materials in isolated regions of each. To gain a better understanding of the dynamics near the junction we change our focus to a sample with 0.5 μm alternating strips. It is not sufficient to look at the decay profile at a single junction. This is because the physical junction size (~5 nm)[187] is far too small to contribute to the signal, since the probe spot size is larger than a micrometer. Having thinner strips of the two materials allows for a greater contribution, from multiple junctions, to the overall signal.

Figure 5.3(a) shows an optical image of the sample used for this purpose. As before, the blueish strips are the SiO_2 covered $MoSe_2$ regions, with the uncovered regions being MoS_2. Again, the sample is excited using a 1.85 eV pump and the differential reflection of a 1.53 eV probe is measure as a function of relative delay time. The results are shown in Fig. 5.3(b) for the 0.5 μm strips (orange). For comparison, the results from the isolated $MoSe_2$ sample are re-plotted from Fig. 5.2 (blue). The magnitude of the signal from the heterostructure sample is significantly less than that from $MoSe_2$ alone. This is largely attributed to the probe partially overlapping regions of MoS_2, to which it is not sensitive. Additionally, some sample to sample variation could contribute to the decreased magnitude of the probe reflection. In fitting this data with a bi-exponential function, we find short and long time constants of 14 $\pm$ 9 ps and 67 $\pm$ 20 ps, with comparable contributions. The lack of a slow component would suggest that both electrons and holes transfer, as expected from type-I alignment. If type-II, the charge separation at the junction would be expected to create a longer exciton lifetime, similar to observations in TMD vertical heterostructures[35;78;79;102;194].

The early part of the dynamics are shown in Fig. 5.3(c). Here, the two signals are normalized to facilitate a better comparison between the signal rise time in each case. There is a noticeably longer rise of the signal in the heterostructure case compared to the isolated $MoSe_2$ ML. The gray

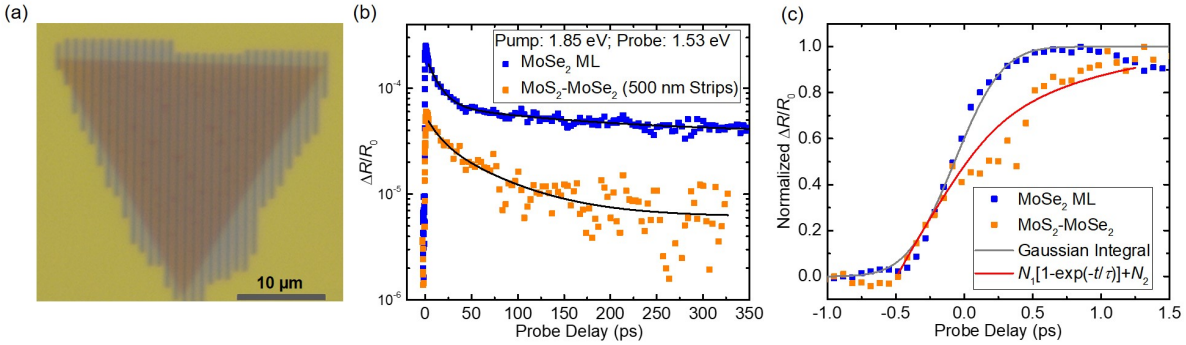

Figure 5.3: (a) Optical image of the sample with 0.5 μm alternating strips of MoS_2 and $MoSe_2$. (b) Time resolved differential reflection of a 1.53 eV probe for isolated $MoSe_2$ (blue) and the 500 nm strips (orange). The black curves represent exponential fits to the data. (c) Short time scale measurements of the same regions in (b). The gray line represents a Gaussian integral fit to the rise time of the isolated $MoSe_2$ data and the red line is a transfer model for the rise time of the signal from the heterostructure.

line, fit to the $MoSe_2$ ML data, is calculated using a Gaussian integral with a width of 0.275 ps. This value is close to the cross-correlation width of the pump and probe pulses, and thus represents the time resolution of the experiment. The red line, fit to the heterostructure data, is represented by $N_1[1-exp(-t/\tau_T)]+N_2$, where N_1 and N_2 represent the initial exciton densities in MoS_2 and $MoSe_2$, respectively. Here, τ_T represents the transfer time for the signal to reach its peak and is found to be about 0.8 ps. This increased rise time is strong evidence of exciton transfer from MoS_2 to $MoSe_2$ and type-I band alignment.

5.2.3 Observation of Exciton Drift

With strong evidence that carriers are indeed transferring from MoS_2 to $MoSe_2$, we next want to observe more about the dynamics of this carrier transfer. This is done by tracking the differential reflection of a 1.53 eV probe over time, as well as, a function of the relative spatial separation between the pump and probe pulses. A schematic of this spatiotemporal measurement scheme is shown in Fig. 5.4. To keep the relative pump-probe separation consistent with the sample position, the probe is kept stationary near the junction while the position of the pump is swept across the sample.

Figure 5.4(a) shows the expected band alignment and exciton transfer at the junction. The blue and red arrows represent the pump and probe energies, respectively. Carriers are injected in both layers, but the band offsets at the junction create a built-in electrical potential facilitating the transfer of both types of charge. As shown earlier, the probe is only sensitive to the carriers near the band edge in $MoSe_2$. Figure 5.4(b) shows a schematic of the initial carrier distribution near the junction (zero delay). The yellow and red circles represent excitons injected in MoS_2 and $MoSe_2$, respectively. At later probe delays, the excitons in MoS_2 transfer to $MoSe_2$ and take on the properties of $MoSe_2$ excitons, as shown in Fig. 5.4(c). It is also important to note that band alignment additionally prevents either charge carrier to transfer in the opposite direction (into MoS_2). Thus, the expectation would be for a build-up of carriers near the junction.

For this experiment a more energetic 2.21 eV pump is focused through a 100× objective lens, to a spot size of 0.65 μm, injecting carriers with a peak fluence of 78.3 μJ cm^{-2}. With absorption coefficients of 3×10^5 cm^{-1} and 2.6×10^5 cm^{-1} [42], this corresponds to injected carrier densities of 4.6×10^{12} cm^{-2} and 4.0×10^{12} cm^{-2} in MoS_2 and $MoSe_2$, respectively. In this experiment, the probe with a FWHM spot size of about 0.9 μm, is positioned about 0.5 μm onto the $MoSe_2$ side of a single junction of the 7 μm sample. This is done to help increase the signal to noise ratio, but still see effects from carriers injected in MoS_2. The results of these spatiotemporal measurements are shown in Fig. 5.5. The signal shows a clear trend towards the MoS_2 side of the junction with increased delay time, which is consistent with the expectations discussed early and strong evidence for carriers moving from MoS_2 to $MoSe_2$. Fig. 5.5(b) shows the measured spatial profiles at each time step. A plot of the normalized spatial profiles is shown in Fig. 5.5(c) in order to provide a better visual of the shift at later delay times.

Each profile is fit with an asymmetric double sigmoidal function in order to extract the center position of the profile. The fitting function is given by,

$$y = y_0 + A \cdot \frac{1}{1 + e^{-\frac{x - x_c + \frac{w_1}{2}}{w_2}}} \cdot \left(1 - \frac{1}{1 + e^{-\frac{x - x_c - \frac{w_1}{2}}{w_3}}} \right) \tag{5.1}$$

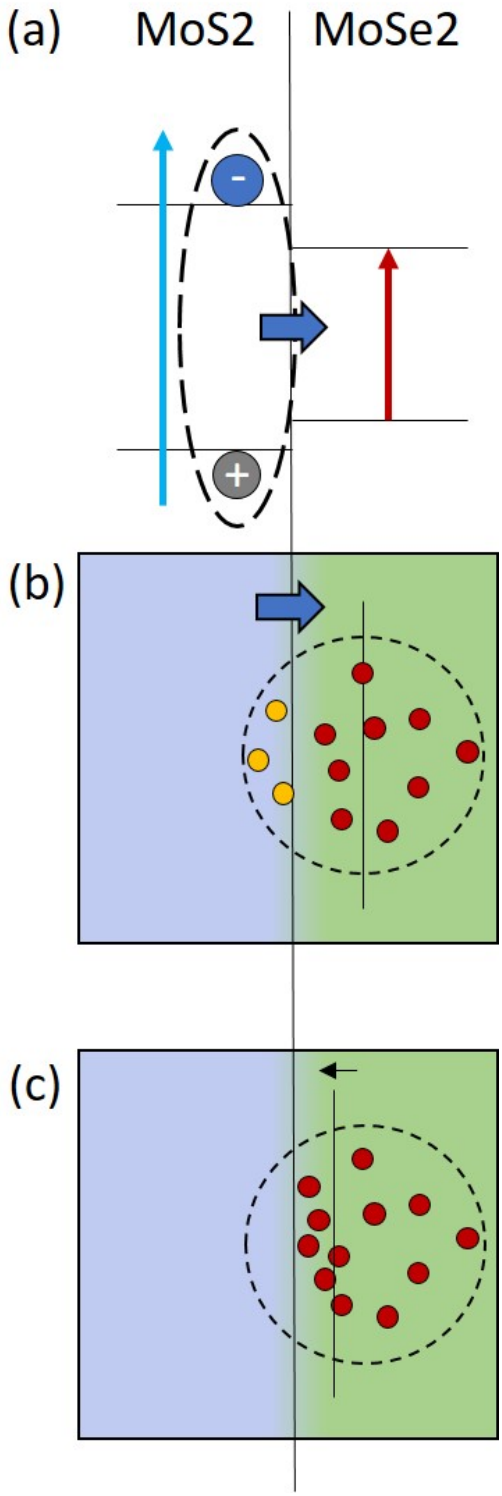

Figure 5.4: (a) Schematic of the expected band alignment and exciton transport. The blue and red arrows represent the energy of the pump and probe, respectively. (b) Schematic of the differential reflection scheme near the junction at the time of carrier injection. The yellow and red circles are excitons injected in MoS_2 and $MoSe_2$, respectively. The black line represents the measured center of the distribution (c) Schematic of the experiment at a later time, after carrier injection. The measured center of the profile (black line) shifts towards the junction as excitons transfer from MoS_2.

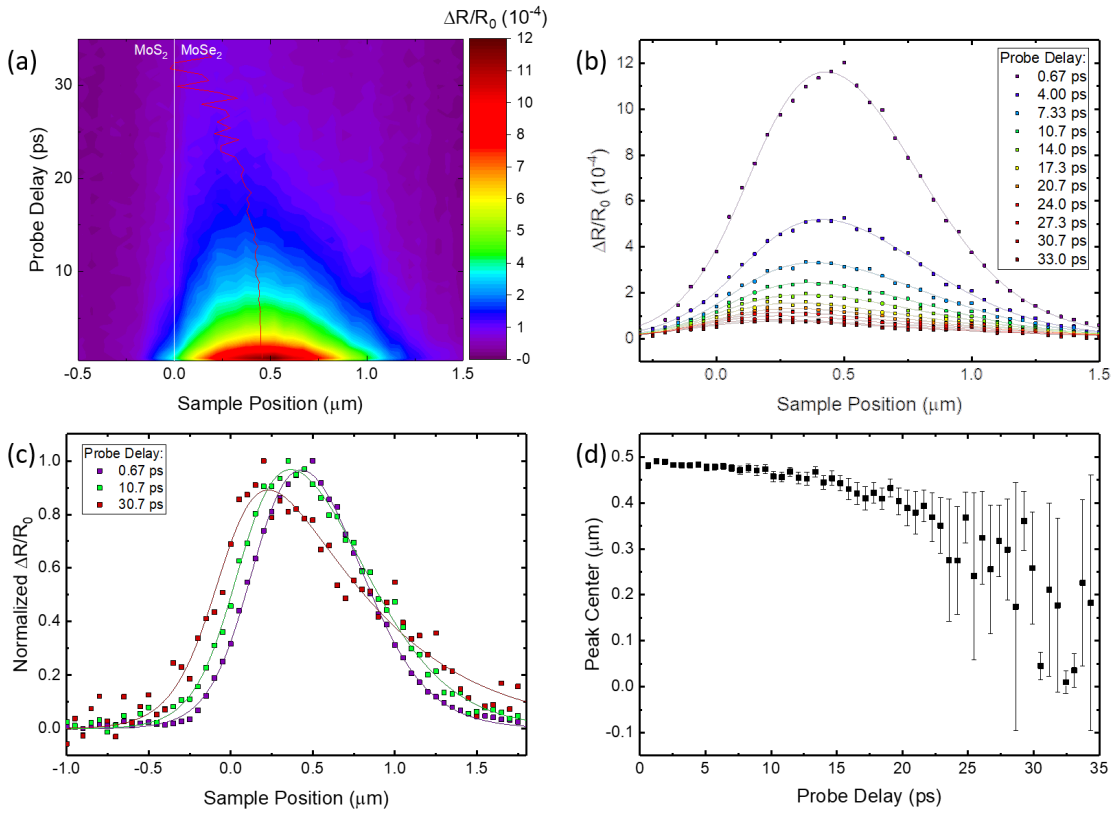

Figure 5.5: (a) Spatiotemporal differential reflection measurements measured across a single MoS_2-$MoSe_2$ junction. The red line shows the peak signal in time. The vertical white line, at $x = 0$, represents the junction between materials. (b) Spatial profiles of the differential reflection measurements for different delay times with the colors going from violet to red representing early to late delay times. The color coordinated lines are asymmetric double sigmoidal fits to the data. (c) A sampling of normalized spatial profiles with the same fits from (b) providing a better visual of the shifting profile. (d) The position of the peak center of each fit as a function of delay time.

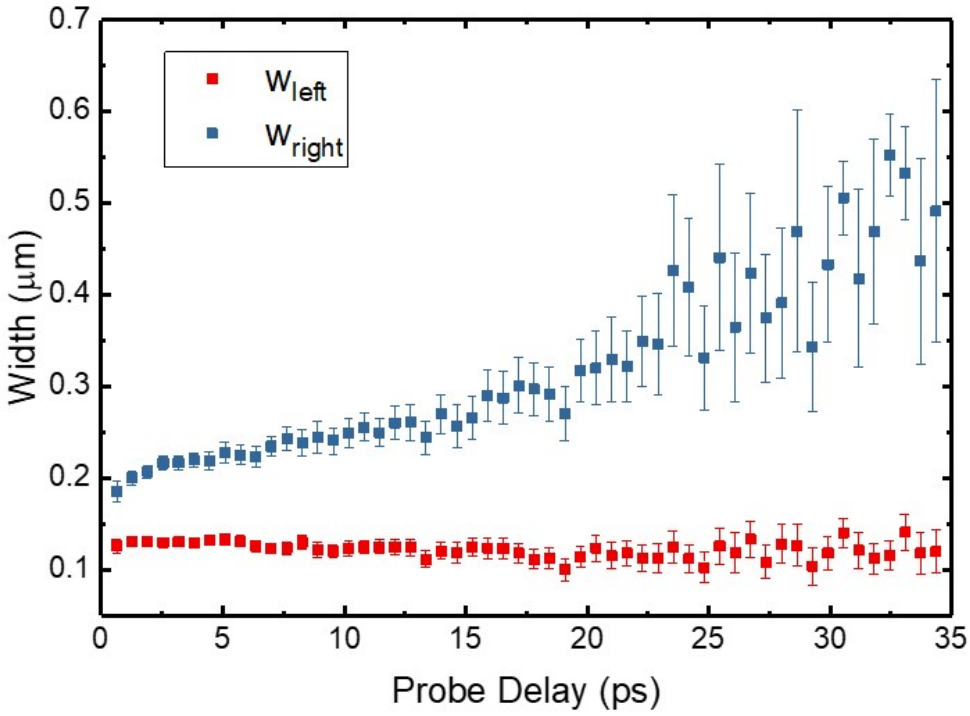

Figure 5.6: Width of the left (red) and right (blue) contributions to the asymmetric double sigmoidal fits to the spatial profiles.

where x_c is the center of the profile, w_1 is the full width at half maximum of the profile, and w_2 and w_3 are the variance or width of the left and right sides, respectively.

Ultimately, the fairly large shift of x_c towards the junction with increasing delay time, as shown in Fig. 5.5(d), as well as by the red overlay in (a), provides strong evidence of carrier transport from MoS_2 to $MoSe_2$. Further evidence of this is shown in Fig. 5.6, where the width of each side of this double sigmoidal fit is tracked as function of delay time. It is clearly seen that the left side, trending further into $MoSe_2$, expands, whereas the right side, trending towards the junction remains fairly constant. With the position of the highest carrier density trending towards the junction, but the profile width only expanding away from the junction, this is a clear indication of carrier build-up near the junction.

Finally, to additionally confirm that this observation is not a result of unforeseen impacts of the experimental process and that the result is from carrier transport across the junction, we perform

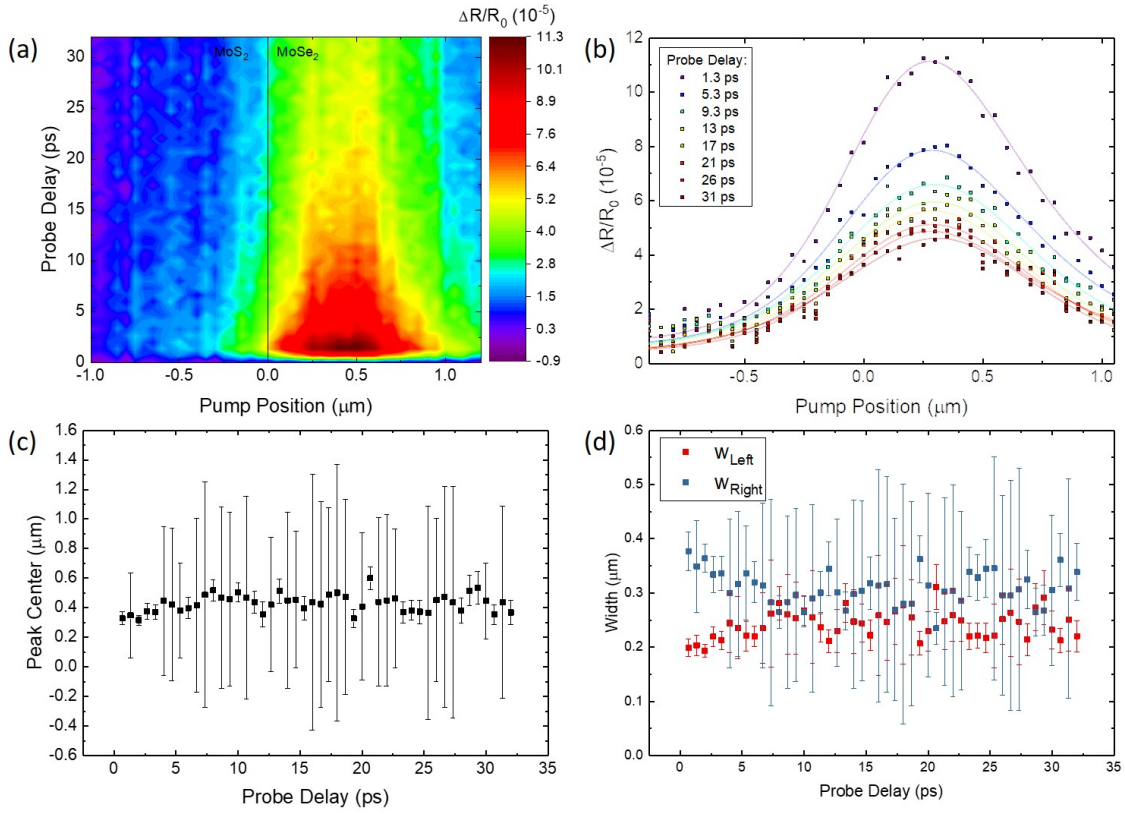

Figure 5.7: (a) Spatiotemporal differential reflection of a 1.53 eV probe for a pump energy of 1.72 eV. (b) The spatial profiles at a sample of delay time. The fits in this case are Gaussian fits. (c) Plot of the Gaussian center of each spatial profile fit as a function of the delay time.

the experiment again with a 1.72 eV pump. This pump energy is below the band gap of MoS_2, and thus selectively injects carriers in $MoSe_2$. The results of this experiment are shown in Fig. 5.7. Here, each spatial profile, Fig. 5.7(b), is fit with a Gaussian function to extract the center position. This center position is tracked as a function of delay time, as shown in Fig. 5.7(c). With no carriers injected in MoS_2, the position of the distribution remains relatively constant. This would indicate that the previously observed shift of the distribution is certainly from the transfer of carriers from MoS_2 to $MoSe_2$.

5.2.4 Model of Carrier Dynamics

With clear evidence of exciton transfer across the junction, we next attempt to quantify this result. Had this study involved a uniform sample under the influence of an external electric field, it would be relatively simple to quantify a drift velocity. One could simply track the position of the distribution over time. However, in our case, the movement of the measured distribution is opposite of the expected transfer direction, because we are selectively probing carriers on one side. Thus, we modeled the experiment in order to extract the evolution of the injected carrier profile.

In the spatiotemporal measurements, the spatial profile measured at each time step is considered to be a spatial convolution of the injected carrier density and the sensitivity profile of the probe. In general terms, the convolution of any two functions, A and B, is given by:

$$C(x) = \int_{-\infty}^{\infty} A(x)B(x-\mu)d\mu \tag{5.2}$$

where μ is the spatially shifted position of B. In this simulation, the probe profile, $P(x)$, is taken as the measured Gaussian profile of the probe laser spot multiplied by a Heaviside function centered at the MoS_2-$MoSe_2$ junction, taken as $x = 0$,

$$P(x) = \frac{1}{\sigma\sqrt{2\pi}} e^{\frac{-(x-x_o)}{2\sigma^2}} \Theta(x) \tag{5.3}$$

$$\Theta(x) = \begin{cases} 0 & x < 0 \\ 1 & x \geq 0 \end{cases} \tag{5.4}$$

Here, σ is the full width half maximum (FWHM) of the Gaussian and x_o is the center of the profile relative to the junction. This way the sensitivity of the probe only considers the contribution from carriers present in $MoSe_2$. This profile is shown in Fig. 5.8 (red) for $\sigma = 0.9$ μm and $x_o = 0.5$ μm.

A similar treatment is used for building the injected carrier density. First, it is important to recognize that the pump laser injects carriers differently in the two materials. This means we cannot simply treat the initial injected carrier density as the pump laser spot, but rather as two halves of the

measured pump Gaussian profile with different amplitudes. Their respective amplitudes are based on the absorption coefficients of the two materials for the pump energy used in the experiment, 2.21 eV. We also correct for the loss of transmission into the $MoSe_2$ layer due to the protective SiO_2 layer.

To construct the overall profile for the injected carrier density, we use the same Gaussian profile for each side of the junction, multiply each half by opposing Heaviside functions, and include appropriate coefficients to the respective sides,

$$N_{MoS_2}(x) = \frac{\alpha_{MoS_2}}{\sigma\sqrt{2\pi}} e^{\frac{-(x-x_o)^2}{2\sigma^2}} \Theta(-x), \tag{5.5}$$

$$N_{MoSe_2}(x) = \frac{\alpha_{MoSe_2}}{\sigma\sqrt{2\pi}} e^{\frac{-(x-x_o)^2}{2\sigma^2}} \Theta(x), \tag{5.6}$$

The two sides are then added to one another to create the overall profile of the injected carrier density,

$$N(x) = N_{MoS_2}(x) + N_{MoSe_2}(x). \tag{5.7}$$

This profile at different values of x_o are shown in Fig. 5.8 (teal).

The convolution of $P(x)$ and $N(x)$ is then found according to 5.2,

$$C(x) = \int_{-\infty}^{\infty} P(x)N(x-x_o)dx_o \tag{5.8}$$

and shown in Fig. 5.8 (black).

Since the goal of this simulation is to mimic the results of the spatiotemporal measurements, we also need to include the dynamics of the injected carrier density. Since the dynamics are measured in the experiment by considering a relative difference in arrival time between the pump and probe pulses, we disregard any time dependence of the probe and focus on the appropriate time dependence in, $N = N(x,t)$.

The dynamics of the injected carriers have two main components, exciton lifetime and dif-

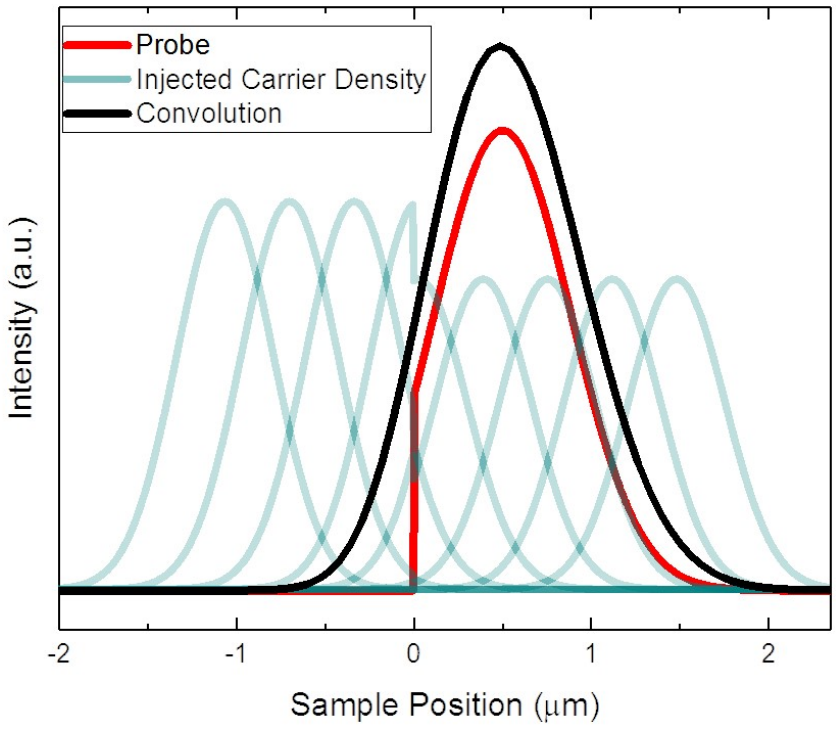

Figure 5.8: Depiction of how the spatial convolution is found in the simulation of the pump-probe experiment. The red curve represents the probe sensitivity profile. The teal curves are the injected carrier density profiles for different sample positions. The black curve is the convolution of the two at time, t=0.

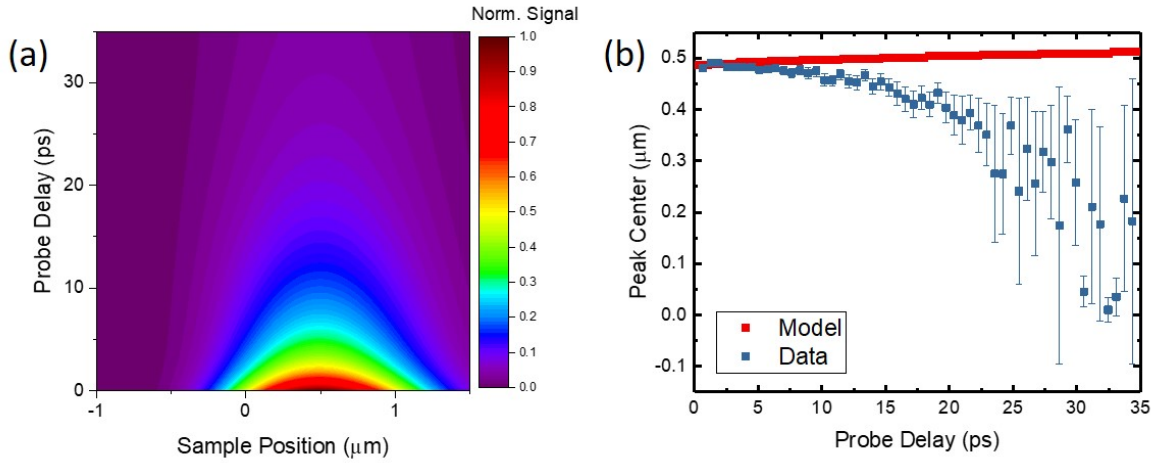

Figure 5.9: (a) Simulation of the spatiotemporal transient absorption experiment without the inclusion of carrier transfer. (b) Peak position as a function of probe delay as calculated by the model (red) and from the data (blue).

fusion. We will later consider the effects of transport across the junction. The exciton lifetime is included by multiplying $N(x)$ by the bi-exponential decay function previously fit to the data. Diffusion of the injected carriers is included by adding a time dependence to the Gaussian width, $\sigma = \sigma(t)$. This gives us

$$N(x,t) = (A_1 e^{-\frac{t}{\tau_1}} + A_2 e^{-\frac{t}{\tau_2}}) \frac{\alpha}{\sigma(t)\sqrt{2\pi}} e^{\frac{-(x-x_0)^2}{2\sigma^2(t)}} \Theta(x) \tag{5.9}$$

where,

$$\sigma^2(t) = \sigma_0^2 + 11.09Dt \tag{5.10}$$

with σ_0 being the initial width of the profile and D as the diffusion coefficient.

From this, we can calculate the convolution at several time steps and build a representation of the experiment, as shown in Fig. 5.9(a). Tracking the peak position, shown in Fig. 5.9(b), we show that the modeled distribution trends slightly towards the $MoSe_2$ side of the heterostructure, contrary to the measured data. This suggests that the model requires some sort of transfer component to better represent the mechanisms observed in the data.

Until now, we have not included any influences of the expected behavior of carriers at, or

near, the junction in this model. Regardless of injection site, the resulting excitons are expected to diffuse radially outward. However, due to the type-I band alignment, what happens at the junction is entirely dependent of which side they are injected. On the MoS_2 side, carriers can transfer across the junction. This can occur through the continuation of diffusive transport into $MoSe_2$ or through drift transport as a result of the built-in electrical potential from the conduction and valence band offsets at the junction. With the actual junction constituting such a small percentage of the total measured area, we only consider the diffusive aspect of this transfer.

In the model, this is implemented by adding a dynamic aspect to the Heaviside function that forms the MoS_2 side of the injected carrier distribution. For simplicity, we consider this process to be linearly time dependent, shown by,

$$N_{MoS_2}(x,t) = (A_1 e^{-\frac{t}{\tau_1}} + A_2 e^{-\frac{t}{\tau_2}}) \frac{\alpha}{\sigma(t)\sqrt{2\pi}} e^{\frac{-(x-x_O)^2}{2\sigma^2(t)}} \Theta(-x-vt) \tag{5.11}$$

where v, can be thought of as a transfer velocity parameter.

Figure 5.10 shows how this transfer effects the injected carrier distribution profile in the simulation. Here, the carrier density is only shown for the pump spot centered at the junction, $x_0 = 0$. For times $t > 0$, N_{MoS_2} extends further into the $MoSe_2$ side, adding to the distribution in $MoSe_2$. One way to look at this effect is as a maximum distance that carriers injected in MoS_2 can diffuse into $MoSe_2$ after a certain duration of time.

As for carriers injected on the $MoSe_2$ side of the junction, they are prohibited from transferring into MoS_2. This likely results in a built up of carriers near the junction. Previously, the model did not take into account the loss of the distribution on the $MoSe_2$ due to diffusive broadening across the junction. This is fixed by taking the difference between the integrals of the initial injected distribution in $MoSe_2$ and that at time, t, to find the total density lost. This is calculated as a function of both delay time and pump position. This contribution is then added back to the $MoSe_2$ side of the distribution with a fairly quickly decaying exponential profile to represent the build up of carriers at the junction.

Tuning both the transfer velocity parameter and the shape of the build up function, we try

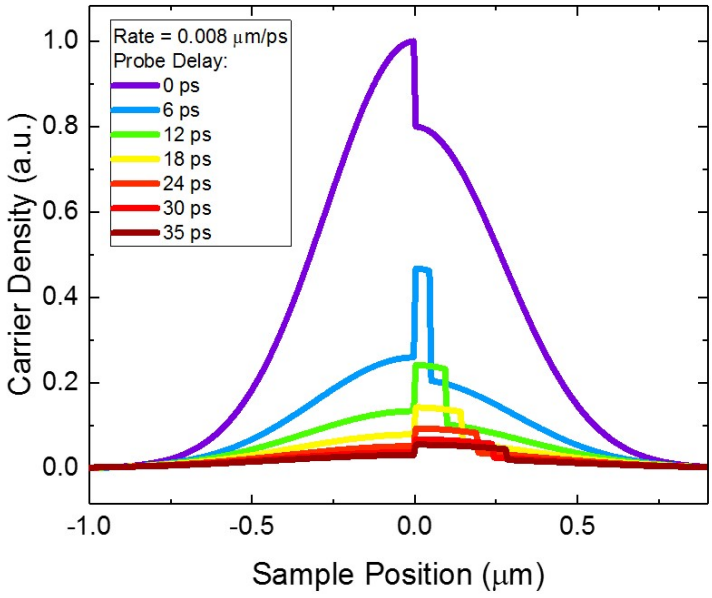

Figure 5.10: Injected carrier density profile centered at the junction for different probe delays. For simplicity, the displacement parameter, here, is varied linearly in time at a rate of 8×10^5 cm/s.

to match the observed shift of the distribution observed from the experiment. With the modeled distribution resulting in smooth convolutions, we can simply take the position of the maximum to represent the center position. The results of this fit are shown in Fig. 5.11(a). The fit was based on the first 20 ps. After 20 ps, the measured signal becomes significantly reduced making it difficult to reliably extract the center position.

The transfer velocity parameter is found to be about 10^6 cm s^{-1}. It is important to mention that this velocity results in a transfer length of 0.35 μm from the junction, which is reasonable considering a diffusion length of about 0.5 μm calculated from the diffusion coefficient and exciton lifetime in $MoSe_2$. Figure 5.11(b) shows the modeled evolution of the carrier distribution at a single injection site, a little more than 0.5 μm from the junction in $MoSe_2$. Here, we can see that the distribution diffuses outward over time from the center of injection, and the carriers transferring from MoS_2 provide a contribution near the junction that increases over time.

Ultimately, these results give great promise not only for the potential of 2D lateral heterostructures, but the ability to observe different transport phenomena in ultrathin systems. We find that

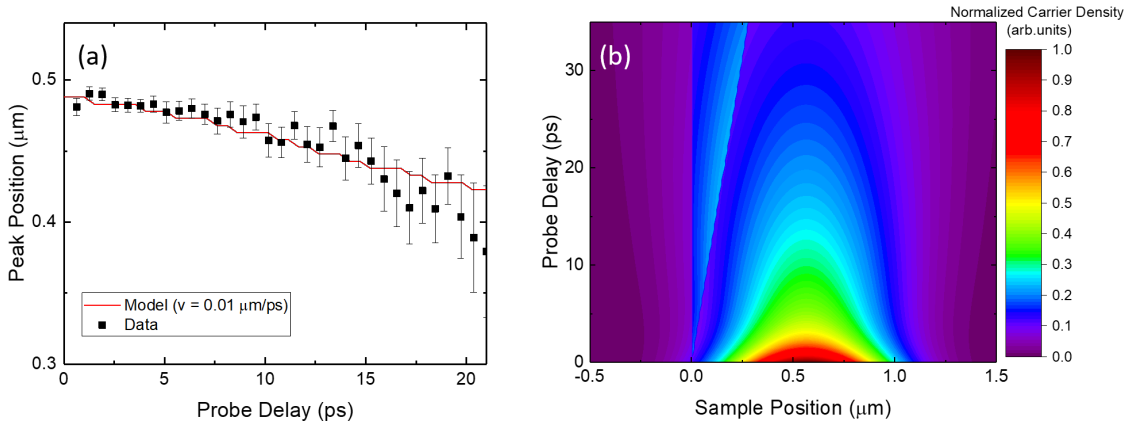

Figure 5.11: (a) Peak position extracted from the measured data (black squares) and the model (red line) as a function of probe delay. The model uses a value of 0.01 μm/ps for the velocity parameter. (b) Contour plot of the modeled carrier density as function of sample position and probe delay. This is for a single injection site (pump spot position), centered a little more than 0.5 μm into $MoSe_2$, to show how the transfer and build up functions effect the distribution.

lithographically patterned MoS_2-$MoSe_2$ heterostructures indeed form a semiconductor junction with type-I band alignment. This facilitates exciton transport from MoS_2 to $MoSe_2$ at a rate on the order of 10^6 cm s^{-1}. This proven ability to directly observe the evolution of an optically injected carrier distribution is especially promising for the discovery of new revelations in carrier transport phenomena in 2D materials and heterostructures.

Chapter 6

Lateral Homostructures Formed in Monolayer TMDs

6.1 Introduction to TMD Lateral Homostructures

The previous section looked at carrier dynamics at the 1D interface between two different TMD MLs. Another area of importance for 2D materials research is the formation of electronic junctions within the same sheet of a single material, referred to, here, as a homojunction. Several studies in recent years have shown the ability to create effective homojunctions within monolayer TMDs. This has been demonstrated through electronic doping[92–94], chemically doping[95], as well as through altering the dielectric environment surrounding a 2D material[36;96].

From an applications standpoint, the use of local gates to modify the electronic structure in different areas of a semiconducting material holds a lot of promise. Several groups have shown the ability of this method to create semiconducting junctions that effectively modulate current flow under certain dual-gate bias conditions[92–94]. In cases where the material is ambipolar, the different gate biases will actually create both a P-doped and N-doped side, making a true P-N junction. This can lead to multi-functional devices, which under different bias configurations can operate as transistors, LEDs, or photovoltaics. The use of chemical doping or other methods involving more permanent homojunction formation will tend to create a sharper interface. This is due to the formation of the junction by either lithographic techniques or simply at the straight edge between a ML and multilayer sample. In chemical doping, the two sides are oppositely doped to either N or P, making a PN junction[95]. With a layer-dependent band energy in many 2D materials, lateral junctions can also form at the interface between ML and multilayer samples[96]. With the mechanism often being explained by Coulomb screening effects, altering the dielectric

environment of a sample area effectively creates a junction[36]. For example, partially covering a ML region through vdWs stacking would be expected to alter the band structure in the covered portion creating a junction at the interface between the covered and non-covered regions.

Ultimately, studying this effect is not only important for potential applications, but also for the understanding of more complex layered structures. With industry trends beginning to move towards 3D device integration, it is likely that future applications of 2D materials will also involve the 3D integration of several diverse layers. Thus, a thorough understanding of in-plane effects as a result of vertical layering is imperative to the discussion. In this section we will begin to explore this by looking at the formation of a lateral junction within a ML TMD, $MoSe_2$, by adding relatively thick layers of hBN over a portion of the ML. With hBN being an electrically insulating material, we do not expect any out-of-plane interaction, and thus focus on the in-plane junction created at the boundary between the covered and uncovered regions of the samples.

6.2 Junction Formation in $MoSe_2$ Monolayer by Increased Coulomb Screening

Samples for this project were fabricated by mechanical exfoliation onto PDMS substrates. First, ML $MoSe_2$ flakes are transferred from the PDMS onto Si/SiO_2 (90 nm) substrates and annealed at 200°C in a H_2/Ar environment for 2 hrs. Relatively thick hBN flakes (~5-10 nm), estimated by optical contrast, are then transferred on top of the $MoSe_2$ partially covering the material, leaving enough area exposed to facilitate measurements across the junction, as well as, either side. One of the samples used in this study is shown in Fig. 6.1(a).

To characterize the samples, we perform photoluminescence spectroscopy measurements. Here, a 405 nm continuous wave laser is focused through a 100× objective lens. The resulting emission spectra for the uncovered and hBN-covered regions of the ML $MoSe_2$ sample are shown, normalized, in Fig. 6.1(b) in red and blue, respectively. The magnitude of the PL peak from the covered sample was found to be noticeably larger, by factor of about 2.4, which can be attributed to fewer

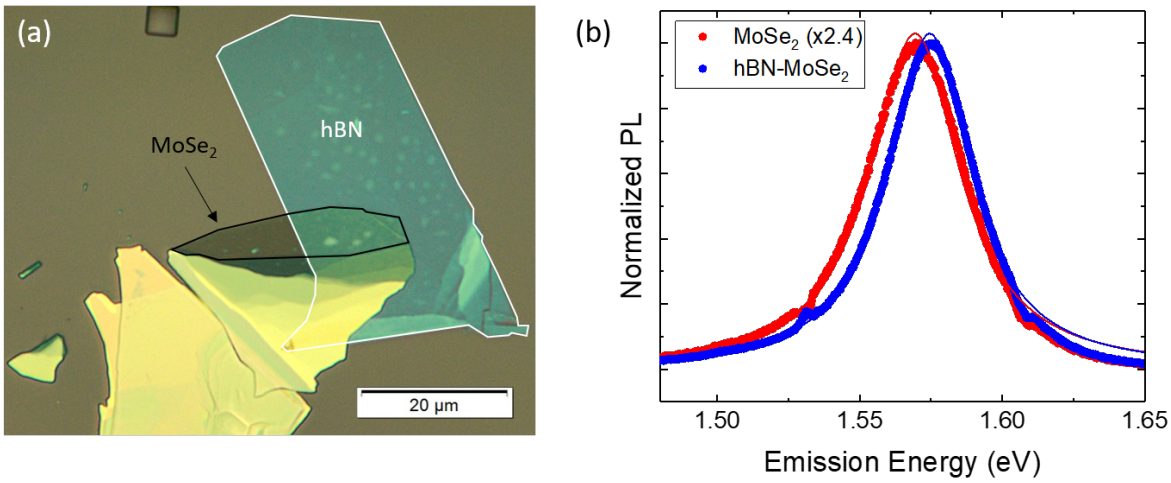

Figure 6.1: (a) Optical image of one of the samples used in this experiment. (b) Photoluminescence measurements for ML $MoSe_2$ (red) and ML $MoSe_2$ covered with hBN (blue)

defects in the covered area. With measurements taken under ambient conditions, influences such as H_2O absorption and moderate sample degradation from slow oxidation processes can increase defect sites and thus reduce radiative recombination yields. The use of hBN as a passivation layer has been widely shown to lessen these effects and preserve sample integrity.Fitting the peaks with Lorenz functions, we find that the ML $MoSe_2$ has an emission energy of 1.569 eV, that blue shifts as much as 12 meV when covered by hBN.

Initially, one would expect to observe a larger shift in the PL emission energy as a result of the changing dielectric environment. Increased dielectric screening in the hBN covered region, is expected to largely reduce the exciton binding energy, as previous reports have shown, up to several hundred meV[36]. However, as seen from the layer dependent electronic structure, it is known that increased screening effects significantly alter the band gap in these materials[38]. As mentioned in Sect. 2.1, the optical band gap is lower than the electronic band gap due to exciton binding energy. The optical gap is actually considered to be the difference between the electronic gap energy and the exciton binding energy. In our case, then, it actually makes sense that we do not see a large change in the energy of PL emission as one of these effects would increase the energy, while the other decreases it.

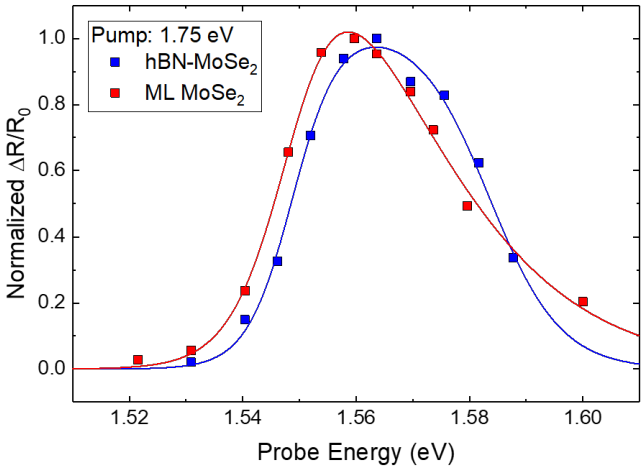

Figure 6.2: Normalized peak differential reflection signal for different probe wavelengths as measured from ML $MoSe_2$ (red) and hBN covered $MoSe_2$ (blue)

Next, we measure the peak differential reflection on each side of the junction as a function of the probe wavelength. We inject carriers in the sample using a 1.75 eV pump focused through a $100\times$ objective lens to a spot size of about 0.9 μm. With a peak injected fluence of 13.9 μJ cm^{-2}, this corresponds to a carrier density of about 4.74×10^{11} cm^{-2}, based on an absorption coefficient of 1.37×10^{7} m^{-1} in $MoSe_2$ for this pump energy. The normalized peak differential reflection at each probe energy is shown in Fig. 6.2. Here, the results measured from the uncovered $MoSe_2$ is shown in red and the hBN-covered area shown in blue. The fit lines are based on an asymmetrical double sigmoidal function (eq. 5.1). From these fits, we find peak positions of about 1.55 eV and 1.56 eV from the uncovered and covered regions, respectively. Similar to the PL results, there is a noticeable blue shift (10 meV) of the dependence when covered with hBN.

Measuring the differential reflection signal in both regions as a function of probe delay, we find a noticeable difference in the exciton lifetime in the two regions. This is shown in Fig. 6.3, for a 1.57 eV probe. Here, we use the same injected fluence and pump energies as above for a 1.75 eV pump. Each curve is fit with a bi-exponential decay with a baseline,

$$\frac{\Delta R}{R_0} = A_0 + A_1 e^{-\frac{t}{\tau_1}} + A_2 e^{-\frac{t}{\tau_2}} \tag{6.1}$$

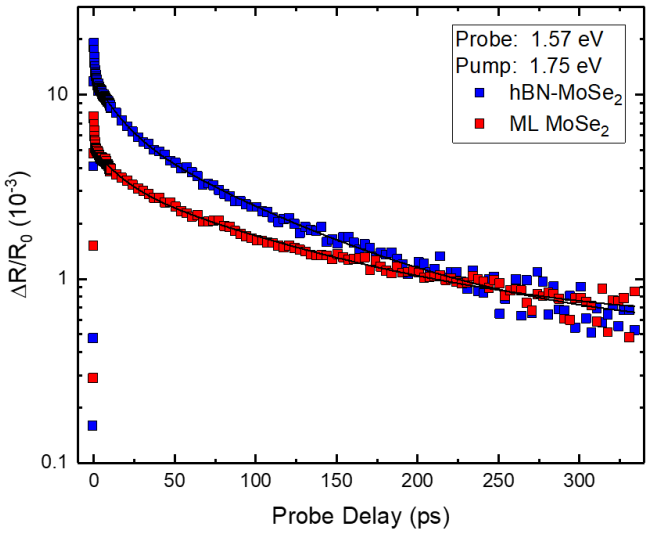

Figure 6.3: Differential reflection measurements as a function of relative probe delay for $MoSe_2$ (red) and hBN covered $MoSe_2$ (blue)

as shown by the black curves. Each of these fits begins after an very short lived decay process that is attributed to exciton formation. From this bi-exponential fit, we find two different time-dependent processes. The first, represented by τ_1, takes 16 ± 2 ps on each side of the junction, and is likely attributed to the exciton-exciton annihilation or hot excitons[33;34]. The second process, found by τ_2, represents the exciton lifetime on each side. This is found to be 114 ± 9 ps on the uncovered side, and 88 ± 4 ps on the hBN-covered side. The decreased exciton lifetime when covered with hBN is likely the result of decreased exciton binding energy from increased dielectric screening. It is also interesting to note, similarly to the PL yield in the two regions, the covered region provides a signal about $2.5\times$ stronger than the uncovered region.

6.2.1 Spatiotemporally Resolved Carrier Distributions in $MoSe_2$ and hBN Covered $MoSe_2$

In addition to measuring the differential reflection as a function of probe delay, we also measure $\Delta R/R_0$ as a function of the relative separation between the pump and probe positions. Here, the

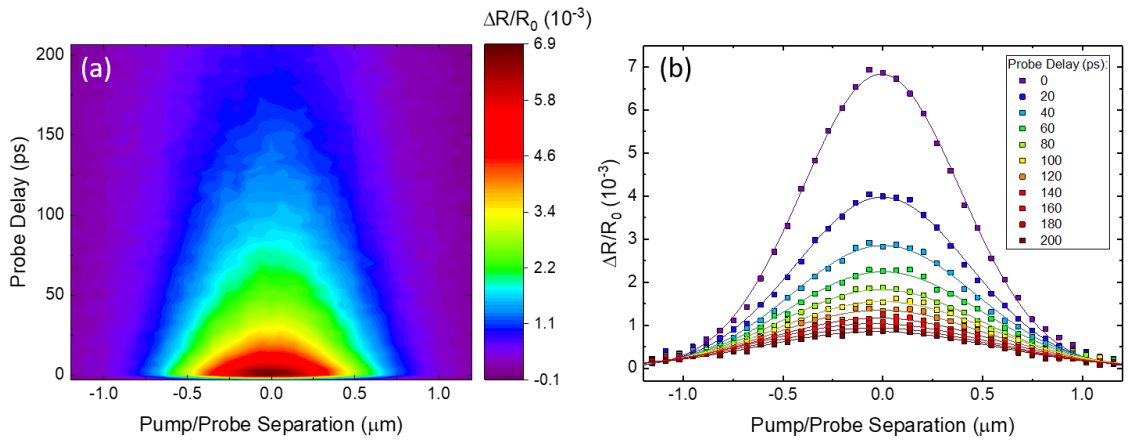

Figure 6.4: (a) Spatiotemporally resolved differential reflection measurements on uncovered ML $MoSe_2$. (b) Spatial profiles at each time step for the data in (a). The color-coded lines are Gaussian fits to each data data.

1.75 eV probe is held at a constant position on the sample and the intensity of the reflection is measured for different spatial positions of the pump.

First, we use this technique to look at the dynamics in the uncovered portion of the $MoSe_2$ sample. The same 1.75 eV pump, as used above, again injects carriers in the sample with a density of about 4.74×10^{11} cm^{-2}, at different relative positions to the probe spot. The resulting differential reflection of the probe as a function of this separation and probe delay is shown in Fig. 6.4(a). The corresponding spatial profiles for several probe delays are shown in Fig. 6.4(b). These profiles are the spatial convolution of the injected carrier density and the probe profile. Since both the pump and probe beams are spatially Gaussian, this convolution is also expected to be Gaussian at each time step, assuming the carrier density diffuses isotropically outward. We thus fit the spatial profiles using Gaussian functions (color coordinated lines) to extract both the center position and FWHM of each. Here, it is important to note that the center of each profile is found to be roughly constant.

Next, using the same experimental setup, we measure the response from the hBN covered area of the sample. Here, we try to measure sufficiently far away from the junction, as well as, find an area free from interlayer contaminants. The results are shown in Fig. 6.5(a). The spatial profiles for different delay times are shown in Fig. 6.5(b). Oddly, we see the distribution shift to the right. This

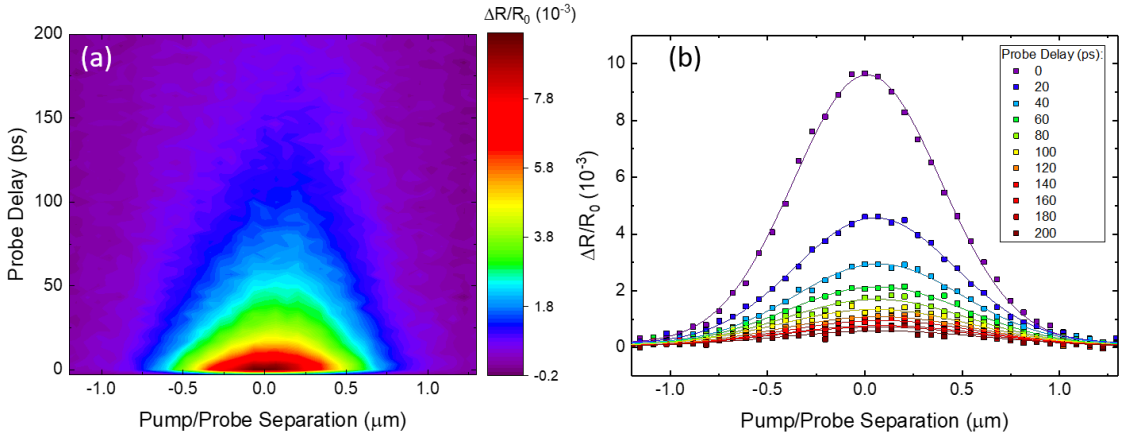

Figure 6.5: (a) Spatiotemporally resolved differential reflection measurements on hBN covered ML $MoSe_2$. (b) Spatial profiles at various time steps for the data in (a). The color-coded lines are Gaussian fits to each set of data.

could be caused by non-uniformity in the sample due to trapped contaminants between the $MoSe_2$ and hBN layers. Nonetheless, the profiles maintain a Gaussian shape and are thus fit accordingly (color coordinated lines).

From the Gaussian fits of each dataset, the FWHM and center position for every time step is extracted. Using the squared width, we deduce the diffusion coefficients in the two regions of the sample. The squared widths as a function of delay time for the covered (blue) and uncovered (red) regions are shown in Fig. 6.6. By the relation $w^2 = w_0^2 + 11.09Dt$, we are able to obtain the diffusion coefficient from the slope of the linear fits (blue and red lines). The diffusion coefficients are found to be 4.36 $\pm$ 0.08 $cm^2\ s^{-1}$ and 3.12 $\pm$ 0.15 $cm^2\ s^{-1}$ for the covered and uncovered regions, respectively.

6.2.2 Exciton Drift at the Lateral Junction Between Uncovered and Covered $MoSe_2$

Next, we focus our attention on the junction between the covered and uncovered areas. If there is transport of injected carriers across the junction due to a change in band energy in the hBN-covered $MoSe_2$, performing the same experiment should show a drift of the carrier distribution towards one

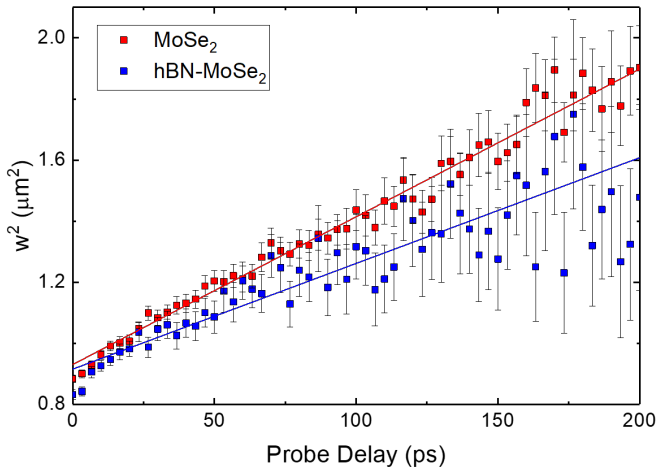

Figure 6.6: Squared width of the Gaussian profiles in 6.4(b) (red) and 6.5(b) (blue) as a function of probe delay. The lines are linear fits to extract the diffusion coefficients.

side or the other. If there is no carrier transport, the shape of the spatial profiles would be expected to simply broaden and not shift in either direction. It should also be mentioned a shift in the effective work function of $MoSe_2$, without a change to the gap energy, would be expected to create a type-II junction, resulting in charge separation. In this case, one would expect the distribution to split into two peaks.

Here, trying to better resolve any possible transfer, we inject carriers with a less energetic, 1.675 eV pump. With an absorption coefficient of 1.34×10^7 m^{-1}, and peak injected fluence of 27.8 μJ cm^{-2}, we are injecting a peak areal density of 9.64×10^{11} cm^{-2}. Since we are injecting and probing carriers in both layers, a lower energy pump should reduce the effects seen from hot carriers in the early stage dynamics and should help us to observe more of the effects from transport phenomena.

For these measurements, the probe laser spot is centered as close to the junction as possible. This is to more reliably track the center position of the distribution. The peak signal at zero delay should be at the best overlap position of the pump and probe, which here is very near the junction. This way, any shift of the profile is likely a sign of transport in that direction. The results are shown in Fig. 6.7(a). The black line represents the estimated position of the junction between the

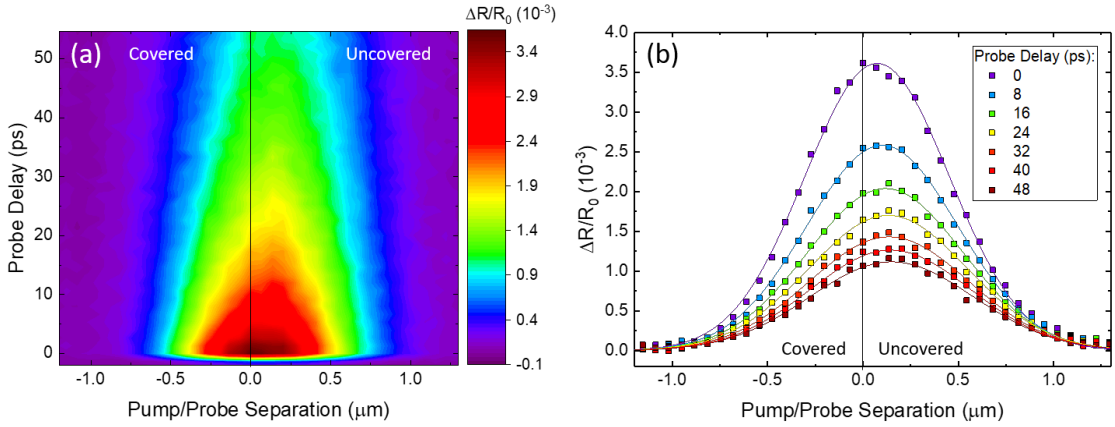

Figure 6.7: (a) Spatiotemporally resolved differential reflection measurements with the probe placed at the junction between the hBN covered and uncovered areas of $MoSe_2$. (b) Spatial profiles at various time steps for the data in (a). The color-coded lines are Gaussian fits to each set of data.

hBN-covered and uncovered sample regions. The corresponding spatial profiles for different probe delays are shown in Fig. 6.7(b). Again, each profile is fit with a Gaussian function.

From the Gaussian fits, we extract the peak position of the distribution at each time step. Tracking this position provides a good way to observe if there is carrier transport across the junction. The center position as a function of the probe delay is shown in Fig. 6.8 for all three datasets, uncovered $MoSe_2$ (red), hBN-covered $MoSe_2$ (blue) and the junction (white).

As expected, the uncovered region shows no noticeable deviation from the initial center position. We do see a shift of the profile in the covered region, which as explained earlier, may be due to non-uniformity in that region from trapped residue during the transfer process. Finally, we see a very noticeable shift of the peak position when focusing on the junction. The shift is towards the uncovered side of the junction and would suggest that there is exciton transfer in the observed direction and thus type-I band alignment. In an attempt to quantify the dynamics across the junction, we can simply take derivative of the peak position over time. To do this, we first fit the peak position data measured at the junction. At this point, we are trying to extract a mathematical expression for the data over this range and are less focused on the underlying physics. Given this, we fit the data using a simple rational function,

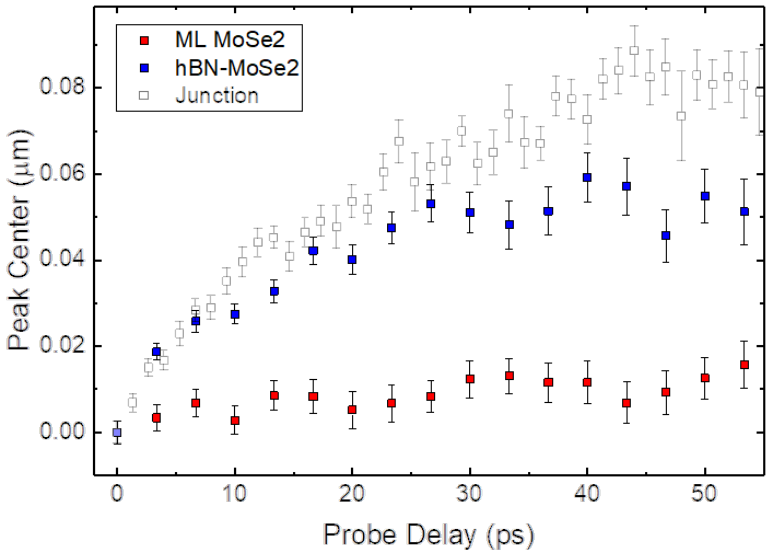

Figure 6.8: Center position of each spatial profile from the peak fitting of the spatial profiles for ML $MoSe_2$ (red), hBN covered $MoSe_2$ (blue), and the junction between them (white)

$$y = \frac{cx}{(a+x)} \tag{6.2}$$

with fitting parameters c and a. With this fit representing the position of the distribution as a function of time, the derivative can be considered the distribution velocity or drift velocity. We can then plot this velocity as a function of sample position based on the previous relation between position and time. This is shown in Fig. 6.9. The inset shows the data and fitting function.

With an expectedly sharp interface between the covered and uncovered regions, and thus a very localized built-in potential, this trend of the velocity would seem to agree with assumptions. The peak velocity of about 8×10^5 cm s^{-1} is also reasonable compared to previously studies on exciton transport, which found excitons could be acoustically driven, on the order of the speed of sound in GaAs based quantum wells[195;196]. Given the exciton lifetime and diffusion coefficient found in $MoSe_2$, it is important to note that the observed drift length of roughly 100 nm is consistent with the diffusion length, $L = \sqrt{D\tau}$.

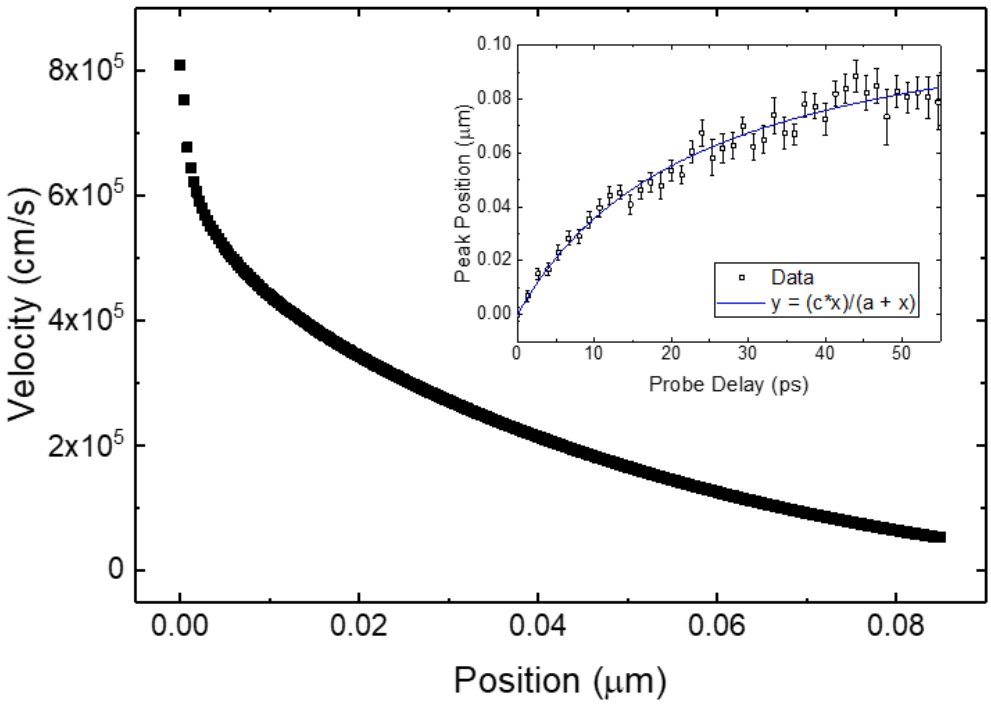

Figure 6.9: Derivative of the peak position with respect to probe delay plotted as function of position. The inset shows the fit of the peak position using eq. 6.2.

6.3 Summary

In this chapter, lateral, in-plane homojunctions were explored in 2D materials. Specifically, the formation of an electronic interface between bare ML $MoSe_2$ and hBN-covered $MoSe_2$ was studied. The electronic structure of $MoSe_2$ was expected to be altered due to increased dielectric screening when covered by fairly thick hBN. These effects were observed by slight blue shifts in both the photoluminescence spectrum and peak differential reflection measurements. A reduced exciton lifetime in the covered region is also strong evidence of increased screening effects.

Through spatiotemporally resolved differential reflection measurements, it was shown that the injected photocarrier distribution diffuses isotropically in the uncovered $MoSe_2$, but near the junction the distribution shifts away from the hBN-covered region and more into the uncovered region. By tracking the peak position of the distribution as a function of delay time, we are able to infer information about the drift transport near the junction. As expected, the distribution moves fastest near the junction due to a sharp built-in potential, quickly slowing down as it moves away.

These results provide important information about the formation of electronic interfaces in 2D materials. The ability to modulate the electronic structure of MLs through vdWs stacking is also a key observation. Although other methods of homojunction formation in layered materials may be more relevant or easily implemented in applications, it is crucial to understand the in-place effects resulting from out-of-plane interactions.

Chapter 7

Summary and Outlook

With the emergence of research on 2D materials and their vast potential for uses in the electronics and optoelectronics industries, it is imperative to continue studying their properties both individually and in heterostructures. This dissertation has been focused on ultrafast optical studies of carrier dynamics in several unique heterostructure configurations. The goal has been to highlight different mechanisms that dictate charge and energy transfer across low dimensional, electronic interfaces.

We started by looking at vertical heterostructures between crystalline TMD layers. These vertical structures all involved the stacking of individual MLs by vdWs adhesion. Despite fairly weak mechanical coupling between layers, the electronic interaction between the two surfaces is shown to actually promote ultrafast charge or energy transfer. Here, we looked at 3 different samples. Photoluminescence measurements showed charge separation and the formation of trions in a $MoSe_2$-WS_2 heterostructure. These results displayed the type-II, band alignment at the interface, which is common to most TMD heterostructures.

With type-II structures so prevalent in the 2D realm, we next looked at two heterostructures predicted to have type-I band alignment. These were WSe_2-$MoTe_2$ and MoS_2-ReS_2. Ultrafast pump-probe experiments showed that both types of charge carriers indeed transferred from the larger gap materials to the smaller gap materials, confirming the suspected type-I alignment. With a transfer process in the WSe_2-$MoTe_2$ sample occurring more than twice as fast as in the MoS_2-ReS_2 sample, it is believed that the matching of crystal structures could play an important role in the mechanisms behind charge and energy transfer across 2D sheets.

Next, the results from studies on heterostructures formed between atomically thin crystalline

and amorphous semiconductors were explored. The amorphous material in this case was amorphous black phosphorus. Obtaining these ultrathin aBP samples near the infancy of their discovery, little was known about their basic properties as it pertains to our measurements. These properties, such as exciton lifetime and diffusion characteristics, were studied first to better understand the carrier dynamics in these samples. Temporally and spatially resolved pump-probe experiments showed exciton diffusion coefficients in the thinner samples were orders of magnitude larger than those found in more established amorphous materials like silicon. With the promising characteristics in the thinnest of aBP samples, we attempted to look at possible charge transfer between aBP and TMD MLs. Using both PL spectroscopy and transient absorption measurements, we studied the interaction between aBP and ML WS_2. Despite the junction being held together by vdWs adhesion between very dissimilar material structures, we found there to be efficient charge transfer between the two materials. The evidence for this included exotic excitonic behavior when separated by a thin insulating barrier and significant differences in the exciton lifetime observed between isolated WS_2 and the direct heterostructure. These results showed promise for applications involving the enhancement of amorphous materials.

The focus was then shifted to in-plane, lateral heterostructures. These samples consisted of alternating strips of ML MoS_2 and $MoSe_2$, patterned by lithographic techniques. With type-I band alignment at the junction, we observed strong evidence of lateral exciton transport from MoS_2 to $MoSe_2$. By selectively probing the smaller gap material, $MoSe_2$, we directly measured the build up of carriers near the junction using spatially resolved transient absorption techniques. From this, a model was derived to extract a more quantitative analysis of the exciton drift across the junction.

Finally, with a method in place to resolve the movement of a carrier distribution over time, we studied the possible transport across a lateral homostructure. In this case, partially covering a ML TMD, namely $MoSe_2$, with thick flakes of insulating hBN, forms a lateral interface in $MoSe_2$ between the two regions. Stacking hBN on top of the ML significantly alters the electronic structure in $MoSe_2$ by increasing the out-of-plane dielectric screening, thus reducing the Coulomb interaction of injected electron-hole pairs. Evidence of this effect is found from a decreased exciton

lifetime in the covered region of the sample as a result of a smaller exciton binding energy. With an effective junction created at the interface between the two regions, we then use the spatially and temporally resolved pump-probe technique used previously to observe the drift of the distribution over time. We find that the distribution moves towards the uncovered side, implying both an increase in the gap energy in the covered region and type-I band alignment at the junction.

Overall this work highlights several different attributes of transfer phenomena at low dimensional semiconducting interfaces. Not only do these projects highlight the vast diversity of this research area, but also explore some previously unexplored structures. With a likely more prevalent implementation of 2D materials for industry applications in the future, it is important to understand these mechanism.

Appendix A

Fabrication and Characterization of vdWs Heterostructures

A.1 Mechanical Exfoliation and vdWs Stacking

Since the experimental isolation of monolayer graphene in 2004, one of the most common methods for fabricating monolayer samples for small scale experiments is mechanical exfoliation[2]. In this process, bulk crystals of a layered material are placed on to an adhesive tape. The tape is then folded over to cover both sides of the bulk crystal and then pulled apart, separating the crystal into two thinner pieces. This process is repeated several times, resulting in thinner and thinner fragments of the material on the tape. Once thinned down enough, the tape is then placed onto a desired substrate and pulled off. For most of the samples made for the projects in this dissertation, polydimethylsiloxane (PDMS) and oxide capped silicon substrates were used. Resulting from the vdWs interaction between the layered material and the substrate, several flakes, varying in thickness, adhere to the substrate rather than remaining attached to the bulk crystal. This process has proven effective at creating high quality flakes, as thin as monolayer. Factors such as the surface energy between the layered material and substrate, type of adhesive tape, and environmental conditions can all play roles in size and yield of ML flakes. Due to this variability and with the desire to fabricate large scale crystals for future industry use, other methods such as chemical vapor deposition and epitaxial growth of ML samples have been widely explored. However, for small scale experiments aimed at more fundamental exploration of material properties, exfoliated samples are used because of their superior quality.

With the ability to exfoliate layered materials down to their ML limit, it is of increasing interest to stack these MLs to form ultrathin heterostructures. This can be done by utilizing the same

procedure mentioned above for as many layers are desired. The stacking process is outlined in Fig. A.1. Monolayer flakes are exfoliated onto PDMS substrates that are adhered to glass slides by the natural interaction between the them. The PDMS provides a transparent medium so that MLs can be identified from both the top and bottom, under a microscope. The glass slide is then flipped upside down under a microscope equipped with long working distance objective lenses so that the ML sample is facing downward. Using micro-manipulators, the sample is then slowly lowered onto a SiO_2 substrate until contact is made. The exfoliated flakes then interact more strongly with the SiO_2 substrate than the PDMS completing the transfer process. The use of the microscope and micro-manipulators allows for very precise control over the placement of transferred samples to within about 1 μm. This makes it attainable to stack separately exfoliated flakes into effective heterostructures.

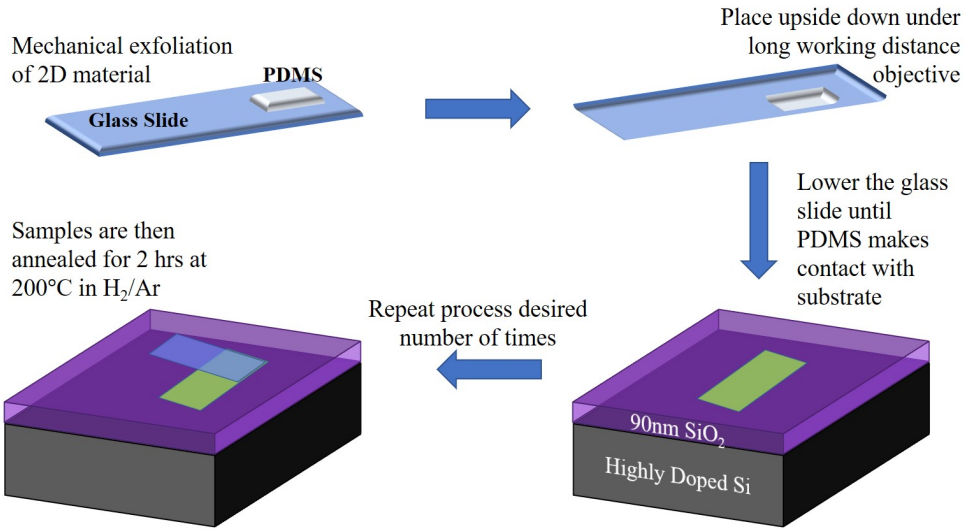

Figure A.1: Schematic of the process for transferring and stacking 2D materials. The green and blue shapes in the bottom to panels represent flakes of the materials being transferred.

Once stacked, the samples are often annealed to better couple the interaction between layers and clean possible residue and contaminants left from adhesive tape or other steps in the fabrication process. The annealing process involves placing the samples in a controlled environment under the flow of Ar/H_2 gases held at a base pressure of about 3 Torr. Using a furnace, the sample is then heated to around 200 °C. This temperature can vary based on the materials involved as some, like

black phosphorus, easily degrade if too hot.

A.2 Optical Contrast Methods

Once fabricated, it is important to confirm the suspected thickness of these layered samples. In most cases, this is done by determining how many discrete layers comprise the sample, which can later be related to a more physical thickness if needed. Because of this layered nature, one of the most common practices is the measurement of optical contrast from a sample image. The main advantage of this method is that it does not require special equipment uncommon to most laboratory settings. Simply using a CCD equipped microscope to take an optical image of the sample and free computer software to extract image data is all that is needed.

The optical contrast for a certain region of the sample can be found by

$$C = \frac{I_{substrate} - I_{sample}}{I_{substrate}}, \tag{A.1}$$

where I represents the measured gray scale intensity. This intensity is found by splitting a color image into its three channels, blue, green, and red, and choosing the one that provides the best contrast. Studies have been done to calculate the expected optical contrast for various atomically thin materials as a function of wavelength and substrate thickness[136;197;198]. Most find that either red or green color channel provides a reasonable contrast for commonly accessible Si_2 substrate thicknesses of around either 90 or 300 nm. One the other advantageous results is that in the few layer limit, the contrast scales linearly with layer number, with each layer contributing about a 10-15 % contrast.

An example of this process, using the sample from Sect. 3.2.2, is shown in Fig. A.2. Here, an optical image taken from a CCD attached to a microscope is split into the three color channels. Using the green channel image, the profile of the gray scale intensity is measured along path of the yellow line. Using eq. A.1, the contrast is calculated relative to the substrate, inset of Fig. A.2, for the two materials involves, ReS_2 and MoS_2. It is seen that both layers have a very similar contrast

of about 12.5 %, which is consistent with other reports using comparable methods[136–138].

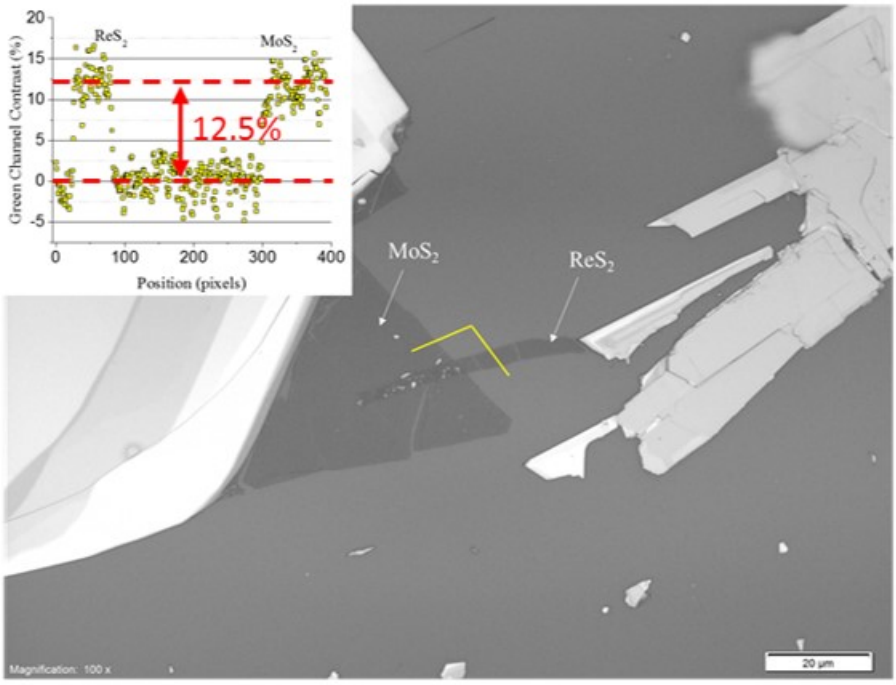

Figure A.2: Green channel image of the ReS_2-MoS_2 heterostructure. The inset shows the measured contrast along the yellow line. Adapted from Ref. 135 with permission from The Royal Chemical Society.

A.3 Other Characterization Methods

Although optical contrast is a fairly quick and easy way to characterize sample thickness of layered materials, it is important to have other methods to confirm its reliability. A few of the common tools employed are atomic force microscopy (AFM), Raman spectroscopy, and as mentioned in 2.1, PL spectroscopy.

The first, AFM, involves a more direct measurement of thickness by mapping the topography of a sample. As the name suggests, AFM measures the force between an atomically sharp tip and the sample. This tip is typically mounted on a small cantilever, which when very close to the sample, gets deflected based on the interaction between the two. A common way to measure this deflection utilizes a photo-detector to track the position of a laser beam reflected off the back of the cantilever[110]. Scanning the tip across the sample area provides a map of this deflection and thus

the resulting topography. AFM has been shown to have sub-nm resolution in measuring topography, making it suitable for even the thinnest 2D materials. However, with thicknesses comparable to the resolution, it can still sometimes be difficult to confirm between 1-2 layers. Using functionalized probes can also provide other information beyond topography, like in magnetic force microscopy (MFM) where magnetic nano-particles are attached to the tip to measure the magnetic forces between tip and sample.

Spectroscopic techniques can provide other useful insights into material properties, as well as help determine thickness based on layer dependent trends. As discussed previously, PL spectroscopy gives insights into energy relaxation mechanisms in semiconductor materials. The transition from direct band gap semiconductors in ML to indirect gap semiconductors in 2+ layers, results in significantly larger PL signals in ML samples. This phenomenon, as well as trends in optical band gap with thickness makes PL a useful tool for characterization.

Raman spectroscopy, on the other hand, is useful in determining vibration modes, crystal structure, and again due to layer dependent trends sample thickness for layered materials. This technique indirectly measures vibration transitions based on photon scattering mechanisms. Typically, a laser is shown incident on a sample with much of the light being reflected back with the same energy, *i.e. Rayleigh scattering*. Due to excited vibrational states of the crystal lattice, some of the incident photons either lose or gain energy through either Stokes or anti-Stokes Raman scattering, respectively. A Raman spectrum, then, consists of peaks related to the Raman shift of these scattered photons relative to the energy of the incident photons[199;200]

For 2D materials, in particular, Raman spectroscopy illuminates impacts of interlayer interactions as out-of-plane vibrational modes are intuitively sensitive to their surroundings[139;173]. This becomes useful for determining the number of layers of a 2D sample using well established trends from literature. A few examples as they pertain to the projects in this dissertation are highlighted in Fig. A.3. Both of these are expansions on the characterization of the MoS_2 and ReS_2 layers in Sect. 3.2.2.

First, the Raman spectra measured from ML (blue) and bulk (red) MoS_2 are shown in Fig.

A.3(a). Here, a 532 nm laser is used to excite the sample. There are two noticeable peaks that are each fit the with Lorentzian functions. The resulting positions for monolayer were found to be 385.05 ± 0.05 and 404.10 ± 0.04 cm-$^{-1}$, representing the E_{2g} and A_{1g} vibrational modes, respectively. Previous studies have shown that the separation between these two peaks is a strong indication of layer number with relative Raman shift between them increasing with increased number of layers. From our measurements on bulk, we see a clear broadening of this separation, consistent with previous studies[139].

Raman measurements for the ReS_2 sample are presented in Fig. A.3(b). As discussed in Chenet *et al*[201], four characteristic peaks in ReS_2 between 120-170 cm^{-1} can be used to identify sample thickness. These peaks are labeled I - IV in Fig. A.3(b). Taking the difference between the positions of peaks I and III leads to a significant difference between monolayer and thicker ReS_2. They observed a difference of 16.8 cm^{-1} between these peaks in monolayer that drops to 14.9 cm^{-1} in bilayer and drops further in thicker samples[201]. Our result of 16.7 cm^{-1} closely matches their results for monolayer ReS_2. Other reports on ReS_2 Raman spectra also show the presence of low frequency, shear and breathing, modes that occur in bilayer ReS_2, but are not present in monolayer[202;203].

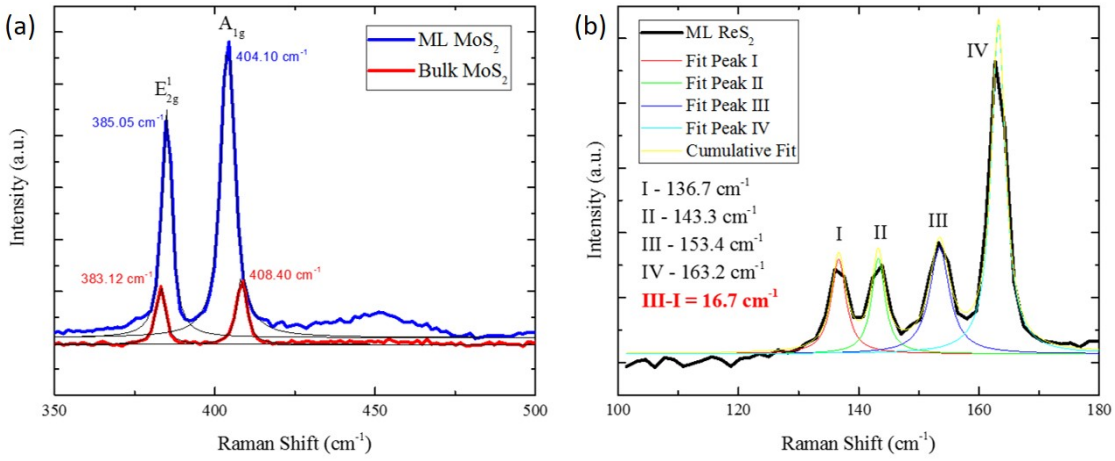

Figure A.3: Raman spectroscopy measurements from the (a) MoS_2 and (b) ReS_2 regions of the sample. (a) Shows both the spectrum for ML MoS_2 (blue) and bulk MoS_2 (red). The fitted curves in each are Lorentz fits. Adapted from Ref. 135 with permission from The Royal Chemical Society.

References

[1] A. K. Geim and K. S. Novoselov. The rise of graphene. *Nat. Mater.*, 6:183–191, 2007.

[2] K. S. Novoselov, A. K. Geim, S. V. Morozov, D. Jiang, Y. Zhang, S. V. Dubonos, I. V. Grigorieva, and A. A. Firsov. Electric field effect in atomically thin carbon films. *Science*, 306:666–669, 2004.

[3] C. Berger, Z. Song, X. Li, X. Wu, N. Brown, C. Naud, D. Mayou, T. Li, J. Hass, A. N. Marchenkov, E. H. Conrad, P. N. First, and W. A. de Heer. Electronic confinement and coherence in patterned epitaxial graphene. *Science*, 312:1191, 2006.

[4] K. S. Kim, Y. Zhao, H. Jang, S. Y. Lee, J. M. Kim, K. S. Kim, J. H. Ahn, P. Kim, J. Y. Choi, and B. H. Hong. Large-scale pattern growth of graphene films for stretchable transparent electrodes. *Nature*, 457:706, 2009.

[5] S. Park and R. S. Ruoff. Chemical methods for the production of graphenes. *Nat. Nanotechnol.*, 47:12, 2009.

[6] E. Gibney. The super materials that could trump graphene. *Nature*, 522:274–276, 2015.

[7] A. H. C. Neto and K. Novoselov. New directions in science and technology: two-dimensional crystals. *Rep. Prog. Phys.*, 74:082501, 2011.

[8] Q. H. Wang, K. Kalantar-Zadeh, A. Kis, J. N. Coleman, and M. S. Strano. Electronics and optoelectronics of two-dimensional transition metal dichalcogenides. *Nat. Nanotechnol.*, 7: 699–712, 2012.

[9] S. Z. Butler, S. M. Hollen, L. Cao, Y. Cui, J. A. Gupta, H. R. Gutiérrez, T. F. Heinz, S. S. Hong, J. Huang, A. F. Ismach, E. Johnston-Halperin, M. Kuno, V. V. Plashnitsa,

R. D. Robinson, R. S. Ruoff, S. Salahuddin, J. Shan, L. Shi, M. G. Spencer, M. Terrones, W. Windl, and J. E. Goldberger. Progress, challenges, and opportunities in two-dimensional materials beyond graphene. *ACS Nano*, 7:2898, 2013.

[10] L. Britnell, R. V. Gorbachev, R. Jalil, B. D. Belle, F. Schedin, A. Mishchenko, T. Georgiou, M. I. Katsnelson, L. Eaves, S. V. Morozov, N. M. R. Peres, J. Leist, A. K. Geim, K. S. Novoselov, and L. A. Ponomarenko. Field-effect tunneling transistor based on vertical graphene heterostructures. *Science*, 335(6071):947–950, 2012.

[11] Liam Britnell, Roman V. Gorbachev, Rashid Jalil, Branson D. Belle, Fred Schedin, Mikhail I. Katsnelson, Laurence Eaves, Sergey V. Morozov, Alexander S. Mayorov, Nuno M. R. Peres, Antonio H. Castro Neto, Jon Leist, Andre K. Geim, Leonid A. Ponomarenko, and Kostya S. Novoselov. Electron tunneling through ultrathin boron nitride crystalline barriers. *Nano Letters*, 12(3):1707–1710, 2012.

[12] H. Tian, M. L. Chin, S. Najmaei, Q. S. Guo, F. N. Xia, H. Wang, and M. Dubey. Optoelectronic devices based on two-dimensional transition metal dichalcogenides. *Nano Res.*, 9: 1543–1560, 2016.

[13] M. Batmunkh, M. Bat-Erdene, and J. G. Shapter. Phosphorene and phosphorene-based materials - prospects for future applications. *Adv. Mater.*, 28(39):8586–8617, 2016.

[14] S. Balendhran, S. Walia, H. Nili, S. Sriram, and M. Bhaskaran. Elemental analogues of graphene: Silicene, germanene, stanene, and phosphorene. *Small*, 11(6):640–652, 2015.

[15] Han Liu, Adam T. Neal, Zhen Zhu, Zhe Luo, Xianfan Xu, David Tománek, and Peide D. Ye. Phosphorene: An unexplored 2d semiconductor with a high hole mobility. *ACS Nano*, 8(4):4033–4041, 2014.

[16] M. Freitag. Graphene: Trilayers unravelled. *Nat. Phys.*, 7:596–597, 2011.

[17] A. Splendiani, L. Sun, Y. Zhang, T. Li, J. Kim, C. Y. Chim, G. Galli, and F. Wang. Emerging photoluminescence in monolayer MoS_2. *Nano Lett.*, 10:1271–1275, 2010.

[18] K. F. Mak, C. Lee, J. Hone, J. Shan, and T. F. Heinz. Atomically thin MoS_2: A new direct-gap semiconductor. *Phys. Rev. Lett.*, 105:136805, 2010.

[19] L. K. Li, J. Kim, C. H. Jin, G. J. Ye, D. Y. Qiu, F. H. da Jornada, Z. W. Shi, L. Chen, Z. C. Zhang, F. Y. Yang, K. Watanabe, T. Taniguchi, W. Ren, S. G. Louie, X. H. Chen, Y. B. Zhang, and F. Wang. Direct observation of the layer-dependent electronic structure in phosphorene. *Nat. Nanotechnol.*, 12:21–25, 2017.

[20] Y. Zhang, T. Tang, C. Girit, Z. Hao, M. C. Martin, A. Zettl, M. F. Crommie, Y. R. Shen, and F. Wang. Direct observation of a widely tunable bandgap in bilayer graphene. *Nature*, 459: 820, 2009.

[21] Yi Zhang, Tay-Rong Chang, Bo Zhou, Yong-Tao Cui, Hao Yan, Zhongkai Liu, Felix Schmitt, James Lee, Rob Moore, Yulin Chen, Hsin Lin, Horng-Tay Jeng, Sung-Kwan Mo, Zahid Hussain, Arun Bansil, and Zhi-Xun Shen. Direct observation of the transition from indirect to direct bandgap in atomically thin epitaxial $MoSe_2$. *Nature Nanotechnology*, 9: 111, 2013.

[22] N. Kumar, S. Najmaei, Q. Cui, F. Ceballos, P. M. Ajayan, J. Lou, and H. Zhao. Second harmonic microscopy of monolayer MoS_2. *Phys. Rev. B*, 87:161403, 2013.

[23] Y. Li, Y. Rao, K. F. Mak, Y. You, S. Wang, C. R. Dean, and T. F. Heinz. Probing symmetry properties of few-layer MoS_2 and h-BN by optical second-harmonic generation. *Nano Lett.*, 13:3329–3333, 2013.

[24] D. Xiao, G. B. Liu, W. Feng, X. Xu, and W. Yao. Coupled spin and valley physics in monolayers of MoS_2 and other group-VI dichalcogenides. *Phys. Rev. Lett.*, 108:196802, 2012.

[25] H. Zeng, J. Dai, W. Yao, D. Xiao, and X. Cui. Valley polarization in MoS_2 monolayers by optical pumping. *Nat. Nanotechnol.*, 7:490–493, 2012.

[26] K. F. Mak, K. He, J. Shan, and T. F. Heinz. Control of valley polarization in monolayer MoS_2 by optical helicity. *Nat. Nanotechnol.*, 7:494–498, 2012.

[27] A. Chernikov, T. C. Berkelbach, H. M. Hill, A. Rigosi, Y. L. Li, O. B. Aslan, D. R. Reichman, M. S. Hybertsen, and T. F. Heinz. Exciton binding energy and nonhydrogenic Rydberg series in monolayer WS_2. *Phys. Rev. Lett.*, 113:076802, 2014.

[28] K. He, N. Kumar, L. Zhao, Z. Wang, K. F. Mak, H. Zhao, and J. Shan. Tightly bound excitons in monolayer WSe_2. *Phys. Rev. Lett.*, 113:026803, 2014.

[29] K. F. Mak, K. He, C. Lee, G. H. Lee, J. Hone, T. F. Heinz, and J. Shan. Tightly bound trion in monolayer MoS_2. *Nat. Mater.*, 12:207–211, 2013.

[30] Y. M. You, X. X. Zhang, T. C. Berkelbach, M. S. Hybertsen, D. R. Reichman, and T. F. Heinz. Observation of biexcitons in monolayer WSe_2. *Nat. Phys.*, 11:477–481, 2015.

[31] K. Hao, J. F. Specht, P. Nagler, L. Xu, K. Tran, A. Singh, C. K. Dass, C. Schüller, T. Korn, M. Richter, A. Knorr, X. Li, and G. Moody. Neutral and charged inter-valley biexcitons in monolayer $MoSe_2$. *Nat. Commun.*, 8:15552, 2017.

[32] Z. Nie, R. Long, L. Sun, C. C. Huang, J. Zhang, Q. Xiong, D. W. Hewak, Z. Shen, O. V. Prezhdo, and Z. H. Loh. Ultrafast carrier thermalization and cooling dynamics in few-layer MoS_2. *ACS Nano*, 8:10931–10940, 2014.

[33] F. Ceballos, Q. Cui, M. Z. Bellus, and H. Zhao. Exciton formation in monolayer transition metal dichalcogenides. *Nanoscale*, 8:11681–11688, 2016.

[34] P. Steinleitner, P. Merkl, P. Nagler, J. Mornhinweg, C. Schuller, T. Korn, A. Chernikov, and R. Huber. Direct observation of ultrafast exciton formation in a monolayer of WSe_2. *Nano Lett.*, 17:1455–1460, 2017.

[35] J. He, N. Kumar, M. Z. Bellus, H. Y. Chiu, D. He, Y. Wang, and H. Zhao. Electron transfer and coupling in graphene-tungsten disulfide van der Waals heterostructures. *Nat. Commun.*, 5:5622, 2014.

[36] A. Raja, A. Chaves, J. Yu, G. Arefe, H. M. Hill, A. F. Rigosi, T. C. Berkelbach, P. Nagler, C. Schuller, T. Korn, C. Nuckolls, J. Hone, L. E. Brus, T. F. Heinz, D. R. Reichman, and A. Chernikov. Coulomb engineering of the bandgap and excitons in two-dimensional materials. *Nat. Commun.*, 8:15251, 2017.

[37] S. Cui, H. Pu, S. A. Wells, Z. Wen, S. Mao, J. Chang, M. C. Hersam, and J. Chen. Ultrahigh sensitivity and layer-dependent sensing performance of phosphorene-based gas sensors. *Nat. Commun.*, 6:8632, 2015.

[38] S. Borghardt, J. Tu, F. Winkler, J. Schubert, W. Zander, K. Leosson, and B. E. Kardynał. Engineering of optical and electronic band gaps in transition metal dichalcogenide monolayers through external dielectric screening. *Physical Review Materials*, 1(5):054001, 2017.

[39] D. Akinwande, N. Petrone, and J. Hone. Two-dimensional flexible nanoelectronics. *Nat. Commun.*, 5:5678, 2014.

[40] T. Georgiou, R. Jalil, B. D. Belle, L. Britnell, R. V. Gorbachev, S. V. Morozov, Y. J. Kim, A. Gholinia, S. J. Haigh, O. Makarovsky, L. Eaves, L. A. Ponomarenko, A. K. Geim, K. S. Novoselov, and A. Mishchenko. Vertical field-effect transistor based on graphene-WS_2 heterostructures for flexible and transparent electronics. *Nat. Nanotechnol.*, 8:100–103, 2013.

[41] L. Britnell, R. M. Ribeiro, A. Eckmann, R. Jalil, B. D. Belle, A. Mishchenko, Y.-J. Kim, R. V. Gorbachev, T. Georgiou, S. V. Morozov, A. N. Grigorenko, A. K. Geim, C. Casiraghi, A. H. C. Neto, and K. S. Novoselov. Strong light-matter interactions in heterostructures of atomically thin films. *Science*, 340:1311–1314, 2013.

[42] H.-L. Liu, C.-C. Shen, S.-H. Su, C.-L. Hsu, M.-Y. Li, and L.-J. Li. Optical properties of monolayer transition metal dichalcogenides probed by spectroscopic ellipsometry. *Appl. Phys. Lett.*, 105:201905, 2014.

[43] M. Bernardi, M. Palummo, and J. C. Grossman. Extraordinary sunlight absorption and one nanometer thick photovoltaics using two-dimensional monolayer materials. *Nano Lett.*, 13 (8):3664–3670, 2013.

[44] L. Y. Yang, N. A. Sinitsyn, W. B. Chen, J. T. Yuan, J. Zhang, J. Lou, and S. A. Crooker. Long-lived nanosecond spin relaxation and spin coherence of electrons in monolayer MoS_2 and WS_2. *Nat. Phys.*, 11:830–834, 2015.

[45] B. Radisavljevic, A. Radenovic, J. Brivio, V. Giacometti, and A. Kis. Single-layer MoS_2 transistors. *Nat. Nanotechnol.*, 6:147–150, 2011.

[46] B. Radisavljevic and A. Kis. Mobility engineering and a metal-insulator transition in monolayer MoS_2. *Nat. Mater.*, 12:815–820, 2013.

[47] B. Radisavljevic, M. B. Whitwick, and A. Kis. Integrated circuits and logic operations based on single-layer MoS_2. *ACS Nano*, 5:9934–9938, 2011.

[48] H. Wang, L. L. Yu, Y. H. Lee, Y. M. Shi, A. Hsu, M. L. Chin, L. J. Li, M. Dubey, J. Kong, and T. Palacios. Integrated circuits based on bilayer MoS_2 transistors. *Nano Lett.*, 12: 4674–4680, 2012.

[49] B. W. H. Baugher, H. O. H. Churchill, Y. Yang, and P. Jarillo-Herrero. Optoelectronic devices based on electrically tunable p-n diodes in a monolayer dichalcogenide. *Nat. Nanotechnol.*, 9:262–267, 2014.

[50] Y. J. Zhang, T. Oka, R. Suzuki, J. T. Ye, and Y. Iwasa. Electrically switchable chiral light-emitting transistor. *Science*, 344:725–728, 2014.

[51] J. S. Ross, P. Klement, A. M. Jones, N. J. Ghimire, J. Yan, D. G. Mandrus, T. Taniguchi, K. Watanabe, K. Kitamura, W. Yao, D. H. Cobden, and X. Xu. Electrically tunable excitonic light-emitting diodes based on monolayer WSe_2 p-n junctions. *Nat. Nanotechnol.*, 9:268–274, 2014.

[52] A. Pospischil, M. M. Furchi, and T. Mueller. Solar-energy conversion and light emission in an atomic monolayer p-n diode. *Nat. Nanotechnol.*, 9:257–261, 2014.

[53] A. K. Geim and I. V. Grigorieva. Van der waals heterostructures. *Nature*, 499:419–425, 2013.

[54] Y. Liu, N. O. Weiss, X. Duan, H.-C. Cheng, Y. Huang, and X. Duan. van der Waals heterostructures and devices. *Nat. Rev. Mater.*, 1:16042, 2016.

[55] K. S. Novoselov, A. Mishchenko, A. Carvalho, and A. H. C. Neto. 2D materials and van der Waals heterostructures. *Science*, 353:461, 2016.

[56] L. A. Ponomarenko, R. V. Gorbachev, G. L. Yu, D. C. Elias, R. Jalil, A. A. Patel, A. Mishchenko, A. S. Mayorov, C. R. Woods, J. R. Wallbank, M. Mucha-Kruczynski, B. A. Piot, M. Potemski, I. V. Grigorieva, K. S. Novoselov, F. Guinea, V. I. Fal'ko, and A. K. Geim. Cloning of dirac fermions in graphene superlattices. *Nature*, 497:594, 2013.

[57] G. Li, A. Luican, J. M. B. Lopes dos Santos, A. H. Castro Neto, A. Reina, J. Kong, and E. Y. Andrei. Observation of van hove singularities in twisted graphene layers. *Nature Physics*, 6:109, 2009.

[58] M. Yankowitz, J. Xue, D. Cormode, J. D. Sanchez-Yamagishi, K. Watanabe, T. Taniguchi, P. Jarillo-Herrero, P. Jacquod, and B. J. LeRoy. Emergence of superlattice dirac points in graphene on hexagonal boron nitride. *Nature Physics*, 8:382, 2012.

[59] S. V. Morozov, K. S. Novoselov, M. I. Katsnelson, F. Schedin, D. C. Elias, J. A. Jaszczak,

and A. K. Geim. Giant intrinsic carrier mobilities in graphene and its bilayer. *Phys. Rev. Lett.*, 100:016602, 2008.

[60] Y. Liu, H. Wu, H. C. Cheng, S. Yang, E. B. Zhu, Q. Y. He, M. N. Ding, D. H. Li, J. Guo, N. O. Weiss, Y. Huang, and X. F. Duan. Toward barrier free contact to molybdenum disulfide using graphene electrodes. *Nano Lett.*, 15:3030–3034, 2015.

[61] D. Qu, X. Liu, F. Ahmed, D. Lee, and W. J. Yoo. Self-screened high performance multi-layer MoS_2 transistor formed by using a bottom graphene electrode. *Nanoscale*, 7:19273–19281, 2015.

[62] W. J. Yu, Y. Liu, H. Zhou, A. Yin, Z. Li, Y. Huang, and X. Duan. Highly efficient gate-tunable photocurrent generation in vertical heterostructures of layered materials. *Nat. Nanotechnol.*, 8:952–958, 2013.

[63] D. De Fazio, I. Goykhman, D. Yoon, M. Bruna, A. Eiden, S. Milana, U. Sassi, M. Barbone, D. Dumcenco, K. Marinov, A. Kis, and A. C. Ferrari. High responsivity, large-area Graphene/MoS_2 flexible photodetectors. *ACS Nano*, 10:8252–8262, 2016.

[64] W. J. Yu, Q. A. Vu, H. Oh, H. G. Nam, H. L. Zhou, S. Cha, J. Y. Kim, A. Carvalho, M. Jeong, H. Choi, A. H. C. Neto, Y. H. Lee, and X. F. Duan. Unusually efficient photocurrent extraction in monolayer van der Waals heterostructure by tunnelling through discretized barriers. *Nat. Commun.*, 7:13278, 2016.

[65] W. J. Yu, Z. Li, H. L. Zhou, Y. Chen, Y. Wang, Y. Huang, and X. F. Duan. Vertically stacked multi-heterostructures of layered materials for logic transistors and complementary inverters. *Nat. Mater.*, 12:246–252, 2013.

[66] L. Britnell, R. V. Gorbachev, R. Jalil, B. D. Belle, F. Schedin, A. Mishchenko, T. Georgiou, M. I. Katsnelson, L. Eaves, S. V. Morozov, N. M. R. Peres, J. Leist, A. K. Geim, K. S. Novoselov, and L. A. Ponomarenko. Field-effect tunneling transistor based on vertical graphene heterostructures. *Science*, 335:947–950, 2012.

[67] C. J. Shih, Q. H. Wang, Y. Son, Z. Jin, D. Blankschtein, and M. S. Strano. Tuning on-off current ratio and field-effect mobility in a MoS_2-graphene heterostructure via Schottky barrier modulation. *ACS Nano*, 8:5790–5798, 2014.

[68] J. Y. Kwak, J. Hwang, B. Calderon, H. Alsalman, N. Munoz, B. Schutter, and M. G. Spencer. Electrical characteristics of multilayer MoS_2 FET's with MoS_2/graphene heterojunction contacts. *Nano Lett.*, 14:4511–4516, 2014.

[69] K. Roy, M. Padmanabhan, S. Goswami, T. P. Sai, G. Ramalingam, S. Raghavan, and A. Ghosh. Graphene-MoS_2 hybrid structures for multifunctional photoresponsive memory devices. *Nat. Nanotechnol.*, 8:826–830, 2013.

[70] Y. Sata, R. Moriya, S. Morikawa, N. Yabuki, S. Masubuchi, and T. Machida. Electric field modulation of schottky barrier height in graphene/MoS_2 van der Waals heterointerface. *Appl. Phys. Lett.*, 107:023109, 2015.

[71] M. V. Zhao, Y. Ye, Y. M. Han, Y. Xia, H. Y. Zhu, S. Q. Wang, Y. Wang, D. A. Muller, and X. Zhang. Large-scale chemical assembly of atomically thin transistors and circuits. *Nat. Nanotechnol.*, 11:954–959, 2016.

[72] D. McManus, S. Vranic, F. Withers, V. Sanchez-Romaguera, M. Macucci, H. F. Yang, R. Sorrentino, K. Parvez, S. K. Son, G. Iannaccone, K. Kostarelos, G. Fiori, and C. Casiraghi. Water-based and biocompatible 2D crystal inks for all-inkjet-printed heterostructures. *Nat. Nanotechnol.*, 12:343–350, 2017.

[73] X. Chen, Y. J. Park, T. Das, H. Jang, J. B. Lee, and J. H. Ahn. Lithography-free plasma-induced patterned growth of MoS_2 and its heterojunction with graphene. *Nanoscale*, 8: 15181–15188, 2016.

[74] M. H. Chiu, C. D. Zhang, H. W. Shiu, C. P. Chuu, C. H. Chen, C. Y. S. Chang, C. H. Chen, M. Y. Chou, C. K. Shih, and L. J. Li. Determination of band alignment in the single-layer MoS_2/WSe_2 heterojunction. *Nat.Commun.*, 6:7666, 2015.

[75] H. Fang, C. Battaglia, C. Carraro, S. Nemsak, B. Ozdol, J. S. Kang, H. A. Bechtel, S. B. Desai, F. Kronast, A. A. Unal, G. Conti, C. Conlon, G. K. Palsson, M. C. Martin, A. M. Minor, C. S. Fadley, E. Yablonovitch, R. Maboudian, and A. Javey. Strong interlayer coupling in van der Waals heterostructures built from single-layer chalcogenides. *Proc. Natl. Acad. Sci. U. S. A.*, 111:6198–6202, 2014.

[76] S. Latini, K. T. Winther, T. Olsen, and K. S. Thygesen. Interlayer excitons and band alignment in MoS_2/hBN/WSe_2 van der Waals heterostructures. *Nano Lett.*, 17:938–945, 2017.

[77] H. M. Hill, A. F. Rigosi, K. T. Rim, G. W. Flynn, and T. F. Heinz. Band alignment in MoS_2/WS_2 transition metal dichalcogenide heterostructures probed by scanning tunneling microscopy and spectroscopy. *Nano Lett.*, 16:4831–4837, 2016.

[78] X. Hong, J. Kim, S. F. Shi, Y. Zhang, C. Jin, Y. Sun, S. Tongay, J. Wu, Y. Zhang, and F. Wang. Ultrafast charge transfer in atomically thin MoS_2/WS_2 heterostructures. *Nat. Nanotechnol.*, 9:682–686, 2014.

[79] F. Ceballos, M. Z. Bellus, H. Y. Chiu, and H. Zhao. Ultrafast charge separation and indirect exciton formation in a MoS_2-$MoSe_2$ van der waals heterostructure. *ACS Nano*, 8:12717–12724, 2014.

[80] P. Rivera, J. R. Schaibley, A. M. Jones, J. S. Ross, S. Wu, G. Aivazian, P. Klement, K. Seyler, G. Clark, N. J. Ghimire, J. Yan, D. G. Mandrus, W. Yao, and X. Xu. Observation of long-lived interlayer excitons in monolayer $MoSe_2$-WSe_2 heterostructures. *Nat. Commun.*, 6: 6242, 2015.

[81] B. Miller, A. Steinhoff, B. Pano, J. Klein, F. Jahnke, A. Holleitner, and U. Wurstbauer. Long-lived direct and indirect interlayer excitons in van der Waals heterostructures. *Nano Lett.*, 17:5229–5237, 2017.

[82] C. H. Lee, G. H. Lee, A. M. van der Zande, W. Chen, Y. Li, M. Han, X. Cui, G. Arefe,

C. Nuckolls, T. F. Heinz, J. Guo, J. Hone, and P. Kim. Atomically thin p-n junctions with van der Waals heterointerfaces. *Nat. Nanotechnol.*, 9:676–681, 2014.

[83] J. S. Ross, P. Rivera, J. Schaibley, E. Lee-Wong, H. Y. Yu, T. Taniguchi, K. Watanabe, J. Q. Yan, D. Mandrus, D. Cobden, W. Yao, and X. D. Xu. Interlayer exciton optoelectronics in a 2D heterostructure p-n junction. *Nano Lett.*, 17:638–643, 2017.

[84] P. Rivera, K. L. Seyler, H. Y. Yu, J. R. Schaibley, J. Q. Yan, D. G. Mandrus, W. Yao, and X. D. Xu. Valley-polarized exciton dynamics in a 2D semiconductor heterostructure. *Science*, 351:688–691, 2016.

[85] J. R. Schaibley, P. Rivera, H. Y. Yu, K. L. Seyler, J. Q. Yan, D. G. Mandrus, T. Taniguchi, K. Watanabe, W. Yao, and X. D. Xu. Directional interlayer spin-valley transfer in two-dimensional heterostructures. *Nat. Commun.*, 7:13747.

[86] J. Kim, C. H. Jin, B. Chen, H. Cai, T. Zhao, P. Lee, S. Kahn, K. Watanabe, T. Taniguchi, S. Tongay, M. F. Crommie, and F. Wang. Observation of ultralong valley lifetime in WSe_2/MoS_2 heterostructures. *Sci. Adv.*, 3:e1700518, 2017.

[87] W. G. Xu, W. W. Liu, J. F. Schmidt, W. J. Zhao, X. Lu, T. Raab, C. Diederichs, W. B. Gao, D. V. Seletskiy, and Q. H. Xiong. Correlated fluorescence blinking in two-dimensional semiconductor heterostructures. *Nature*, 541:62, 2017.

[88] M. M. Furchi, A. Pospischil, F. Libisch, J. Burgdorfer, and T. Mueller. Photovoltaic effect in an electrically tunable van der Waals heterojunction. *Nano Lett.*, 14:4785–4791, 2014.

[89] R. Cheng, D. Li, H. Zhou, C. Wang, A. Yin, S. Jiang, Y. Liu, Y. Chen, Y. Huang, and X. Duan. Electroluminescence and photocurrent generation from atomically sharp WSe_2/MoS_2 heterojunction p-n diodes. *Nano Lett.*, 14:5590–5597, 2014.

[90] K. Chen, X. Wan, J. X. Wen, W. G. Xie, Z. W. Kang, X. L. Zeng, H. J. Chen, and J. B.

Xu. Electronic properties of MoS_2–WS_2 heterostructures synthesized with two-step lateral epitaxial strategy. *ACS Nano*, 9(10):9868–9876, 2015.

[91] Y. Gong, S. Lei, G. Ye, B. Li, Y. He, K. Keyshar, X. Zhang, Q. Wang, J. Lou, Z. Liu, R. Vajtai, W. Zhou, and P. M. Ajayan. Two-step growth of two-dimensional WSe_2/$MoSe_2$ heterostructures. *Nano Letters*, 15(9):6135–6141, 2015.

[92] Jason S. Ross, Philip Klement, Aaron M. Jones, Nirmal J. Ghimire, Jiaqiang Yan, D. G. Mandrus, Takashi Taniguchi, Kenji Watanabe, Kenji Kitamura, Wang Yao, David H. Cobden, and Xiaodong Xu. Electrically tunable excitonic light-emitting diodes based on monolayer WSe_2 p–n junctions. *Nature Nanotechnology*, 9:268, 2014.

[93] A. Pospischil, M. M. Furchi, and T. Mueller. Solar-energy conversion and light emission in an atomic monolayer p–n diode. *Nature Nanotechnology*, 9:257, 2014.

[94] B. W. H. Baugher, H. O. H. Churchill, Y. Yang, and P. Jarillo-Herrero. Optoelectronic devices based on electrically tunable p–n diodes in a monolayer dichalcogenide. *Nature Nanotechnology*, 9:262, 2014.

[95] M. S. Choi, D. Qu, D. Lee, X. Liu, K. Watanabe, T. Taniguchi, and W. J. Yoo. Lateral MoS_2 p–n junction formed by chemical doping for use in high-performance optoelectronics. *ACS Nano*, 8(9):9332–9340, 2014.

[96] C. Zhang, Y. Chen, J. Huang, X. Wu, L. Li, W. Yao, J. Tersoff, and C. Shih. Visualizing band offsets and edge states in bilayer–monolayer transition metal dichalcogenides lateral heterojunction. *Nature Communications*, 7:10349, 2016.

[97] H. Kwon, K. Lee, J. Heo, Y. Oh, H. Lee, S. Appalakondaiah, W. Ko, H. W. Kim, J. Jung, H. Suh, H. Min, I. Jeon, E. Hwang, and S. Hwang. Characterization of edge contact: Atomically resolved semiconductor–metal lateral boundary in MoS_2. *Advanced Materials*, 29 (41):1702931, 2017.

[98] F. J. M. Hoeben, P. Jonkheijm, E. W. Meijer, and A. Schenning. About supramolecular assemblies of pi-conjugated systems. *Chem. Rev.*, 105:1491–1546, 2005.

[99] D. L. Dexter. A theory of sensitized luminescence in solids. *J. Chem. Phys.*, 21:836–850, 1953.

[100] C. B. Murphy, Y. Zhang, T. Troxler, V. Ferry, J. J. Martin, and W. E. Jones. Probing förster and dexter energy-transfer mechanisms in fluorescent conjugated polymer chemosensors. *J. Phys. Chem. B*, 108:1537–1543, 2004.

[101] F. Ceballos, M. Z. Bellus, H. Y. Chiu, and H. Zhao. Probing charge transfer excitons in a $MoSe_2$-WS_2 van der Waals heterostructure. *Nanoscale*, 7:17523–17528, 2015.

[102] B. Peng, G. Yu, X. Liu, B. Liu, X. Liang, L. Bi, L. Deng, T. C. Sum, and K. P. Loh. Ultrafast charge transfer in MoS_2/WSe_2 p-n heterojunction. *2D Mater.*, 3:025020, 2016.

[103] H. M. Zhu, J. Wang, Z. Z. Gong, Y. D. Kim, J. Hone, and X. Y. Zhu. Interfacial charge transfer circumventing momentum mismatch at two-dimensional van der waals heterojunctions. *Nano Lett.*, 17:3591–3598, 2017.

[104] A. F. Rigos, H. M. Hill, Y. L. Li, A. Chernikov, and T. F. Heinz. Probing interlayer interactions in transition metal dichalcogenide heterostructures by optical spectroscopy: MoS_2/WS_2 and $MoSe_2$/WSe_2. *Nano Lett.*, 15:5033–5038, 2015.

[105] D. Kozawa, A. Carvalho, I. Verzhbitskiy, F. Giustiniano, Y. Miyauchi, S. Mouri, A. H. C. Neto, K. Matsuda, and G. Eda. Evidence for fast interlayer energy transfer in $MoSe_2$/WS_2 heterostructures. *Nano Lett.*, 16:4087–4093, 2016.

[106] X. Zhu, N. R. Monahan, Z. Gong, H. Zhu, K. W. Williams, and C. A. Nelson. Charge transfer excitons at van der Waals interfaces. *J. Am. Chem. Soc.*, 137:8313–8320, 2015.

[107] R. Long and O. V. Prezhdo. Quantum coherence facilitates efficient charge separation at a MoS_2/$MoSe_2$ van der Waals junction. *Nano Lett.*, 16:1996–2003, 2016.

[108] H. Wang, J. Bang, Y. Y. Sun, L. B. Liang, D. West, V. Meunier, and S. B. Zhang. The role of collective motion in the ultrafast charge transfer in van der Waals heterostructures. *Nat. Commun.*, 7:11504, 2016.

[109] Y. Wang, Z. Wang, W. Yao, G. B. Liu, and H. Y. Yu. Interlayer coupling in commensurate and incommensurate bilayer structures of transition-metal dichalcogenides. *Phys. Rev. B*, 95:115429, 2017.

[110] Charles Kittel. *Introduction to Solid State Physics*. John Wiley & Sons, Inc., 8th edition, 2005.

[111] I. G. Lezama, A. Arora, A. Ubaldini, C. Barreteau, E. Giannini, M. Potemski, and A. F. Morpurgo. Indirect-to-direct band gap crossover in few-layer $MoTe_2$. *Nano Lett.*, 15:2336–2342, 2015.

[112] F. Ceballos and H. Zhao. Ultrafast laser spectroscopy of two-dimensional materials beyond graphene. *Adv. Funct. Mater.*, 27:1604509, 2017.

[113] E. W Weisstein. Convolution, 2018. URL `http://mathworld.wolfram.com/Convolution.html`.

[114] J. He, D. He, Y. Wang, Q. Cui, F. Ceballos, and H. Zhao. Spatiotemporal dynamics of excitons in monolayer and bulk ws_2. *Nanoscale*, 7:9526, 2015.

[115] H. Zhao, B. Dal Don, S. Moehl, H. Kalt, K. Ohkawa, and D. Hommel. Spatio-temporal dynamics of quantum-well excitons. *Phys. Rev. B*, 67:035306, 2003.

[116] A. A. Mitioglu, P. Plochocka, J. N. Jadczak, W. Escoffier, G. Rikken, L. Kulyuk, and D. K. Maude. Optical manipulation of the exciton charge state in single-layer tungsten disulfide. *Phys. Rev. B*, 88:245403, 2013.

[117] Y. Li, Z. Qi, M. Liu, Y. Wang, X. Cheng, G. Zhang, and L. Sheng. Photoluminescence of monolayer MoS_2 on $LaAlO_3$ and $SrTiO_3$ substrates. *Nanoscale*, 6:15248–15254, 2014.

[118] J. D. Lin, C. Han, F. Wang, R. Wang, D. Xiang, S. Qin, X. A. Zhang, L. Wang, H. Zhang, A. T. Wee, and W. Chen. Electron-doping-enhanced trion formation in monolayer molybdenum disulfide functionalized with cesium carbonate. *ACS Nano*, 8:5323–5329, 2014.

[119] M. Z. Bellus, F. Ceballos, H.-Y. Chiu, and H. Zhao. Tightly bound trions in transition metal dichalcogenide heterostructures. *ACS Nano*, 9:6459–6464, 2015.

[120] J. S. Ross, S. Wu, H. Yu, N. J. Ghimire, A. M. Jones, G. Aivazian, J. Yan, D. G. Mandrus, D. Xiao, W. Yao, and X. Xu. Electrical control of neutral and charged excitons in a monolayer semiconductor. *Nat. Commun.*, 4:1474, 2013.

[121] Z. Ye, T. Cao, K. O'Brien, H. Zhu, X. Yin, Y. Wang, S. G. Louie, and X. Zhang. Probing excitonic dark states in single-layer tungsten disulphide. *Nature*, 513:214–218, 2014.

[122] B. Zhu, H. Zeng, J. Dai, Z. Gong, and X. Cui. Anomalously robust valley polarization and valley coherence in bilayer WS_2. *Proc. Nat. Acad. Sci. USA*, 111:11606–11611, 2014.

[123] P. Tonndorf, R. Schmidt, P. Bottger, X. Zhang, J. Borner, A. Liebig, M. Albrecht, C. Kloc, O. Gordan, D. R. T. Zahn, S. M. de Vasconcellos, and R. Bratschitsch. Photoluminescence emission and Raman response of monolayer MoS_2, $MoSe_2$, and WSe_2. *Opt. Express*, 21: 4908, 2013.

[124] W. J. Zhao, Z. Ghorannevis, L. Q. Chu, M. L. Toh, C. Kloc, P. H. Tan, and G. Eda. Evolution of electronic structure in atomically thin sheets of WS_2 and WSe_2. *ACS Nano*, 7:791–797, 2013.

[125] N. Peimyoo, J. Z. Shang, C. X. Cong, X. N. Shen, X. Y. Wu, E. K. L. Yeow, and T. Yu. Nonblinking, intense two-dimensional light emitter: Mono layer WS_2 triangles. *ACS Nano*, 7:10985–10994, 2013.

[126] C. Gong, H. J. Zhang, W. H. Wang, L. Colombo, R. M. Wallace, and K. J. Cho. Band

alignment of two-dimensional transition metal dichalcogenides: Application in tunnel field effect transistors. *Appl. Phys. Lett.*, 103:053513, 2013.

[127] T. Schmidt, K. Lischka, and W. Zulehner. Excitation-power dependence of the near-band-edge photoluminescence of semiconductors. *Phy. Rev. B*, 45:8989–8994, 1992.

[128] F. Vietmeyer, P. A. Frantsuzov, B. Janko, and M. Kuno. Carrier recombination dynamics in individual CdSe nanowires. *Phys. Rev. B*, 83:115319, 2011.

[129] Michael A. Reshchikov, Anita J. Olsen, Marilyn F. Bishop, and Tom McMullen. Superlinear increase of photoluminescence with excitation intensity in zn-doped GaN. *Phys. Rev. B*, 88: 075204, 2013.

[130] B. Chen, H. Sahin, A. Suslu, L. Ding, M. I. Bertoni, F. M. Peeters, and S. Tongay. Environmental changes in $MoTe_2$ excitonic dynamics by defects-activated molecular interaction. *ACS Nano*, 9:5326–5332, 2015.

[131] T. Yan, X. Qiao, X. Liu, P. Tan, and X. Zhang. Photoluminescence properties and exciton dynamics in monolayer WSe_2. *Appl. Phys. Lett.*, 105:101901, 2014.

[132] F. Ceballos, P. Zereshki, and H. Zhao. Separating electrons and holes by monolayer increments in van der waals heterostructures. *Phys. Rev. Mater.*, 1:044001, 2017.

[133] F. Ceballos, M. Z. Bellus, H. Y. Chiu, and H. Zhao. Charge separation and indirect exciton formation in a mos_2-$mose_2$ van der waals heterostructure. *ACS Nano*, page 10.1021/nn505736z, 2014.

[134] S. Pan, F. Ceballos, M. Z. Bellus, and H. Zhao. Ultrafast charge transfer between $MoTe_2$ and MoS_2 monolayers. *2D Mater.*, 4:015033, 2017.

[135] M. Z. Bellus, M. Li, S. Lane, F. Ceballos, Q. Cui, X. C. Zeng, and H. Zhao. Type-I van der Waals heterostructure formed by MoS_2 and ReS_2 monolayers. *Nanoscale Horiz.*, 2:31–36, 2016.

[136] A Castellanos-Gomez, N. Agraït, and G Rubio-Bollinger. Optical identification of atomically thin dichalcogenide crystals. *Appl. Phys. Lett.*, 96:213116, 2010.

[137] M. M. Benameur, B. Radisavljevic, J. S. Héron, S. Sahoo, H. Berger, and A. Kis. Visibility of dichalcogenide nanolayers. *Nanotechnology*, 22:125706, 2011.

[138] O. B. Aslan, D. A. Chenet, A. M. van der Zande, J. C. Hone, and T. F. Heinz. Linearly polarized excitons in single- and few-layer ReS_2 crystals. *ACS Photon.*, 3:96–101, 2016.

[139] H. Li, Q. Zhang, C. C. R. Yap, B. K. Tay, T. H. T. Edwin, A. Olivier, and D. Baillargeat. From bulk to monolayer MoS_2: Evolution of raman scattering. *Adv. Funct. Mater.*, 22: 1385–1390, 2012.

[140] Y. Li, Q. Cui, F. Ceballos, S. D. Lane, Z. Qi, and H. Zhao. Ultrafast interlayer electron transfer in incommensurate transition metal dichalcogenide homobilayers. *Nano Letters*, 17 (11):6661–6666, 2017.

[141] A. Shah, P. Torres, R. Tscharner, N. Wyrsch, and H. Keppner. Photovoltaic technology: The case for thin-film solar cells. *Science*, 285:692–698, 1999.

[142] P. G. Lecomber, W. E. Spear, and A. Ghaith. Amorphous-silicon field-effect device and possible application. *Electron. Lett.*, 15:179–181, 1979.

[143] K. Nomura, H. Ohta, A. Takagi, T. Kamiya, M. Hirano, and H. Hosono. Room-temperature fabrication of transparent flexible thin-film transistors using amorphous oxide semiconductors. *Nature*, 432:488–492, 2004.

[144] Y. Idota, T. Kubota, A. Matsufuji, Y. Maekawa, and T. Miyasaka. Tin-based amorphous oxide: A high-capacity lithium-ion-storage material. *Science*, 276:1395–1397, 1997.

[145] K. S. Suslick, S. B. Choe, A. A. Cichowlas, and M. W. Grinstaff. Sonochemical synthesis of amorphous iron. *Nature*, 353:414–416, 1991.

[146] R. D. L. Smith, M. S. Prevot, R. D. Fagan, Z. P. Zhang, P. A. Sedach, M. K. J. Siu, S. Trudel, and C. P. Berlinguette. Photochemical route for accessing amorphous metal oxide materials for water oxidation catalysis. *Science*, 340:60–63, 2013.

[147] H. Liu, A. T. Neal, Z. Zhu, Z. Luo, X. Xu, D. Tomanek, and P. D. Ye. Phosphorene: An unexplored 2D semiconductor with a high hole mobility. *ACS Nano*, 8:4033–4041, 2014.

[148] L. Li, Y. Yu, G. J. Ye, Q. Ge, X. Ou, H. Wu, D. Feng, X. H. Chen, and Y. Zhang. Black phosphorus field-effect transistors. *Nat. Nanotechnol.*, 9:372–377, 2014.

[149] J. Qiao, X. Kong, Z. X. Hu, F. Yang, and W. Ji. High-mobility transport anisotropy and linear dichroism in few-layer black phosphorus. *Nat. Commun.*, 5:4475, 2014.

[150] Y. Du, H. Liu, Y. Deng, and P. D. Ye. Device perspective for black phosphorus field-effect transistors: Contact resistance, ambipolar behavior, and scaling. *ACS Nano*, 8:10035–10042, 2014.

[151] F. Xia, H. Wang, and Y. Jia. Rediscovering black phosphorus as an anisotropic layered material for optoelectronics and electronics. *Nat. Commun.*, 5:4458, 2014.

[152] H. Liu, A. T. Neal, M. W. Si, Y. C. Du, and P. D. Ye. The effect of dielectric capping on few-layer phosphorene transistors: Tuning the Schottky barrier heights. *IEEE Electr. Dev. Lett.*, 35:795–797, 2014.

[153] S. Das, M. Demarteau, and A. Roelofs. Ambipolar phosphorene field effect transistor. *ACS Nano*, 8:11730–11738, 2014.

[154] J. Na, Y. T. Lee, J. A. Lim, K. Hwang do, G. T. Kim, W. K. Choi, and Y. W. Song. Few-layer black phosphorus field-effect transistors with reduced current fluctuation. *ACS Nano*, 8:11753–11762, 2014.

[155] J. D. Wood, S. A. Wells, D. Jariwala, K. S. Chen, E. Cho, V. K. Sangwan, X. Liu, L. J.

Lauhon, T. J. Marks, and M. C. Hersam. Effective passivation of exfoliated black phosphorus transistors against ambient degradation. *Nano Lett.*, 14:6964–6970, 2014.

[156] J. He, D. He, Y. Wang, Q. Cui, M. Z. Bellus, H.-Y. Chiu, and H. Zhao. Exceptional and anisotropic transport properties of photocarriers in black phosphorus. *ACS Nano*, 9:6436–6442, 2015.

[157] A. Favron, E. Gaufres, F. Fossard, A. L. Phaneuf-L'Heureux, N. Y. Tang, P. L. Levesque, A. Loiseau, R. Leonelli, S. Francoeur, and R. Martel. Photooxidation and quantum confinement effects in exfoliated black phosphorus. *Nat. Mater.*, 14:826–832, 2015.

[158] L. K. Li, F. Y. Yang, G. J. Ye, Z. C. Zhang, Z. W. Zhu, W. K. Lou, X. Y. Zhou, L. Li, K. Watanabe, T. Taniguchi, K. Chang, Y. Y. Wang, X. H. Chen, and Y. B. Zhang. Quantum hall effect in black phosphorus two-dimensional electron system. *Nat. Nanotechnol.*, 11: 592–596, 2016.

[159] S. Das, W. Zhang, M. Demarteau, A. Hoffmann, M. Dubey, and A. Roelofs. Tunable transport gap in phosphorene. *Nano Lett.*, 14:5733–5739, 2014.

[160] L. Liang, J. Wang, W. Lin, B. G. Sumpter, V. Meunier, and M. Pan. Electronic bandgap and edge reconstruction in phosphorene materials. *Nano Lett.*, 14:6400–6406, 2014.

[161] S. Zhang, J. Yang, R. Xu, F. Wang, W. Li, M. Ghufran, Y. W. Zhang, Z. Yu, G. Zhang, Q. Qin, and Y. Lu. Extraordinary photoluminescence and strong temperature/angle-dependent Raman responses in few-layer phosphorene. *ACS Nano*, 8:9590–9596, 2014.

[162] X. M. Wang, A. M. Jones, K. L. Seyler, V. Tran, Y. C. Jia, H. Zhao, H. Wang, L. Yang, X. D. Xu, and F. N. Xia. Highly anisotropic and robust excitons in monolayer black phosphorus. *Nat. Nanotechnol.*, 10:517–521, 2015.

[163] Z. Yang, J. Hao, S. Yuan, S. Lin, H. M. Yau, J. Dai, and S. P. Lau. Field-effect transis-

tors based on amorphous black phosphorus ultrathin films by pulsed laser deposition. *Adv. Mater.*, 27:3748–3754, 2015.

[164] M. Z. Bulles, Z. B. Yang, J. H. Hao, S. P. Lau, and H. Zhao. Amorphous two-dimensional black phosphorus with exceptional photocarrier transport properties. *2D Mater.*, 4:025063, 2017.

[165] D. Sun, Z. K. Wu, C. Divin, X. B. Li, C. Berger, W. A. de Heer, P. N. First, and T. B. Norris. Ultrafast relaxation of excited Dirac fermions in epitaxial graphene using optical differential transmission spectroscopy. *Phys. Rev. Lett.*, 101:157402, 2008.

[166] B. A. Ruzicka, N. Kumar, S. Wang, K. P. Loh, and H. Zhao. Two-probe study of hot carriers in reduced graphene oxide. *J. Appl. Phys.*, 109:084322, 2011.

[167] H. Zhao, S. Moehl, S. Wachter, and H. Kalt. Hot exciton transport in ZnSe quantum wells. *Appl. Phys. Lett.*, 80:1391, 2002.

[168] A. Thilagam. Exciton formation assisted by longitudinal optical phonons in monolayer transition metal dichalcogenides. *J. Appl. Phys.*, 120:124306, 2016.

[169] N. Kumar, Q. Cui, F. Ceballos, D. He, Y. Wang, and H. Zhao. Exciton-exciton annihilation in $MoSe_2$ monolayers. *Phys. Rev. B*, 89:125427, 2014.

[170] D. Sun, Y. Rao, G. A. Reider, G. Chen, Y. You, L. Brezin, A. R. Harutyunyan, and T. F. Heinz. Observation of rapid exciton-exciton annihilation in monolayer molybdenum disulfide. *Nano Lett.*, 14:5625–5629, 2014.

[171] L. Yuan and L. B. Huang. Exciton dynamics and annihilation in WS_2 2d semiconductors. *Nanoscale*, 7:7402–7408, 2015.

[172] C. Poellmann, P. Steinleitner, U. Leierseder, P. Nagler, G. Plechinger, M. Porer, R. Bratschitsch, C. Schuller, T. Korn, and R. Huber. Resonant internal quantum transitions and

femtosecond radiative decay of excitons in monolayer WSe_2. *Nat. Mater.*, 14:889–893, 2015.

[173] A. C. Ferrari, J. C. Meyer, V. Scardaci, C. Casiraghi, M. Lazzeri, F. Mauri, S. Piscanec, D. Jiang, K. S. Novoselov, S. Roth, and A. K. Geim. Raman spectrum of graphene and graphene layers. *Phys. Rev. Lett.*, 97:187401, 2006.

[174] Q. Gu, E. A. Schiff, S. Grebner, F. Wang, and R. Schwarz. Non-gaussian transport measurements and the einstein relation in amorphous silicon. *Phys. Rev. Lett.*, 76:3196–3199, 1996.

[175] U. Haken, M. Hundhausen, and L. Ley. Analysis of the moving-photocarrier-grating technique for the determination of mobility and lifetime of photocarriers in semiconductors. *Phys. Rev. B*, 51:10579–10590, 1995.

[176] F. Wang and R. Schwarz. Electrically detected transient photocarrier grating method. *Appl. Phys. Lett.*, 65:884–886, 1994.

[177] Y. Cai, G. Zhang, and Y. W. Zhang. Layer-dependent band alignment and work function of few-layer phosphorene. *Sci. Rep.*, 4:6677, 2014.

[178] A. Boulesbaa, B. Huang, K. Wang, M. W. Lin, M. Mahjouri-Samani, C. Rouleau, K. Xiao, M. Yoon, B. Sumpter, A. Puretzky, and D. Geohegan. Observation of two distinct negative trions in tungsten disulfide monolayers. *Physical Review B*, 92(11), 2015.

[179] X. Duan, C. Wang, J. C. Shaw, R. Cheng, Y. Chen, H. Li, X. Wu, Y. Tang, Q. Zhang, A. Pan, J. Jiang, R. Yu, Y. Huang, and X. Duan. Lateral epitaxial growth of two-dimensional layered semiconductor heterojunctions. *Nat. Nanotechnol.*, 9:1024–1030, 2014.

[180] X. Q. Zhang, C. H. Lin, Y. W. Tseng, K. H. Huang, and Y. H. Lee. Synthesis of lateral heterostructures of semiconducting atomic layers. *Nano Lett.*, 15:410–415, 2015.

[181] Y. Gong, J. Lin, X. Wang, G. Shi, S. Lei, Z. Lin, X. Zou, G. Ye, R. Vajtai, B. I. Yakobson, H. Terrones, M. Terrones, B. K. Tay, J. Lou, S. T. Pantelides, Z. Liu, W. Zhou, and P. M. Ajayan. Vertical and in-plane heterostructures from WS_2/MoS_2 monolayers. *Nat. Mater.*, 13:1135–1142, 2014.

[182] K. Bogaert, S. Liu, J. Chesin, D. Titow, S. Gradecak, and S. Garaj. Diffusion-mediated synthesis of MoS_2/WS_2 lateral heterostructures. *Nano Lett.*, 16:5129–5134, 2016.

[183] K. Chen, X. Wan, W. G. Xie, J. X. Wen, Z. W. Kang, X. L. Zeng, H. J. Chen, J. B. Xu, and B. V. P. Ldas. Lateral built-in potential of monolayer MoS_2-WS_2 in-plane heterostructures by a shortcut growth strategy. *Adv. Mater.*, 27:6431, 2015.

[184] H. Heo, J. H. Sung, G. Jin, J. H. Ahn, K. Kim, M. J. Lee, S. Cha, H. Choi, and M. H. Jo. Rotation-misfit-free heteroepitaxial stacking and stitching growth of hexagonal transition-metal dichalcogenide monolayers by nucleation kinetics controls. *Adv. Mat.*, 27:3803–3810, 2015.

[185] C. Huang, S. Wu, A. M. Sanchez, J. J. Peters, R. Beanland, J. S. Ross, P. Rivera, W. Yao, D. H. Cobden, and X. Xu. Lateral heterojunctions within monolayer $MoSe_2$-WSe_2 semiconductors. *Nat. Mater.*, 13:1096–1101, 2014.

[186] M. Y. Li, Y. M. Shi, C. C. Cheng, L. S. Lu, Y. C. Lin, H. L. Tang, M. L. Tsai, C. W. Chu, K. H. Wei, J. H. He, W. H. Chang, K. Suenaga, and L. J. Li. Epitaxial growth of a monolayer WSe_2-MoS_2lateral p-n junction with an atomically sharp interface. *Science*, 349:524–528, 2015.

[187] M. Mahjouri-Samani, M. W. Lin, K. Wang, A. R. Lupini, J. Lee, L. Basile, A. Boulesbaa, C. M. Rouleau, A. A. Puretzky, I. N. Ivanov, K. Xiao, M. Yoon, and D. B. Geohegan. Patterned arrays of lateral heterojunctions within monolayer two-dimensional semiconductors. *Nat. Commun.*, 6:7749, 2015.

[188] H. N. Li, P. Li, J. K. Huang, M. Y. Li, C. W. Yang, Y. M. Shi, X. X. Zhang, and L. J. Li. Laterally stitched heterostructures of transition metal dichalcogenide: Chemical vapor deposition growth on lithographically patterned area. *ACS Nano*, 10:10516–10523, 2016.

[189] J. Y. Chen, W. Zhou, W. Tang, B. B. Tian, X. X. Zhao, H. Xu, Y. P. Liu, D. C. Geng, S. J. R. Tan, W. Fu, and K. P. Loh. Lateral epitaxy of atomically sharp WSe_2/WS_2 heterojunctions on silicon dioxide substrates. *Chem. Mater.*, 28:7194–7197, 2016.

[190] J. Kang, H. Sahin, and F. M. Peeters. Tuning carrier confinement in the MoS_2/WS_2 lateral heterostructure. *J. Phys. Chem. C*, 119:9580–9586, 2015.

[191] Y. Z. Guo and J. Robertson. Band engineering in transition metal dichalcogenides: Stacked versus lateral heterostructures. *Appl. Phys. Lett.*, 108:233104, 2016.

[192] J. Lee, J. S. Huang, B. G. Sumpter, and M. Yoon. Strain-engineered optoelectronic properties of 2D transition metal dichalcogenide lateral heterostructures. *2D Mater.*, 4:021016, 2017.

[193] K. Chen, X. Wan, J. X. Wen, W. G. Xie, Z. W. Kang, X. L. Zeng, H. J. Chen, and J. B. Xu. Electronic properties of MoS_2-WS_2 heterostructures synthesized with two-step lateral epitaxial strategy. *ACS Nano*, 9:9868–9876, 2015.

[194] F. Ceballos, M. G. Ju, S. D. Lane, X. C. Zeng, and H. Zhao. Highly efficient and anomalous charge transfer in van der Waals trilayer semiconductors. *Nano Lett.*, 17:1623–1628, 2017.

[195] M. M. de Lima, R. Hey, J. A. H. Stotz, and P. V. Santos. Acoustic manipulation of electron–hole pairs in gaas at room temperature. *Applied Physics Letters*, 84(14):2569–2571, 2004.

[196] C. Rocke, S. Zimmermann, A. Wixforth, J. P. Kotthaus, G. Böhm, and G. Weimann. Acoustically driven storage of light in a quantum well. *Physical Review Letters*, 78(21):4099–4102, 1997.

[197] P. Blake, E. W. Hill, A. H. C. Neto, K. S. Novoselov, D. Jiang, R. Yang, T. J. Booth, and A. K. Geim. Making graphene visible. *Appl. Phys. Lett.*, 91:063124, 2007.

[198] G. Rubio-Bollinger, R. Guerrero, D. de Lara, J. Quereda, L. Vaquero-Garzon, N. Agraït, R. Bratschitsch, and A. Castellanos-Gomez. Enhanced visibility of MoS_2, $MoSe_2$, WSe_2 and black-phosphorus: Making optical identification of 2d semiconductors easier. *Electronics*, 4(4):847, 2015.

[199] R.L. McCreery. *Raman Spectroscopy for Chemical Analysis*. Wiley, 2005. ISBN 9780471231875. URL `https://books.google.com/books?id=qY4MI0Zln1YC`.

[200] X. Zhang, X. Qiao, W. Shi, J. Wu, D. Jiang, and P. Tan. Phonon and raman scattering of two-dimensional transition metal dichalcogenides from monolayer, multilayer to bulk material. *Chemical Society Reviews*, 44(9):2757–2785, 2015.

[201] D. A. Chenet, O. B. Aslan, P. Y. Huang, C. Fan, A. M. van der Zande, T. F. Heinz, and J. C. Hone. In-plane anisotropy in mono- and few-layer ReS_2 probed by raman spectroscopy and scanning transmission electron microscopy. *Nano Lett.*, 15:5667–5672, 2015.

[202] R. He, J. A. Yan, Z. Y. Yin, Z. P. Ye, G. H. Ye, J. Cheng, J. Li, and C. H. Lui. Coupling and stacking order of ReS_2 atomic layers revealed by ultralow-frequency raman spectroscopy. *Nano Lett.*, 16:1404–1409, 2016.

[203] E. Lorchat, G. Froehlicher, and S. Berciaud. Splitting of interlayer shear modes and photon energy dependent anisotropic raman response in n-layer $ReSe_2$1 and ReS_2. *ACS Nano*, 10: 2752–2760, 2016.